FABRICATION AND CHARACTERIZATION OF MICROLASERS BY THE SOL-GEL METHOD

Thesis by

Lan Yang

In Partial Fulfillment of the Requirements for the

Degree of

Doctor of Philosophy

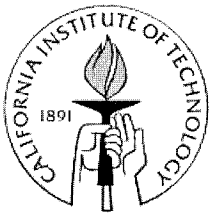

CALIFORNIA INSTITUTE OF TECHNOLOGY

Pasadena, California

2005

(Defended May 16, 2005)

ACKNOWLEDGEMENTS

The time I have spent at Caltech was certainly fruitful and enjoyable. Caltech not only opened the door to scientific research, but also broadened my view in many aspects to the world. I feel very grateful to spend part of my life in this wonderful place.

There are many people to thank for their support and encouragement, without whom this thesis would have not been possible. First I would like to thank my thesis advisor, Professor Kerry J. Vahala, for his patience, support, and guidance through my five years in his group at Caltech. It has been a great pleasure to be one of his students. His deep understanding of physics and his fascination with both fundamental and applied science are what have inspired me most. While allowing and encouraging me to work independently, he was always ready to offer helpful suggestions and insightful comments. In spite of his many responsibilities, he was never too busy to give inspiration, detailed comments, including correcting my naïve grammar mistakes on my papers, or simply to chat. I truly believe I could not have had a better advisor, and his attitude toward science, education and even life will serve as a role model for me in the years to come.

I want to thank other members of my thesis Advisory Committee: Professor Demetri Psaltis, Professor Oskar Painter, Professor David Rutledge and Professor Changhuei Yang, for their useful comments and suggestions for the work included in this thesis.

I have enjoyed working with people in the lab and would like to thank, Dr. Min Cai, Dr. Mark Brongersma, Dr. Sean M. Spillane, Dr. Tobias, J. Kippenberg, Hosein Rohksari, Deniz Armani, and Andrea Martin. Special thanks go to Dr. Tal Carmon and Bumki Min,

with whom I have had a fruitful collaboration. I would like to thank Bumki Min for his willingness to share his knowledge with me and I have enjoyed talking with him very much. It is also an enjoyable experience working with Dr. Tal Carmon and I like his "Hebrew wisdom" very much. I also would like to thank Alireza Ghaffari for showing me how to use some facilities, such as mask aligner and spinner, in the clean room.

I also want to thank my friends for making the graduate school life a colorful experience. Many thanks go to Lili Yang, Pin Wang, Weiwei Zhong, Yin Gong, Chunhui Mo, Qiang Yang, Zhengrong Wang, Jiao Lin, Jian Wu, Qingsong Zhang, Wei Liang, Yanyi Huang, Jie Yu, Ying Li, Charles Fan, Fang Wang, and Chunhua Qi……

I thank my beloved family whose love and encouragement are extremely important to me. I appreciate what they have done for me throughout these years. I also thank my husband Hongyu for his unlimited support, who made the possibly-dreary graduate school life a pleasant experience overall. With beloved ones around, I can move forward full of passion and hope.

ABSTRACT

The present study explores the application of new materials systems for low threshold microlasers, and characterization of the microcavities. The sol-gel method is used for gain functionalization of high-Q microcavities. A detailed procedure for preparation of the sol-gel films by the spin-on or dip-coating method is presented. The effect of different process conditions on the properties and microstructure of the thin films is investigated through Fourier Transform Infrared (FTIR) Spectroscopy, Scanning Electron Microscopy (SEM), and etching rate test.

Surface gain functionalization of microsphere cavities is fabricated by coating the microsphere with a thin layer of Er^{3+}-doped sol-gel films. The optical gain is due to the population inversion of rare earth ions in the sol-gel films. A fiber taper is used to both couple the pump power into and extract the laser power out of the microsphere laser. The laser dynamics change between continuous-wave and pulsating operation by varying the doping concentration and the thickness of the sol-gel films outside the microsphere.

Surface functionalization is also achieved on the microtoroid on a single silicon chip, which can be fabricated in parallel using wafer-scale processing and has characteristics that are more easily controlled than microsphere. The microtoroid can be selectively coated only at the periphery by making use of the variation of etching rate (in buffered HF) of sol-gel films with different degrees of densification. The laser performance of the gain functionalized microtoroids is investigated. Highly confined whispering gallery modes make possible single-mode microlasers. This work also shows that the high Q microtoroid laser has a linewidth much lower than 300 kHz.

The thesis explores fabrication of high Q microcavities directly from the sol-gel silica films deposited on a single silicon wafer. Quality factor as high as 2.5×10^7 at 1561 nm is obtained in toroidal microcavities formed of silica sol-gel, which allows Raman lasing at absorbed pump power below 1 mW. Additionally, Er^{3+}-doped microlasers are fabricated from Er^{3+}-doped sol-gel layers with control of the laser dynamics possible by varying the erbium concentration of the starting sol-gel material. Continuous lasing with a record threshold of 660 nW for erbium-doped microlaser on a silicon wafer is also obtained.

Analytic formulas are derived to predict the laser performance, such as the laser output power, the threshold power, and the differential quantum efficiency, under different loading condition, i.e. the air gap between the fiber-taper coupler and the cavities. The effect of Er^{3+} concentration on the minimum threshold is also investigated. In addition, we present a theoretical model in which we include paired ions as the saturable absorber. It shows that self-pulsing operation can be expected with paired-ions-induced quenching in the system. The pulsation frequency increases linearly with the square root of the pumping level, which is consistent with the experimental observation.

TABLE OF CONTENTS

LIST OF FIGURES

LIST OF TABLES

Chapter 1

INTRODUCTION

There has been interest in microresonators, which are attractive systems both for fundamental physics research in the fields of nonlinear optics, cavity quantum electrodynamics and for applications in sensor for bio-molecule and low threshold microlasers etc. [1-4]. My research interest lies in exploring application of new materials system for low threshold microlasers and evaluating the performance of the devices. Optical gain can be obtained not only through nonlinear optical process such as Stimulated Raman Scattering (SRS), but also through population inversion of rare earth ions in a host medium [5]. High finesse microcavities are good candidate for low threshold microlasers. Chang's research group reported lasing from rhodamine doped ethanol [6]. Later Campillo and his colleagues observed Stimulated Raman Scattering from CS_2 microdroplets [7-9]. However the liquid droplets are difficult to handle and suffer from their short lifetime due to the evaporation in the air. More recently, Ilchenko first showed a surface-tension-induced silica microsphere exhibiting relatively small mode volume with the highest observed quality factor (Q) up to 10^{10} at 633 nm corresponding to photon storage times in the order of microsecond [10]. Subsequently, an ultra-low-threshold microsphere Raman laser was demonstrated due to high power build-up factor of these ultra-high-Q microcavities [11]. Nd^{3+}-doped silica microsphere and Er^{3+}-doped phosphate sphere microlasers have been reported by Sandoghdar and Cai [3, 12], who made the sphere by

heat-fusing the tip of a doped silica or phosphate wire. All the microspheres are made by heat-fusing the tip of a glass wire. For the pure silica microsphere, a regular silica optical fiber can be used, while for the doped microsphere, either the Nd^{3+}-doped silica wire was obtained by HF etching the cladding of a fiber with a core of 20 μm in diameter doped with 0.2 wt% Nd^{3+}, or the Er^{3+}/Yb^{3+} codoped phosphate wire was pulled from a piece of melted Er^{3+}/Yb^{3+} bulk phosphate glass. However, it tends to form some crystallized spots during the melting-and-pulling process to get the doped-phosphate wire and further heating can not get rid of the crystallization defect, which makes the final microsphere inhomogeneous and degrade the quality factor of the microcavites.

On the other hand, sol-gel method has been used for preparation of oxide in a variety forms [13]. This thesis centers on the fabrication of microlasers by surface gain functionalization of existing high-Q microcavities with sol-gel films or directly processing of sol-gel films into a microlasers. Throughout the thesis work, a CO_2 laser was used to modify the sol-gel materials. The laser reflow process endows the sol-gel material very high optical quality. This thesis also includes a detailed study of the microlasers. Before turning to the outline of the thesis, a brief introduction of the sol-gel method in optics field will be outlined.

1.1 Motivation

The sol-gel process actually offers unique opportunity for the synthesis of optical materials with composition stoichiometrically controlled. The homogeneous mixture of several

components in liquid state makes it possible to vary the optical materials over a wide range of compositions at molecular level, therefore the optical properties of the materials are tailored, such as Ge dopants to change the refractive index [14], P dopants to increase nonlinear gain coefficient of silica and rare earth dopants to create gain in the host materials [15-17]. In summary, the sol-gel method provides an efficient and cost-effective platform for us to explore the effects of different dopants on the properties of the microcavities.

1.2 Organization of the Thesis

To provide a common footing for the chapters that follow, chapter 2 introduces the origin of the Whispering Gallery Mode (WGM) cavities. Several terminologies, such as finesse and optical quality factor, used in cavities are also introduced. The mode characterization and field distribution of the microsphere is discussed. Tracing of the modes in microsphere is visible by using up-conversion (540 nm transition) of Er^{3+} inside the sol-gel films coated outside the microsphere.

Chapter 3 describes the fabrication process of fiber taper and gives a review of the fiber taper coupling schemes used throughout this work. A simple theoretical model is presented to study the coupling mechanism between the fiber taper and the microcavities. The coupling efficiency adjusted by variation of the air gap between the microcavities and the taper is discussed in details.

Chapter 4 introduces the sol-gel method and its application in optics field. A detailed procedure for preparation of sol-gel films by spin-on or dip-coating method is presented. The effect of different annealing temperature on the properties of the thin films is investigated by Fourier Transform Infrared (FTIR) Spectroscopy. An etching rate test of the sol-gel films further reveals the change of microstructure of the sol-gel films annealed under different temperature.

Chapter 5 investigates surface gain functionalization of microsphere cavities by coating the microsphere with a thin layer of Er^{3+}-doped sol-gel films. The procedure for fabrication of silica microsphere is presented followed by surface functionalization of the microsphere. A fiber taper is used to both couple the pump power into and extract the laser power out of the microsphere laser. A single frequency laser is obtained under certain pump wavelength and coupling condition. It demonstrates that the laser dynamics can be changed by variation the thickness of the doping films outside the microsphere.

Chapter 6 describes the surface functionalization of a microcavities on a single silicon chip, the microtoroid. Although the ultra-high-Q microsphere is far more robust and stable than the liquid microdroplets, it's not wafer based device and is not suitable for integration with other optical or electronic functions. In addition it's difficult to prepare the microspheres in large scale. In contrast, microlasers on a chip can be fabricated in parallel using wafer-scale processing and have characteristic that are more easily controlled. A numerical simulation of the microtoroid modes shows that the modes are compressed in polar direction compared with the micropshere. The surface functionalization process for

the microtoroid is very similar to that used for the microsphere, except that the microtoroid can be selectively coated only at the periphery by making using of the variation of etching rate (in buffered HF) of sol-gel films with different degree of densification. The laser performance of the gain functionalizaed microtoroids is investigated. With the reduction of freedom in the azimuthal direction, a simpler mode spectra than that of the microsphere is obtained, which makes it easier to get single laser line. A high finesse Fabry-Perot etalon was used to compare the linewidth of the microlaser with that of a single frequency external cavity laser with know linewidth of 300 kHz, which shows that the high-Q microtoroid laser has a much narrower linewidth than 300 kHz.

Chapter 7 explores fabrication of microtoroid lasers directly from the sol-gel films deposited on a single silicon wafer. It's demonstrated that a Raman microlaser can be made from pure silica sol-gel film, while an Er^{3+}-doped microlaser can be achieved from Er^{3+}-doped silica sol-gel films. The single mode Raman lasing and single mode Er^{3+} lasing are presented. A fiber taper was used to couple the pump light into and laser light out of the microtoroids. Analytical formulas were developed to study the change of pump threshold, differential quantum efficiency and laser output power with the air gap between the fiber taper coupler and the microcavities. The effect of Er^{3+} concentration on the minimum absorbed threshold power is also investigated.

In chapter 8, a theoretical modal is developed to study the effect of Er^{3+} concentration due to ion-pair induced quenching on the laser dynamics. Thereafter, experimental data is presented to compare with the simulation results.

Chapter 9, the final chapter, draws upon the general conclusions of the previous chapters to speculate on further study following this work.

Chapter 2

WHISPERING GALLERY TYPE MICRORESONATORS

2.1 Introduction

A wide range of resonator constructed for different applications have been fabricated and investigated. Among them the surface-tension-induced microcavities, such as microsphere and microdisk, attract great interests because unprecedented quality factor (Q) as high as a several billion have been achieved in silica microphere, which are of great use for ultra-narrow linewidth, cavity QED, ultra-low threshold microlasers, and other photonics application. The microsphere, together with cavities with circular geometry, is called Whispering Gallery Mode (WGM) resonators. The WGM is named after the sound effect noted in some cathedrals, where one can whisper along the wall and hear all along the inside perimeter of the dome. Light presents the same behavior when injected tangentially into the WGM type cavities, where light is trapped in circular orbits just within the surface by repeated total internal reflections. This low dissipation mechanism for confinement leads to unusual high quality factor mentioned above.

In this chapter, the mode characterization and field distribution in the microsphere, a typical Whispering Gallery type resonator, is studied. The most important figure of merit, Cavity quality factor Q, is introduced. A typical mode spectrum from a microsphere cavity is presented. In the end, an Er^{3+}-doped microsphere is used to demonstration different WGMs.

2.2 Microsphere resonators

To investigate the electromagnetic modes in the microsphere cavity, we study the Maxwell's equation in an isotropic medium with constant scalar permittivity and permeability, and free of charge and current.

$$\nabla \cdot D = 0 \tag{2.1}$$

$$\nabla \cdot B = 0 \tag{2.2}$$

$$\nabla \times E = -\frac{\partial B}{\partial t} = -\mu \frac{\partial H}{\partial t} \tag{2.3}$$

$$\nabla \times H = -\frac{\partial D}{\partial t} = \varepsilon \frac{\partial E}{\partial t} \tag{2.4}$$

First we take the curl of the Maxwell's curl equation for electric field (2.3), and use the vector identity

$$\nabla \times \nabla \times A = \nabla(\nabla \cdot A) - \nabla^2 A \tag{2.5}$$

to obtain

$$\nabla(\nabla \cdot E) - \nabla^2 E = -\mu \nabla \times (\frac{\partial H}{\partial t}). \tag{2.6}$$

Then using (2.1) and substituting (2.4) in (2.5), we find

$$\nabla^2 E - \mu\varepsilon \frac{\partial^2 E}{\partial t^2} = 0 \tag{2.7}$$

If we assume the field quantities to vary as $E(\vec{r},t) = E(\vec{r})e^{i\omega t}$, we obtain:

$$\nabla^2 E + k^2 E = 0 \tag{2.8}$$

where $k = \omega\sqrt{\mu\varepsilon}$

It's been verified numerically that the polarization direction of the electromagnetic field of a sphere can be approximated constant along the same spherical coordinate axes at all points in space. Therefore the either E_θ or H_θ component of the electromagnetic field is separable, i.e. $E_\theta = \psi_r(r)\cdot\psi_\theta(\theta)\cdot\psi_\phi(\phi)$, or $H_\theta = \psi_r(r)\cdot\psi_\theta(\theta)\cdot\psi_\phi(\phi)$. Here we consider the transverse electric (TE) mode, where the electric field is parallel to the surface with $\vec{E} = E_\theta\vec{\theta}$ and $E_\phi = E_r = 0$. Similar process can be used to study the transverse magnetic (TM) mode. Consider the wave equation (2.8) in spherical coordinate system:

$$\frac{1}{r^2}\frac{\partial}{\partial r}\left(r^2\frac{\partial E}{\partial r}\right) + \frac{1}{r^2\sin\theta}\frac{\partial}{\partial\theta}\left(\sin\theta\frac{\partial E}{\partial\theta}\right) + \frac{1}{r^2\sin^2\theta}\frac{\partial^2 E}{\partial\phi} + k^2 E = 0 \tag{2.9}$$

Equation (2.9) can be solved by separation of variables.

$$\frac{1}{\psi_r}\frac{d}{dr}(r^2\frac{d\psi_r}{\partial r})+\frac{1}{\psi_\theta \sin\theta}\frac{d}{d\theta}(\sin\theta\frac{d\psi_\theta}{d\theta})+\frac{1}{\psi_\phi \sin^2\theta}\frac{d^2\psi_\phi}{d\phi}+k^2r^2=0$$

Thus there are three ordinary differential equation, one in r only, one in θ only and one in ϕ.

(a). The radial dependence satisfy the equation

$$\frac{d^2\psi_r}{dr^2}+\frac{2}{r}\frac{d\psi_r}{dr}+(k^2-\frac{l(l+1)}{r^2})\psi_r=0 \qquad (2.10)$$

This is the spherical Bessel differential equation, and the solutions are called spherical Bessel functions of order l. Within the sphere the general solutions of (2.10) is

$$\psi_r=c_1 j_l(kr)+c_2 n_l(kr) \qquad (2.11)$$

For the field inside the sphere, $r<R_0$, we must consider the behavior of the field as $r\to 0$. While for $x<<1$, $j_l(x)\to\frac{x^l}{(2l+1)!!}$ and $n_l(x)\to-\frac{(2l-1)!!}{x^{l+1}}$, which means that $n_l(x)$ is divergent as $r\to 0$. Since the field should be finite at $r=0$, so the fields inside the sphere ($r<R_0$, where R_0 is the radius of the sphere) is

$$\psi_r=c_1 j_l(kr) \quad \text{for} \quad r<R_0 \qquad (2.12)$$

Outside the sphere, it's an evanescent field which will decay exponentially in the radial direction. To get the solution outside the sphere, we use substitution of variables by assuming $\psi_r = \frac{\varphi_r}{r}$ and obtain:

$$\frac{d^2\varphi_r}{dr^2} + (k^2 - \frac{l(l+1)}{r^2})\varphi_r = 0 \tag{2.13}$$

Let $r = R_0 + \Delta r$ and equation (2.13) become:

$$\frac{d^2\varphi_r}{d\Delta r^2} + (k^2 - \frac{l(l+1)}{(R_0 + \Delta r)^2})\varphi_r = 0 \tag{2.14}$$

Because the amplitude of the fields decay rapidly outside the sphere, we are interested in the region of space that is within several wavelength out from the sphere surface. We can assume that $\frac{\Delta r}{R_0}$, so equation (2.14) is simplified to:

$$\frac{d^2\varphi_r}{d\Delta r^2} + (k^2 - \frac{l(l+1)}{R_0{}^2})\varphi_r = 0 \tag{2.15}$$

Equation (2.15) describes an evanescent field in the radial direction outside the sphere. The solution is an exponentially decay field:

$$\varphi_r \sim exp(-\alpha \cdot \Delta r), \text{ with } \alpha = \sqrt{\frac{l(l+1)}{R_0{}^2} - k^2} \tag{2.16}$$

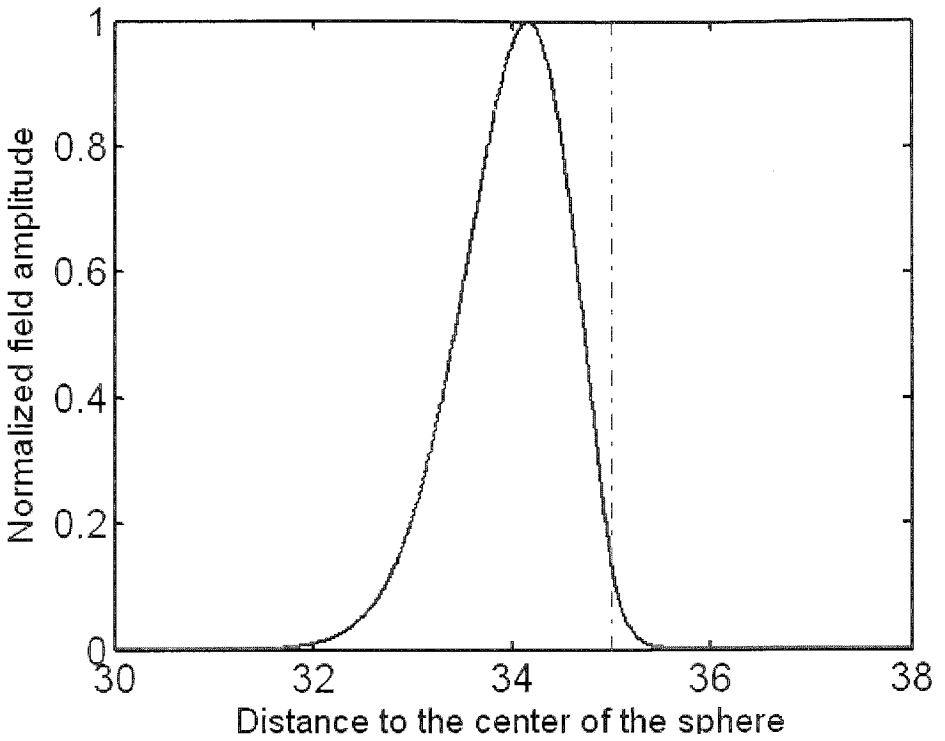

Figure 2.1. The field profile of a TE mode in the radial direction for a microsphere with diameter of 70 μm. The wavelength is at 1.5572 μm and the mode numbers are $n = 1, and\ l = 192.$

So the full radial dependence is:

$$\psi_r = \begin{cases} A\ j_l(kr) & for\ r < R_0 \\ B\ exp(-\alpha \cdot (r - R_0)) & for\ r > R_0 \end{cases} \tag{2.17}$$

with $\alpha = \sqrt{l(l+1)/R_0^2 - k^2}$, and A, B are constants, which will be determined by boundary condition at surface and the normalization condition. The radial dependence of

the fields are related to mode numbers l and n. Furthermore the number of field maximum along the radial direction is determined by n.

(b). The azimuthal dependence satisfy the equation

$$\frac{d^2\psi_\phi}{d\phi} + m^2\psi_\phi = 0 \tag{2.18}$$

The field in the azimuthal direction has a periodicity of 2π, so the azimuthal dependence of the field is:

$$\psi_\phi = N_\phi \, exp(im\phi) \tag{2.19}$$

where m is an integer and N_ϕ is the normalization constant to be chosen so that after one revolution the integral of $|\psi_\phi|^2$ is unity

(c). The polar dependence is

$$\frac{1}{sin\theta}\frac{d}{d\theta}(sin\theta\frac{d\psi_\theta}{d\theta}) + \left[l(l+1-\frac{m^2}{sin^2\theta})\right]\psi_\theta = 0 \tag{2.20}$$

This is polar-dependent part of a spherical harmonic differential equation and the solution is associated Legendre polynomials. So the polar solution of the field is:

$$\psi_\theta = N_\theta P_l^m(cos\theta) \tag{2.21}$$

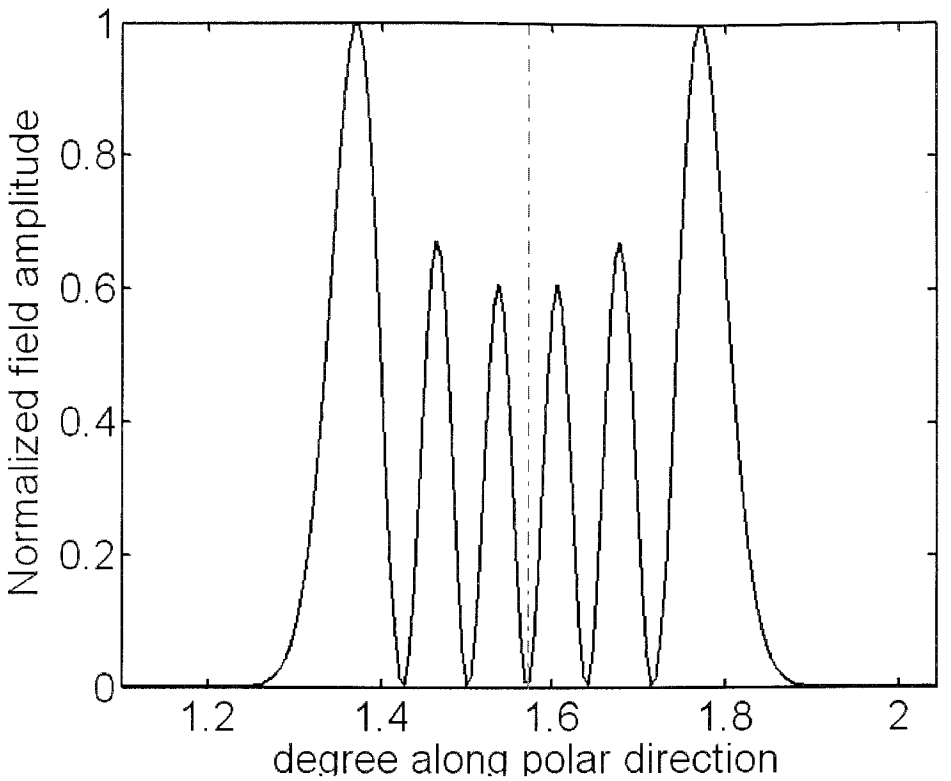

Figure 2.2. The field profile of a TE mode in the azimuthal direction for a microsphere with diameter of 70 μm. The wavelength is 1.557μm and mode numbers are $n = 1, l = 192, m = l - 4$.

where $m = -l, -(l-1), \ldots, l-1, l$ and $P_l^m(\cos\theta)$ is an associated Legendre polynomial. N_θ is the normalization constant to be chosen so that the integral of $|\psi_\theta|^2$ over θ is unity. Figure 2.3 shows images of different WGM of an Er^{3+}-doped microsphere, where the up-conversion transition in 540 nm is used to trace the mode.

The characteristic equation:

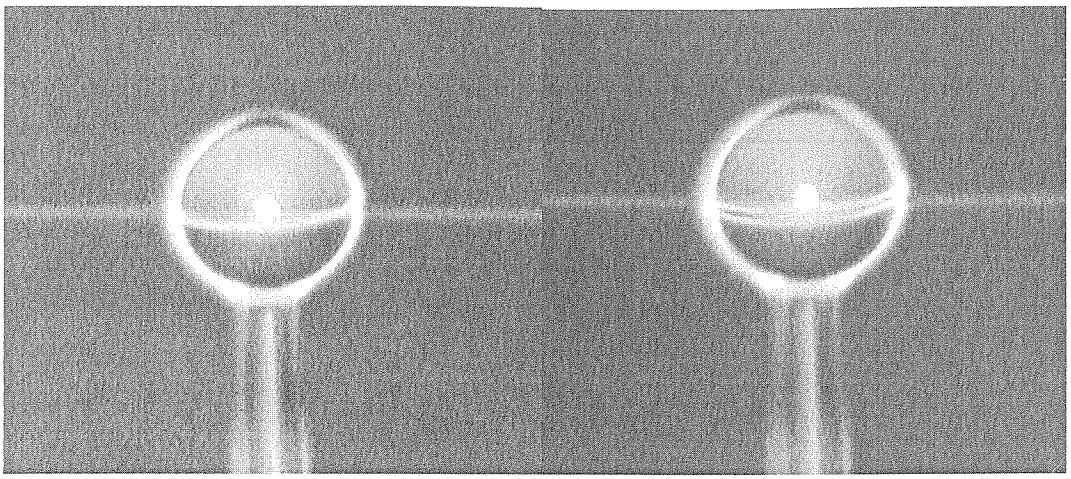

(a) (b)

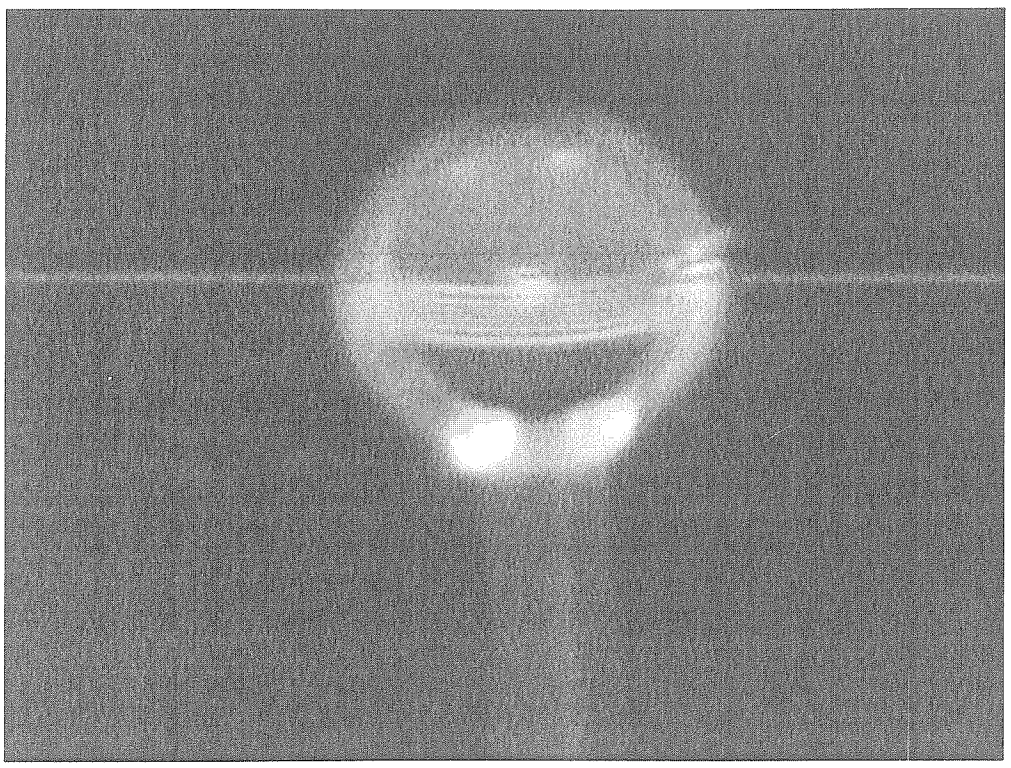

(c)

Figure 2.3. Image of the WGMs in the taper-sphere coupling zone: (a) l-m=0. (b) l-m=1. and (c)l-m=5. The green rings are up-converted photoluminescence.

For the TE mode, the magnetic field can be solved from Maxwell's equation:

$$\vec{H} = -i\frac{1}{\omega\mu}\nabla \times E_\theta \vec{\theta}$$

$$= -i\frac{1}{\omega\mu}\left(-i\frac{m}{r\sin\theta}E_\theta \vec{r} + \left(\frac{E_\theta}{r} + \frac{\partial E_\theta}{\partial r}\right)\vec{\phi}\right) \tag{2.22}$$

The electromagnetic fields must satisfy the boundary condition that the tangential components E_θ and H_ϕ should be continuous at $r = R_0$. This leads to

$$\frac{\frac{j_l(k_0 n_s R_0)}{R_0} + k_0 n_s j_l'(k_0 n_s R_0)}{j_l(k_0 n_s R_0)} = \frac{1}{R_0} - \alpha_s \tag{2.23}$$

Similarly for TM mode

$$\frac{\frac{j_l(k_0 n_s R_0)}{R_0} + k_0 n_s j_l'(k_0 n_s R_0)}{j_l(k_0 n_s R_0)} = \left(\frac{1}{R_0} - \alpha_s\right)\frac{n_s^2}{n_0^2} \tag{2.24}$$

We now use the spherical Bessel function recursion relation

$$j_l'(x) = \frac{l \cdot j_l(x)}{x} - j_{l+1}(x) \tag{2.25}$$

and (2.22) and (2.23) become

$$\text{TE modes: } \left(\frac{l}{R_0}+\alpha_s\right) j_l(k_0 n_s R_0) = k_0 n_s j_{l+1}(k_0 n_s R_0) \tag{2.26}$$

$$\text{TM modes: } \left(\left(l+1-\frac{n_s^2}{n_0^2}\right)\frac{1}{R_0}+\frac{n_s^2}{n_0^2}\alpha_s\right) j_l(k_0 n_s R_0) = k_0 n_s j_{l+1}(k_0 n_s R_0) \tag{2.27}$$

These characteristic equation relates the wavevector k_0 and mode number l and n. For a cavity with $R_0 >> \lambda$, the mode number $l >> 1$, (e.g. for $n_s = 1.43$, $R_0 = 50\ \mu m$, $\lambda = 1.55\ \mu m$, the mode number $l \sim 2n_s \pi R_0 / \lambda = 290$), the characteristic equation for TM mode can be simplified to

$$\text{TM modes: } \left(\frac{l}{R_0}+\frac{n_s^2}{n_0^2}\alpha_s\right) j_l(k_0 n_s R_0) = k_0 n_s j_{l+1}(k_0 n_s R_0) \tag{2.28}$$

2.3 Cavity quality factor (Q)

The quality factor Q is often used to characterize the resonators. It is defined in terms of energy storage and power loss:

$$Q_{tot} = \frac{2\pi(\text{stored energy})}{\text{energy loss per cycle}} = \frac{\omega_0 U}{W} \tag{2.29}$$

where ω_0 is the cavity resonant frequency, U is the energy stored in the mode, and W is the energy loss rate of the mode. So a differential equation can be used to describe the

behavior of stored energy U inside the cavity

$$\frac{dU}{dt} = -\frac{\omega_0}{Q}U \tag{2.30}$$

where ω_0 is the resonant frequency of the cavity. The solution to the equation above is

$$U(t) = U_0 e^{-\frac{\omega_0}{Q}t} \tag{2.31}$$

So the optical field in the cavity is damped as follows:

$$E(t) = E_0 e^{i\omega_0 t} e^{-\omega_0 t/2Q} \tag{2.32}$$

The Standard Fourier analysis yields the optical field in the frequency domain

$$|E(\omega)|^2 = \left| \int_{-\infty}^{\infty} E(t) e^{-i\omega t} dt \right|^2$$

$$= \left| \int_{-\infty}^{\infty} E_0 e^{i(\omega_0 - \omega)t} e^{-\omega_0 t/2Q} dt \right|^2$$

$$= \frac{E_0^2}{(\omega - \omega_0)^2 + (\omega_0/2Q)^2} \tag{2.33}$$

The resonance has a Lorentzian shape with a Full Width at Half Maximum (FWHM) equal to ω_0/Q. Therefore the quality factor Q is related to the linewidth of the mode by $Q = \omega_0/\Delta\omega$. A high resolution Whispering Gallery mode spectrum of a microsphere is

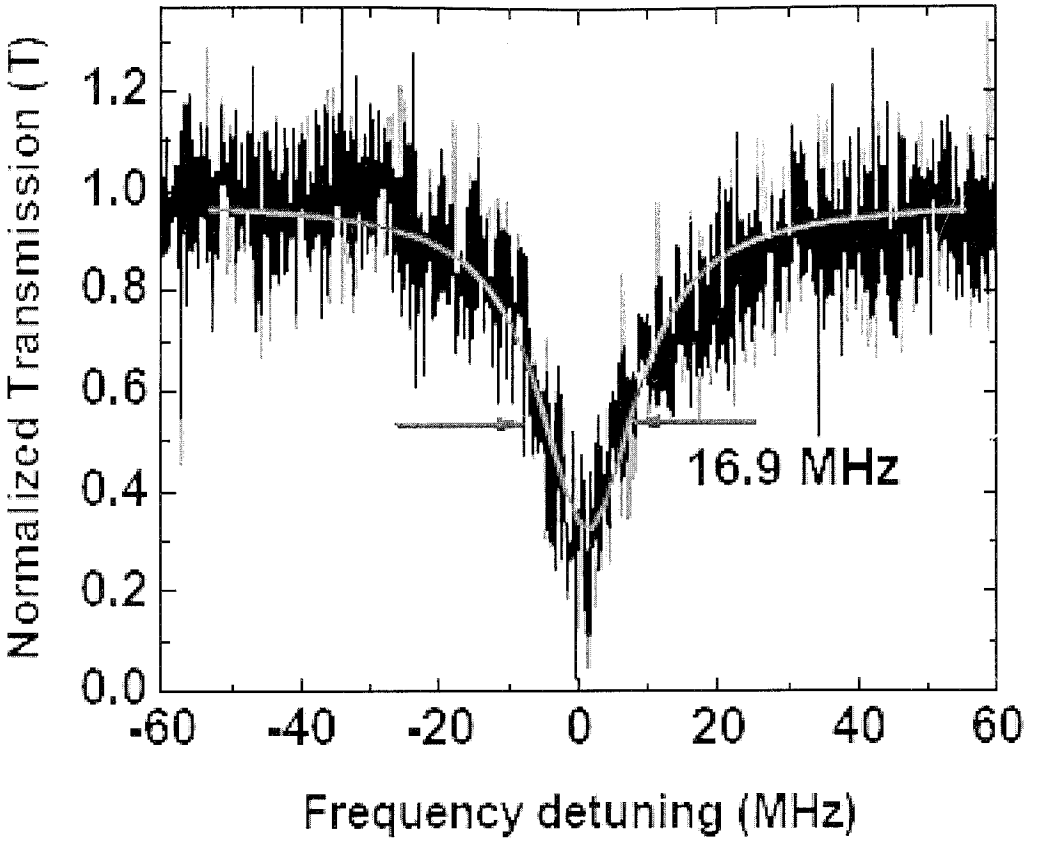

Figure 2.4. High resolution whispering gallery mode spectrum. The quality factor is 2×10^7 at 980 nm.

presented in figure 2.4, where the total quality factor is deduced from the linewidth of the mode.

We recall the definition of the cavity quality factor given by (2.30), and the total quality factor is decided by the total loss rate in the cavities. There are several loss mechanisms in optical resonators, thus we can rewrite equation (2.30) as

$$\frac{1}{Q_{tot}} = \frac{W_{tot}}{\omega U} = \frac{W_{mat}}{\omega U} + \frac{W_{ss}}{\omega U} + \frac{W_{sc}}{\omega U} + \frac{W_{rad}}{\omega U} + \frac{W_{coup}}{\omega U}$$

$$= \underbrace{\frac{1}{Q_{mat}} + \frac{1}{Q_{ss}} + \frac{1}{Q_{sc}} + \frac{1}{Q_{rad}}}_{Intrinsic\ Quality\ factor} + \underbrace{\frac{1}{Q_{coup}}}_{External\ Quality\ factor} \qquad (2.34)$$

where Q_{mat} accounts for materials absorption loss, Q_{ss} denotes the scattering loss from surface inhomogeneities, Q_{sc} describe the loss caused by surface contamination, Q_{rad} represents the tunneling loss due to the curvature of the boundaries in the propagation path of the mode, and Q_{coup} describes the coupling loss to a coupler. The quality factor describing the loss from materials absorption, scattering, surface contamination and radiation are usually called "cold cavity quality factor" or "intrinsic quality factor", while Q_{coup}, which accounts for the coupling to a external coupler, is designated as 'external quality factor'. As studied by Haus and his colleague, Q_{rad} increase exponentially with increasing size, and for air clad microspheres with radii larger than about 15 μm, $Q_{rad} > 10^{11}$ [18]. While the absorption of silica at the wavelength of 1.55 μm can be as low as 0.2 dB/km, which corresponds to an absorption limited quality factor of 10^{11}. Therefore absorption and surface scattering are the predominant loss mechanism for silica microspheres with radii larger than 15 μm.

Materials Loss:

The quality factor due to materials absorption can be determined by [10]:

$$Q_{mat} = \frac{2\pi n}{\lambda \alpha} \tag{2.35}$$

where λ is the wavelength, n is the refractive index of the materials at λ, and α is the linear attenuation in the resonator caused by materials absorption.

Scattering Loss:

The quality factor due to scattering loss by the surface homogeneity can be estimated by [10]

$$Q_{ss} = \frac{\lambda^2 R_0}{\pi^2 \sigma^2 B} \tag{2.36}$$

where σ and B are the rms size the correlation length of surface homogeneities, respectively.

Radiation Loss:

The Quality factor associated with the radiation loss is shown to be [18]:

$$Q_{rad} = \frac{l^2 n_s}{k^3 c \varepsilon_0 N_s n_0^2 R_0^5 Z_0} \left[\begin{array}{l} n_0 \left(\frac{\pi}{\gamma_l} \right) j_l(kn_s R_0) j_{l+1}(kn_s R_0) \\ - n_s \left(\frac{\pi}{\gamma_2} \right) j_{l-1}(kn_s R_0) j_l(kn_s R_0) \end{array} \right]^{-2} \tag{2.37}$$

with $\gamma_l = l - \frac{1}{2} - kn_0R_0 \frac{j_l(kn_0R_0)}{j_{l-1}(kn_0R_0)} + \frac{(kn_0R_0)^2}{l}$

$$\gamma_2 = l + \frac{1}{2} - kn_0R_0 \frac{j_{l+1}(kn_0R_0)}{j_l(kn_0R_0)} + \frac{(kn_0R_0)^2}{l}$$

where c is the speed of light in the vacuum, ε_0 is the permittivity of free space, $Z_0 \approx 377$ is the free space impedance.

Chapter 3

OPTICAL COUPLING BETWEEN FIBER TAPER AND WGM CAVITY

3.1 Introduction

In this chapter we will review various methods developed to excite microsphere modes. The fiber taper is used as an efficient way to couple the light into and out of the microcavities throughout this thesis work. The coupling between the fiber taper and microsphere cavities is investigated in details.

3.2 General methods for coupling to microsphere and microcavities

The modes in the WGM type microcavities are highly confined and are not accessible by free-space beam. Therefore employments of near-field couplers are highly required. Numerous methods have been developed to excite the whispering gallery modes in microsphere resonators. The evanescent coupling scheme in which an evanescent field tunnels into the microsphere appears to be the most promising approaching without disturbing the high Q property of the cavities. As depicted in figure 3.1, the prism can be used to efficiently couple the light into and out of the microsphere [19], but it uses bulk component and it is difficult to align it with microsphere. The polished half block coupler provides is a robust way to couple the light into the microsphere but the coupling efficiency

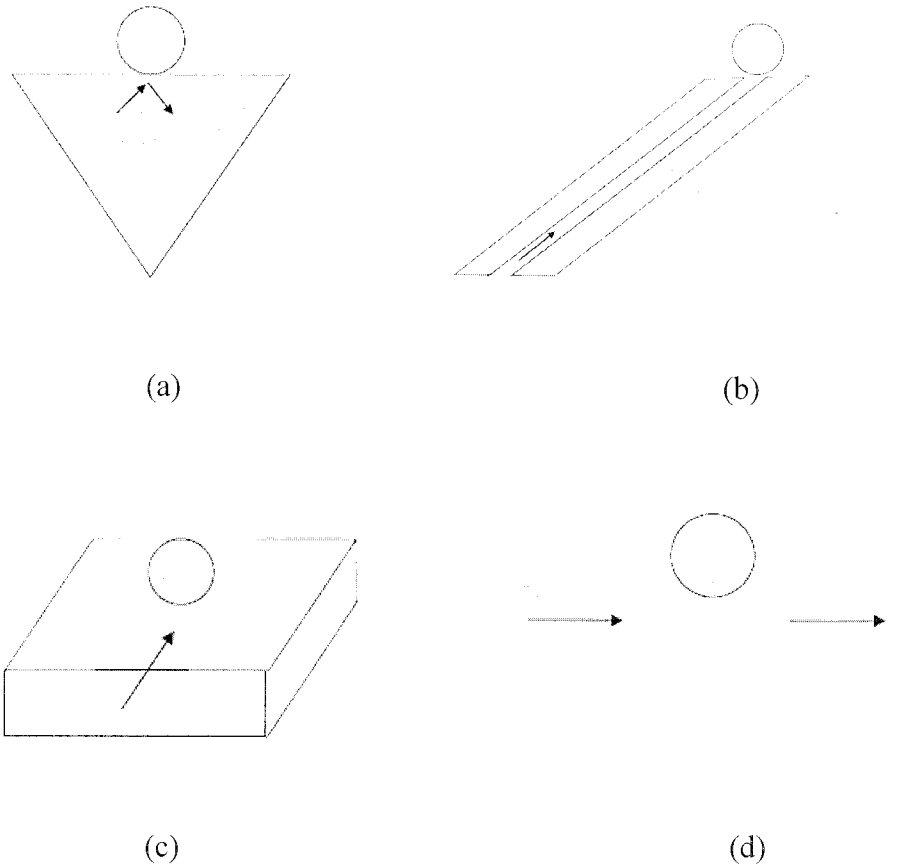

Figure 3.1. Different coupling schemes for microspheres: (a) Prism coupler; (b) Angle polished fiber tip; (c) Polished half block coupler; (d) fiber taper

is low because of the light coupled to the cladding radiation mode of the half block [20, 21]. The angle polished fiber is efficient to excite the microsphere modes, but it requires delicate cutting of the angle and polishing the end of the fiber tip [22]. The fiber taper coupler can not only to align with the microsphere but only efficiently couple the light into and out of the microsphere cavities. In the following part, we will focus on the fiber taper coupler.

3.3 Fabrication of the fiber taper

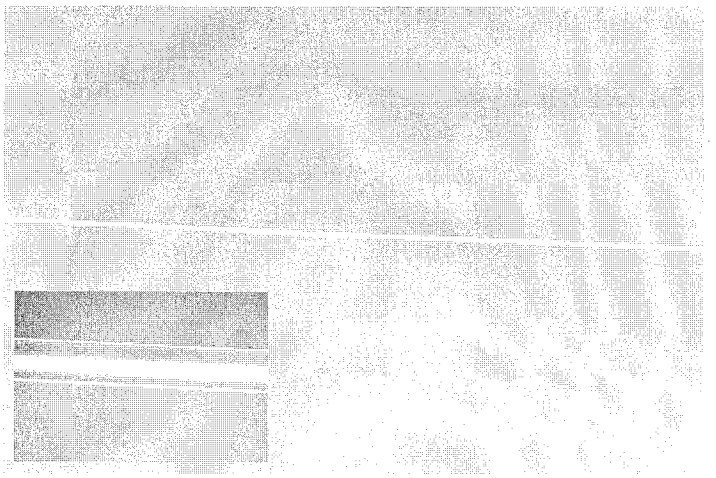

Figure 3.2. Optical image of waist of the fiber taper. Inset: a standard 125 μm single mode optical fibers

The fiber taper is fabricated from a standard optical fiber. The fiber is first mounted on a stage which can hold the fiber throughout all the experiment. Then the fiber is exposed to the top zone of a hydrogen flame, where the temperature is high enough to melt the silica. Right after the fiber become soft due to the heat absorption, two computer program controlled motors begin to pull each end of the fiber to opposite direction. The pulling process is stopped when the waist size of the fiber taper decreases to 1 to 2 μm. Figure 3.2 shows an optical image of a tapered fiber with waist diameter around 1 μm. The inset presents an image of a standard SMF-28 optical fiber with diameter of 125 μm for comparison.

3.4 Characterization of the fiber taper modes

Although the fiber taper is pulled from a fiber with core and cladding region, during the pulling process the core vanishes and the fiber taper can be regarded as an air-clad cylinder waveguides. The analytic solution for mode of propagation in cylinder waveguide is well known. The characteristic equation which determines the propagation constant (β_f) of the fiber mode is [18]:

$$k_f \frac{J_1(ak_f)}{J_0(ak_f)} = \alpha_f \frac{K_1(ak_f)}{K_0(ak_f)} \tag{3.1}$$

with $$k_f = \sqrt{k^2 n_f^2 - \beta_f^2}$$

$$\alpha_f = \sqrt{\beta_f^2 - k^2 n_c^2}$$

where a is the core radius of the fiber taper at the coupling zone, n_f is the refractive index of the fiber taper, J_0 and J_1 are Bessel function of the zero and first order, while K_0 and K_1 are the modified Hankel functions of zero and first order.

3.5 Coupling between the fiber taper and the cavity

Let's consider excitation of a high Q WGM by a traveling mode in the fiber taper coupler. Assume $E_s(t)$ is the field amplitude of the whispering gallery mode, E_i and E_o in the

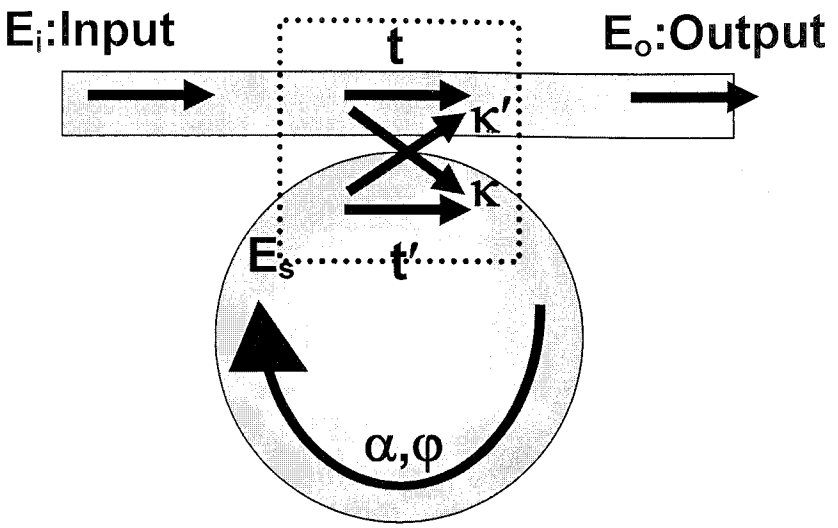

Figure 3.3. Schematic of coupling between fiber taper and cavity

field amplitude of taper mode before and after the cavities, respectively. Let κ describe the coupling of the resonator mode with the fiber taper mode and t be the transmission coefficient of the field amplitude before and after the coupling region. The coupling of light into and out of the resonator can be described by equations [23]:

$$E_s(t) = i\kappa E_i(t) + t' E_s(t - \tau_0) exp(i\varphi - \alpha L/2) \tag{3.2}$$

$$E_o(t) = tE_i(t) + i\kappa' E_s(t) \tag{3.3}$$

where L is the round trip distance traveled by the mode inside the resonator (for the sphere case, $L = 2\pi R_0$), κ is the coupling coefficient, which can be calculated as the normalized

integral of the field of the cavity mode and the fiber taper coupler mode. $\tau_0 = n_s L/c$ is the round trip time of the mode traveling inside the resonator, $\varphi = 2\pi n_s L/\lambda$ is the phase change of the mode after a round trip in the resonator, and α is the linear attenuation in the resonator caused by absorption, scattering and radiation. Because of time reversal symmetry and energy conservation, we have $t = t'$, $\kappa = \kappa'$, and $|t|^2 + |\kappa|^2 = 1$. For high Q cavity, the round trip loss is very small, in other words $\alpha << 1$ and $|\kappa| << 1$. Assume $\omega_0 = 2\pi c/\lambda_0$ is the resonant frequency of the cavity mode. By expanding $E_s(t-\tau_0)$ at t and ignore the high order term, i.e. $E_s(t-\tau_0) = E_s(t) - \tau_0 dE_s(t)/dt$, and replace it in equation 3.2, we obtain

$$\frac{dE_s(t)}{dt} + (\delta_c + \delta_0 + i\Delta\omega)E_s(t) = \frac{i\kappa}{t\tau_0}E_i(t) \tag{3.4}$$

where $\delta_c = \frac{1-t}{t\tau_0}$, $\delta_0 = \frac{c\alpha}{2n_s}$ and $\Delta\omega$ is the frequency shift to the resonant frequency. According to definition of the quality factor, the equation for the field of the mode in the resonator can also be written as

$$\frac{dE_s(t)}{dt} + \left(\frac{\omega_0}{2Q_{ex}} + \frac{\omega_0}{2Q_0} + i\Delta\omega\right)E_s(t) = i\gamma E_i(t) \tag{3.5}$$

where Q_0 is the intrinsic quality factor originating from the loss mechanism in the cavity including scattering from surface, materials absorption due to molecule resonances, or

whispering gallery radiation loss, Q_{ex} is the external quality factor determined by the coupling between the resonator and the coupler and γ is the coupling coefficient of input field coupled into the resonator [18]. Compare equation 3.4 with 3.5, the parameter δ_0 and δ_c can be related to the quality factor:

$$\delta_0 = \frac{\omega_0}{2Q_0} \tag{3.6}$$

$$\delta_c = \frac{\omega_0}{2Q_{ex}} \tag{3.7}$$

At steady state, the time derivative of $E_s(t)$ is equal to zero, which means that

$$E_s(t) = \frac{1}{(\delta_c + \delta_0 + i\Delta\omega)}\left(\frac{i\kappa}{t\tau_0}\right)E_i(t) \tag{3.8}$$

So the field amplitude can be changed by δ_c for a given input power in the fiber taper coupler and it reaches its maximum value at $\delta_0 = \delta_c$. The cavity buildup factor (B) is

$$B = \frac{|E_s|^2}{|E_{in}|^2} = \frac{1}{(\delta_0 + \delta_c)^2}\frac{\kappa^2}{t^2\tau_0^2} = \frac{\lambda_0}{\pi n_s L}\frac{Q_{tot}^2}{Q_{ex}} \tag{3.9}$$

The output field amplitude can be deduced from equation 3.3 and 3.8:

$$E_o(t) = E_i(t) - \frac{1}{(\delta_c + \delta_0 + i\Delta\omega)}\left(\frac{\kappa^2}{t\tau_0}\right)E_i(t)$$

$$= E_i(t) - \frac{2\delta_c}{(\delta_c + \delta_0 + i\Delta\omega)}E_i(t) \qquad (3.10)$$

And the normalized transmission of the cavitiy (T) is given by

$$T = \frac{|E_o(t)|^2}{|E_i(t)|^2} = 1 - \frac{4\delta_0\delta_c}{(\delta_0 + \delta_c)^2 + (\Delta\omega)^2}$$

$$= 1 - \frac{4Q_0Q_{ex}}{(Q_0 + Q_{ex})^2 + (Q_0Q_{ex}\Delta\omega/\omega_0)^2} \qquad (3.11)$$

Both the resonator buildup factor and transmission can be described as function of the quality factors of the resonator, therefore the quality factors are very important parameter to characterize the fiber taper coupled resonator. The intrinsic quality factor is a decided by the resonator itself, while the external quality factor changes with the transmission coefficient t, which changes with the geometry of the coupling (i.e. overlap between the resonator mode and the fiber taper coupler mode). As noted in equation 3.11, the transmission of the resonator is decided by the relation between the intrinsic quality factor Q_{in} and controllable external quality factor Q_{ex}. The intrinsic quality factor Q_{in} is a constant for a given cavity, but the external quality factor Q_{ex} changes with the loading

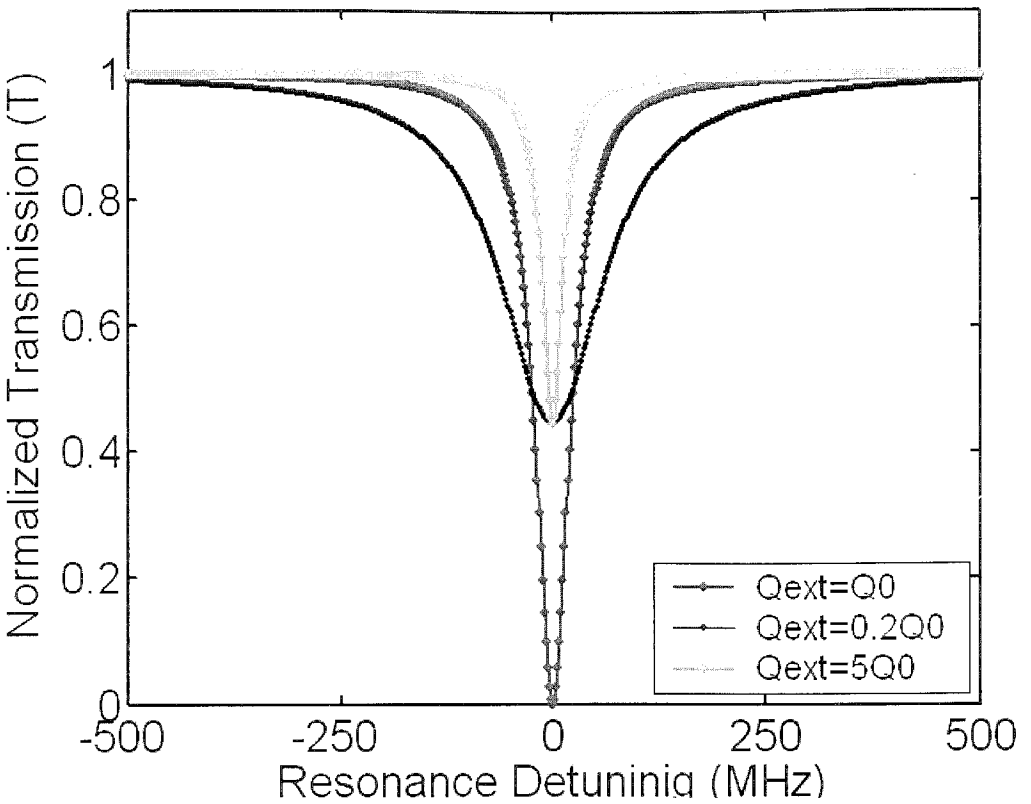

Figure 3.4. Different coupling regimes for a cavity with the intrinsic quality factor Qo of 1×10^8.

conditions. Figure 3.4 is a plot of the resonator transmission T against the phase shift for different loading condition.

When the mode is on resonant in the cavities, the coupling between the waveguide and the resonator can be divided into three regimes:

(1) Under-coupled regime: Due to the loss mechanisms, the resonator has a limited intrinsic quality factor Q_{in}. When the fiber taper is far away from the resonator, the coupling between them is very weak and the overlap between the fiber taper mode and resonator mode is close to zero, i.e. $t \to 1$, and $Q_{ex} \to \infty$. When the fiber taper get closer to the resonator, the overlap of the modes increase, Q_{ex} decreases but still larger than Q_{in}, then the transmission T decrease continuously from unity and approaches zero gradually.

(2) Critical-coupled regime: When the fiber taper get close to the resonator to a such point (critical coupling point) that Q_{ex} is equal to Q_{in}, the normalized transmission is zero, which means that all the input power is coupled into the cavity.

(3) Over-coupled regime: When the fiber taper approaches the cavity further after the critical coupling point, the overlap of the modes become larger and the Q_{ex} decrease further. The normalized transmission becomes smaller than 1 again and it's called over-coupled regime.

Figure 3.4 shows how the transmissions changed by the relation between the intrinsic quality factor and the external quality factor. In addition, as can be seen from equation 3.11, the transmission of the mode is a function of the external quality factor, which changes with the loading condition. Figure 3.5 shows the normalized transmission of the mode as a function of the air gap between the fiber taper coupler and a microsphere with

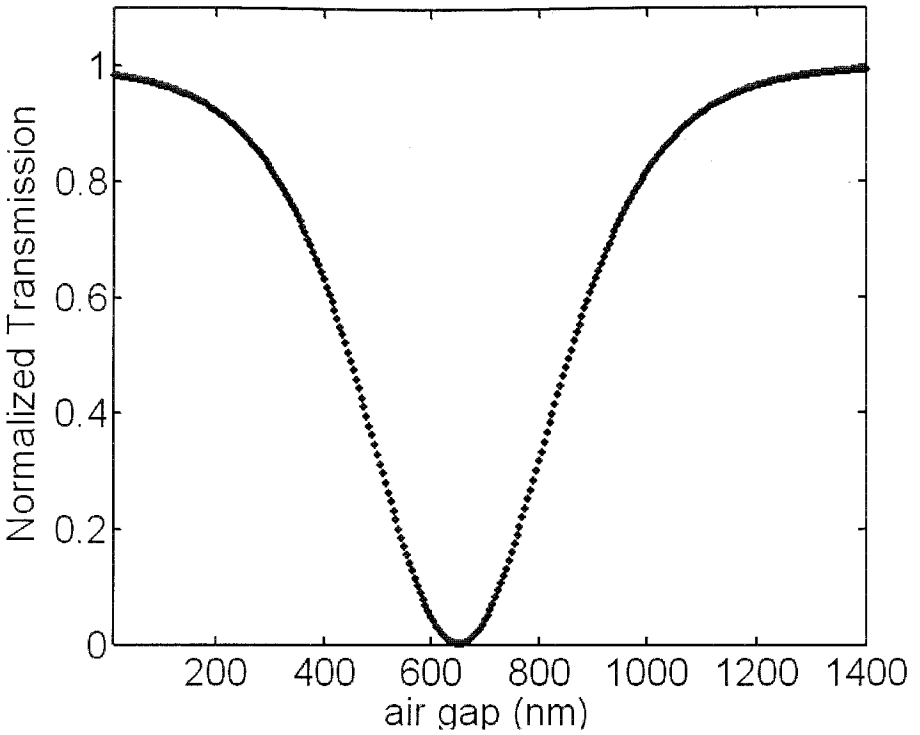

Figure 3.5. Normalized transmission of a fiber taper coupled microsphere versus the air gap between the microsphere and the taper.

diameter of 60 μm. In the under-coupled regime, the transmission decreases gradually when the air gap decreases, and become zero at critical coupling, then it increases if the air gap decrease further.

3.6 Phase matching between the microcavities and the fiber-taper coupler

The amount of power coupled out of the fiber into the sphere is proportional to $exp\left(-\gamma_0 \cdot \Delta\beta^2\right)$, where γ_0 is constant decided by propagation constant β_f and the

diameter of the microsphere and $\Delta\beta$ is the difference in the propagation constants between the fiber mode and the sphere mode. The coupling efficiency is maximized at the phase matching condition, where $\Delta\beta$ is equal to zero.

3.7 Conclusion

Fiber taper is proved to be very efficient in coupling light into and out of the resonator throughout this thesis work. The transmission of the microcavity depends on the configuration, i.e. the air gap between the fiber taper coupler and the microcavity and the phase matching condition between the coupler and microcavity modes. To optimized the coupling efficiency between the fiber taper and the microcavities, phase matching condition need to be satisfied.

Chapter 4

OPTICAL MATERIALS BY SOL-GEL PROCESS

4.1 Introduction

The sol-gel method is a wet-chemical synthesis technique for preparation of oxide gels, glasses, and ceramics at low temperature. It's based on control of hydrolysis and condensation of alkoxide precursors. As early as the mid-1800s, interest in the sol-gel processing of inorganic ceramics and glass materials has begun with Ebelman and Graham's studies on silica gels [24]. The investigator recognized that the product of hydrolysis of tetraethoxysilane (TEOS) under acidic conditions is SiO_2. In the 1950s and 1960s Roy and co-workers used sol-gel method to synthesize a variety of novel ceramic oxide compositions with very high levels of chemical homogeneity, involving Si, Al, Zr, etc, which couldn't be made using traditional ceramic powder methods [25-28]. It's possible to fabricate ceramic or glass materials in a variety of forms, such as ultra-fine powers, fibers, thin films, porous aerogel materials or monolithic bulky glasses and ceramics [29]. Since then powders, fibers, thin films and monolithic optical lens have been made from the sol-gel glass.

4.2 An overview of sol-gel process steps

The sol-gel process, as the name implies, involves transition from a liquid 'sol' (colloidal solution) into a 'gel' phase [30]. Usually inorganic metal salts or metal organic compounds such as metal alkoxide are used as precursors. A colloidal suspension, or a 'sol' is formed after a series of hydrolysis and condensation reaction of the precursors. Then the sol particles condense into a continuous liquid phase (gel). With further drying and heat treatment, the 'gel' is converted into dense ceramic or glass materials. Generally three reactions are used to describe the sol-gel process: hydrolysis, alcohol condensation and water condensation. Because water and alkoxides are immiscible, alcohol is commonly used as co-solvent. Due to the presence of the co-solvent, the sol-gel precursor, alkoxide, mixes well with water to facilitate the hydrolysis.

$$-\overset{|}{\underset{|}{Si}}-OR + H-OH \underset{\text{Re esterification}}{\overset{\text{Hydrolysis}}{\rightleftharpoons}} -\overset{|}{\underset{|}{Si}}-OH + R-OH \qquad (4.1)$$

During the hydrolysis reaction, the alkoxide groups (OR) are replaced with hydroxyl group (OH) through the addition of water. Subsequent condensation reaction involving silanol group (Si-OH) produces siloxane bonds (Si-O-Si) with by-product of water (water condensation) or alcohol (alcohol condensation). As the number of siloxane group increases, they bridged with each other and a silica network is formed. Upon drying, the solvents that are trapped in the network are driven off. With further heat treatment at high temperature, the organic residue in the structure is taken out, the interconnected pores collapse and a densified glass or ceramics is formed.

4.2.1 Hydrolysis and condensation

Although hydrolysis can occur without additional catalyst, it has been observed that with the help of acid or base catalyst the speed and extent of the hydrolysis reaction can be enhanced. Under acid conditions, the alkoxide group is protonated rapidly. As a result, electron density is withdrawn from the silicon atom, making it more electrophilic with partial positive charges. Therefore it's more susceptible to be attacked by the nucleophile, water molecule. Subsequently a penta-coordinated transition state is formed with SN2 type characters, where there is simultaneous attack of the nucleophile and displacement of the leaving group. When the nucleophile attacks the center atom, Si, it's on the opposite side to the position of the leaving group, R-OH. Finally the transition state decays by breaking of the Si-OHR bond and ends up with an inversion of silicon configuration as shown in equation 4.2. The acid-catalyzed mechanism can be described as following:

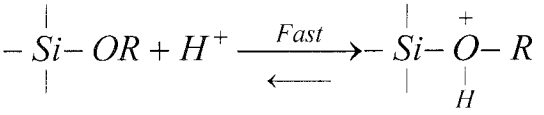

(4.2)

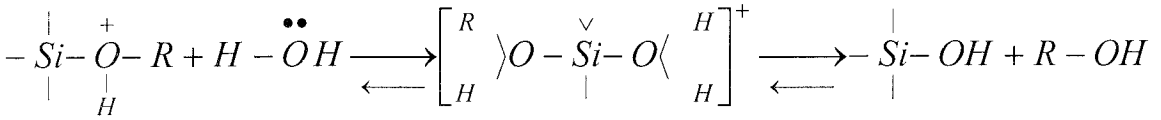

Under basic conditions, the hydroxyl anion works as nucleophile and attacks the silicon atom. Again, an SN-2 type mechanism has been proposed in which OH displaces OR

group with inversion configuration of the silicon tetrahedron. The mechanism of the base-catalyzed mechanism can be described as following:

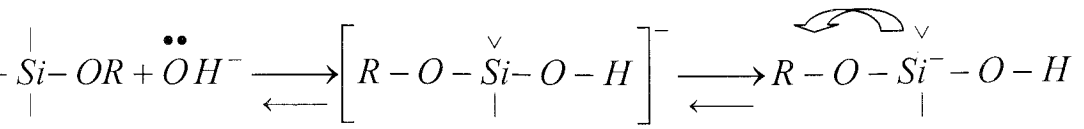

(4.3)

4.2.2 Gelation

In the gelation step, alkoxide gel precursor undergoes polymerization (condensation) reaction with by-product of water or alcohol. Similar to hydrolysis, the condensation reaction is also affected the acid/base catalyst. With the existence of acid catalyst, weakly-crosslinked polymer is formed and can easily aggregate after drying yielding low-porosity microporous structure. On the contrary, if base catalyst is used, discrete highly branched clusters are formed and lead to a mesoporous structure after gelation.

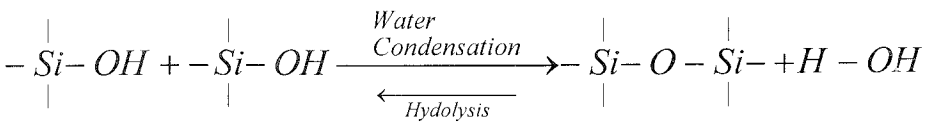

(4.4)

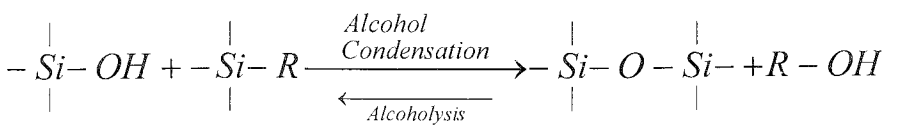

(4.5)

4.2.3 Ageing

The continuing chemical and physical changes during ageing after gelation are very important. During this process, further cross-links continuous, the gel shrinks as the covalent links replace non-bonded contacts and the pore sizes and pore wall strengths change with the evolution of the gel's structure.

4.2.4 Drying

The gel has a high ratio of water and three dimensional inter-connected pores inside the structure. Before the pore is closed during the densification process, drying is needed to remove the liquid trapped in the interconnected pores. On the other hand removal of the liquid from the tiny pores causes significant stress resulting from inhomogeneous shrinkage. Therefore the main problem that had to be overcome is cracking due to the large stress in the structure. For small cross sections, such as powder, coating, or fiber, the drying stress is small and can be accommodated by the materials, so no special care is needed to avoid cracking for those sol-gel structures. While for monolithic objects greater than 1 cm, drying stress developed in ambient atmosphere can introduce catastrophic cracking, as a result control of the chemistry of each processing step is essential to prevent cracking during drying.

4.2.5 Densification

Although there are many applications of sol-gel silica prepared and dried at or near room temperature (especially those involving trapping functional organic or biological molecules with the gel pores), heat treatment of the porous gel at high temperature is necessary for the production of dense glass or ceramics from the gel silica. After the high temperature annealing, the pores are eliminated and the density of the sol-gel materials ultimately becomes equivalent to that of the fused glass. The densification temperature depends considerably on the dimension of the pores, the degree of connection of the pores, and the surface areas in the structure [24].

4.2.6 Advantages and limitations of sol-gel method

Sol-gel method is a very flexible way to fabricate glass/ceramics under mild condition. From the introduction above, the advantages of the sol-gel method become apparent [17, 31-33]:

1. Sol-gel method involves wet chemical synthesis of materials, so the composition of the materials can be tailored at molecular level. As a result, stoichiometrical homogeneous control of the doping is easily achieved.

2. Since liquid precursors are used it's possible to cast the glass and ceramics in a range of shapes, such as thin film, fibers, and monoliths, etc, without the need of machining or melting.

3. The precursors, such as metal alkoxides, with very high purity are commercially available, which makes it easy to fabricate materials with high quality.

4. It's cost effective because the temperatures required in the process are low, close to room temperature, and no delicate vacuum system is needed.

Despite all the advantages, sol-gel method still has some limitation. Solvents, such as alcohol and water, are involved in the process, so it's not appropriate for fabrication which is very sensitive to solvents. Furthermore, stress induced cracks upon drying are not unusal and can't be healed after densification. Very careful attentions are needed to avoid cracking. Despite of the disadvantages, sol-gel method is a very mild and flexible method to fabrication materials that possess properties not attainable by other methods. It inspires us to further investigate and modify the method to exploit its maximum value in application.

4.3 Fabrication of sol-gel films for photonic application

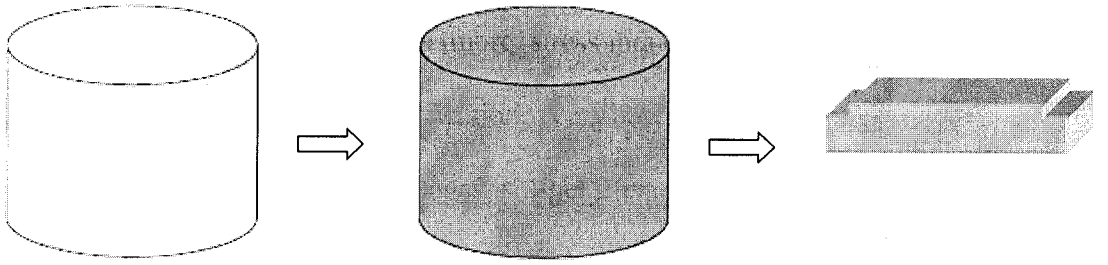

(a) (b) (c)

Figure 4.1. Schematic of fabrication of sol-gel films on a substrate: (a) organometallics and dopants in alcohol solvents (b) hydrolysis of organometallics in water (c) sol-gel films on a substrate by dip-coating or spin-on methods.

Figure 4.1 shows a schematic of the preparation procedure of sol-gel films on a glass or silicon substrate. First, organometallics (such as metal alkoxides) and dopants are put in an alcohol solvent, such as ethanol or isopropanol. Then the water is added to hydrolyze the organometallics. After hydrolysis and condensation reaction for certain time (ranges from several hours to several days under different condition), a viscous gel is formed. After aging the sol solution at room temperature, a layer of sol-gel film is deposited on a substrate by spin-on or dip-coating method. The thickness of the films is decided by the viscosity of the sol solution, the spin speed for the spin-on method, or dipping time for the dip-coating method.

4.4 Characterization of sol-gel silica film with Fourier Transform Infrared Spectrometer (FTIR)

Infrared spectroscopy is the study of the interaction of infrared light with matter [34]. When infrared radiation interacts with matter it can be absorbed, causing the chemical bonds in the materials to vibrate. Chemical structures within molecules, known as functional groups, tend to absorb infrared radiation in the same wavenumber range regardless of the structure of the rest of the molecules. The correlation between the wavenumber and molecule structures makes it possible to identify the structure of unknown molecules. For instance, the peaks around 3000 cm^{-1} are due to C-H stretching bond.

A series of thin films were annealed at different temperatures, ranging from 200° C to 1200° C. A Fourier Transform Infrared (FTIR) microspectroscope was used to compare the

structure of sol-gel silica with that of thermally grown silica. Figure 4.2 shows the evolution of the reflectance infrared spectra as a function of annealing temperature. The characteristic

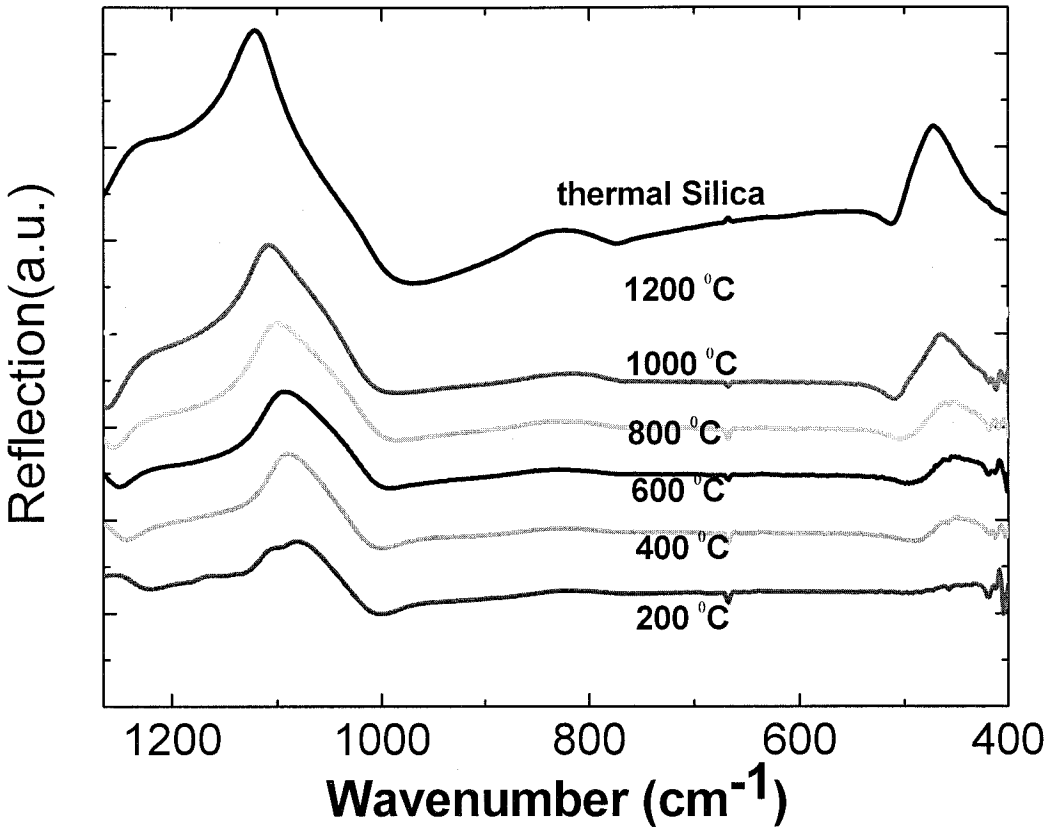

Figure 4.2. FTIR spectra of thermal silica and sol-gel silica samples prepared with different heat treatment.

vibrational bands of silica were found in the spectra of sol-gel silica. Compared with FTIR spectrum of thermally grown silica film, the absorption band, which correspond to Si-O-Si bending (near 460 cm-1), Si-O-Si symmetric stretching (near 810 cm-1), and Si-O-Si

asymmetric stretching (near 1105 cm^{-1}) are clearly shown in figure 4.2 [35]. When the annealing temperature is 200° C, a weak absorption band at ~964 cm^{-1} is observed, which is attributed to stretching vibration of silanol Si-OH hydrogen bonded groups. The excited Er^{3+} can be quenched through non-radiative relaxation by coupling to a quenching site, such as hydroxyl group OH^-. This absorption band disappears at temperature of 600 °C. In addition, compare with the spectra of others, the spectra of the sample heated at 1000° C and 1200° C have stronger, broader and blue-shifted Si-O-Si bands. The changes in the spectra indicate the complete densification of silica films after heat treatment [36]. Furthermore, as the temperature is increased, the absorption band due to Si-O-Si bending becomes stronger. It shows that the crosslink between silica chains are improved gradually due to progressively enhancement of condensation reaction under higher densification temperature. The spectra of the samples heated at 1000° C and 1200° C are similar to that of the thermally grown silica.

4.5 Effect of anneal temperature on etching rate of sol-gel film in buffered Fluoride acid (HF)

To further probe the change of the microstructure of the glass, hydrofluoric acid (HF) etching was used to monitor the subtle change of the glass after different heat treatment. The silicate structure with smaller Si-O-Si bond angles are more vulnerable to HF than structure with larger bond angles [37]. During the etching rate test experiments, the etching rate of films annealed at temperature lower than 600° C has etching rate of more than 1000 Å/s. When samples are annealed at 1000° C and 1200° C, the etching rate

decreases to 15 Å/s, which is almost the same as that of the thermally grown silica (13 Å /s). This result is consistent with the blue shift of the Si-O-Si bond in FTIR which indicates an increase of the average Si-O-Si bond angles [38]. The etching rate experiment confirms that the microstructure of the sol-gel silica annealed at temperature as high as 1000 °C is the very close to that of the thermally grown silica.

4.6 Conclusion

In this work, silica thin film has been prepared by the sol-gel method. A Fourier Transform Infrared Spectroscopy (FTIR) is used to analyze the composition of the silica sol-gel prepared in the lab. It shows that the sol-gel silica annealed at temperature at or above 1000 °C is very similar to thermal silica. Furthermore the etch rate in buffered HF solution of thin films annealed at different temperature was investigated. The etch rate of the films has been shown to change by almost two orders of magnitude for undensified and densified sol-gel films. This result can later be used to selectively coat the surface of a microtoroid cavity on a silicon chip which will be discussed in chapter 6.

Chapter 5

SURFACE FUNCTIONALIZATION OF SILICA MICROSPHERE RESONATORS

5.1 Introduction

Microcavities formed by surface tension (droplets and solid spheres or spheroids) can exhibit quality factors in excess of one billion and are of interest in cavity QED, nonlinear optics, photonics and sensing. When silica microspheres are doped using any number of rare earth ions, ultra-low threshold micro lasers are possible [3, 12, 39]. The preparation of these devices requires acquisition of bulk samples of rare-earth doped glass that are subsequently processed into a spherical cavity. Here, an alternative to this process is presented in which ready-made microspheres of undoped silica serve as a base resonator structure and gain functionalization of the surface is performed using an erbium-doped sol-gel film. Sol-gel films are readily doped with a number of different rare earth ions [40-42], as well as other materials [43, 44], thereby making this a more versatile method for preparation of active microspheres. In addition, the sol-gel preparation process allows for precise control of dopant concentration, making possible the study of a range of inversion concentrations. Finally, it will be shown that the thin film nature of the gain layer has an important effect on laser dynamics.

5.2 Erbium doped silica glass

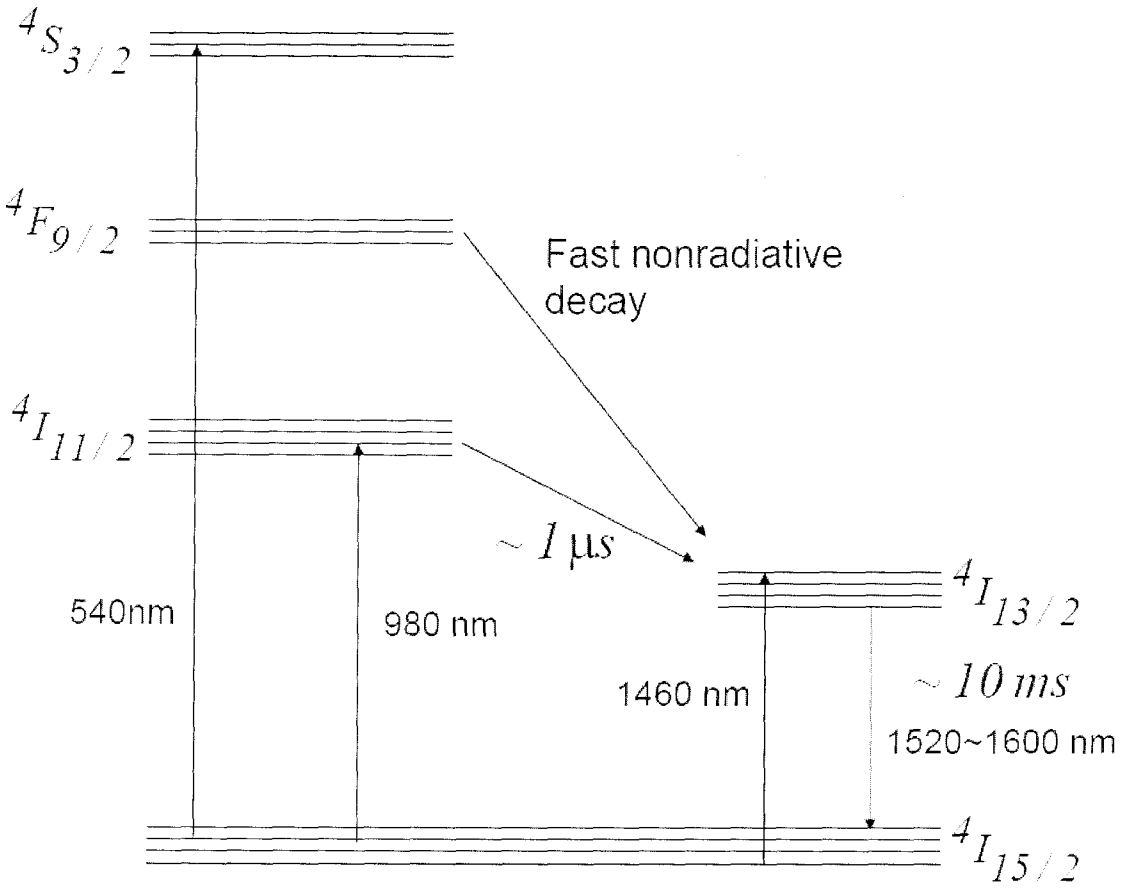

Figure 5.1. Schematic representation of the Er^{3+} intra 4f Energy level.

Rare earth atoms are divided into two groups: the lanthanides with atomic number from 57 to 71, and the actinides with atomic number from 89 to 103. The vast majority of rare earth doped amplifiers and lasers use lanthanides elements as gain medium. Among them erbium (with atomic number 68) doped amplifiers and lasers are especially interesting due to the erbium 4*f* transition $^4I_{13/2} \rightarrow {}^4I_{15/2}$ which falls in the 1.5 μm telecommunication window. Erbium usually takes the ionic form, in particular the trivalent state, Er^{3+}. The atomic

configuration of the Er^{3+} is $(Xe)4f^{11}$, where (Xe) represents a Xenon core. The shielding of 4f electron from the environments by the outmost 5s and 5p electrons is responsible for erbium's rich optical spectrum. Due to various atomic interactions between electrons, the 4f electron spread in different energy level. A further splitting of the energy level arise when erbium are doped in a glass host materials. The local electric field in the glass matrix breaks the spherical symmetry of the rare earth ions. Thus the degeneracy of the 4f atomic states will be lifted to some degree and the splitting is referred to as Stark splitting of the energy level. As can be seen from the energy level diagram in fig. 5.1, the Erbium ion can be excited by pump wavelength of 1.48 or 0.98 μm.

5.2.1 Er^{3+}-Er^{3+} interactions

The intra-4f transitions are 'forbidden electronic dipole' in nature, so the Er^{3+} has very small absorption/emission cross section, on the order of 10^{-21} cm^2. It has been found that when the Er^{3+} concentration is high in order to obtain adequate gain, undesirable effect occurs. These effects can be related to certain Er^{3+}-Er^{3+} interactions. When the local concentration of Er^{3+} becomes high enough, it's not valid to assume that each ion is isolated and independent of its neighbors. On the contrary, when two ions get close enough, energy can migrate from one ion to another, which has a negative impact on the energy-donor ions. There are several erbium ion interactions, among which two mechanisms prevail.

Cooperative Upconversion

When ions 1 and 2 are both in the upper laser level $^4I_{13/2}$, The radiative lifetime around 10 ms in a silica glass gives closely spaced neighbors enough time to interact. During the upconversion process, ion 1 transfers energy to ion 2 and drops back non-radiatively to the ground state. At the same time, ion 2 is promoted to higher energy level, usually $^4I_{9/2}$, from where it rapidly relax non-radiatively back to the excited state $^4I_{13/2}$ or relax radiatively to the ground state with emission of one photon at 540 nm, which corresponds to the green light observed throughout this work. In this case, the ions are independent which means that if one ion in the excited state $^4I_{13/2}$ does not prevent the neighboring ion from being excited to the state $^4I_{13/2}$. Up-conversion depends on whether both ions are exited to the $^4I_{13/2}$ state.

Pair induced quenching

Similar to the cooperative up-conversion it involves energy transfer between two excited ions. The ions are so closely coupled that one ion will transfer its energy to the other one in a time scale that is significantly faster than the pump rate. But in this case the ions are no longer considered to be independent, and the ions should be treated as paired ions, instead of single ions. This effect will be discussed in details in chapter 8.

5.3 Fabrication of silica microsphere

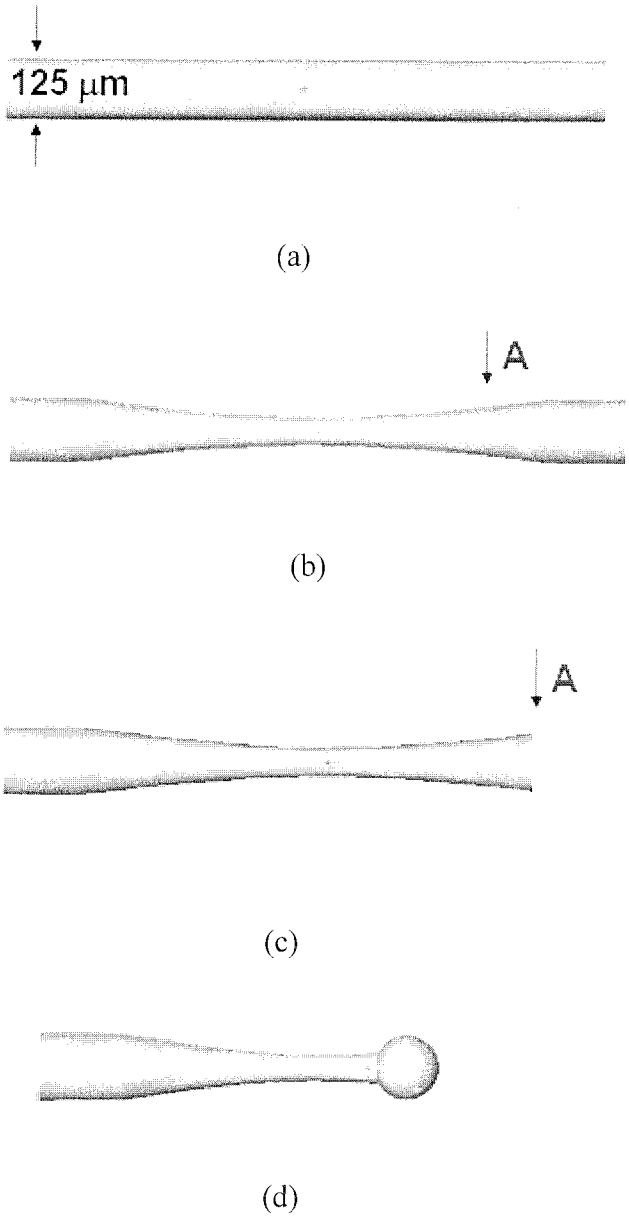

Figure 5.2. Illustration of fabrication of the microsphere for a silica fiber. (a) single mode silica fiber (b) A fiber taper is formed (c) Use very strong CO_2 laser to irradiate at A, at the same time pull the fiber quickly to break the fiber taper at spot A. (d) Irradiate the fiber tip with CO_2 laser, and due to surface tension a microsphere is formed with the left fiber as a supporting stem.

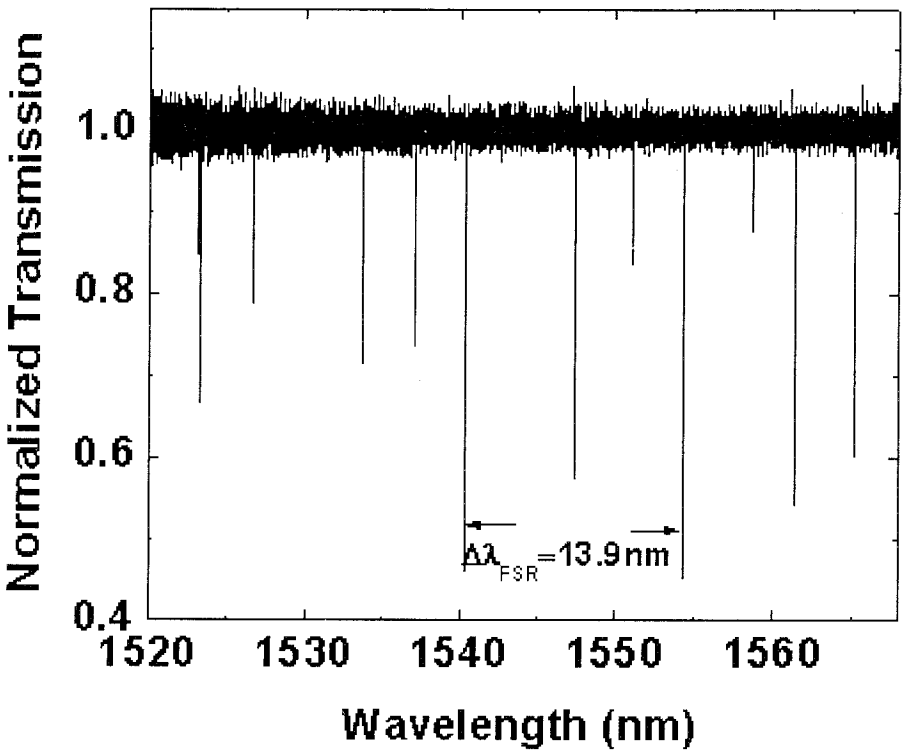

Figure 5.3. Transmission spectrum of a fiber taper coupled microsphere with diameter of 39 μm.

Silica has a very low loss in the 1550 nm band and is therefore an excellent material for preparation of ultra-high-Q microspheres. In addition, because silica has a strong absorption for CO_2 laser at 10.6 μm, a SYNRAD 10W CO_2 laser is used a as a heat source during the microsphere fabrication process. A CCD camera connected with a display screen is used to monitor the microsphere fabrication process. Figure 5.2 shows an illustration of the fabrication of the ultra-high-Q microspheres. First the plastic cladding of a standard silica optical fiber is removed and the core region with a diameter of 125 μm is

exposed to the air. Some volatile solvent, such as ethanol or isopropanol, is used to clean the surface of the core. Then the CO_2 is used to heat certain region of the fiber, simultaneously the fiber is pulled gradually until the waist diameter is about 5~20 μm. Then the heating point moves to fiber region **A** which is a little shifted from the waist area as show in fig. 5.2c. A very strong CO_2 laser is used to irradiation at **A** while the fiber is pulled quickly, as a result the fiber can not sustain the quick pulling and breaks at the soft point **A**. Afterwards, the fiber tip is heated and a microsphere is formed due to surface tension. The left fiber works as a supporting stem for the microsphere. Figure 5.3 shows a transmission spectrum of a fiber taper coupled microsphere.

5.4 Surface functionalization of microsphere

Figure 5.4 shows a schematic for surface functionalization of a silica microsphere. First the sol gel starting solution was prepared by hydrolyzing tetraethoxysilane (TEOS) in water under acid conditions (pH~1) with isopropanol as the co-solvent. Er ions were introduced by adding $ErNO_3 \cdot 5H_2O$ with a weight ratio of $ErNO_3 \cdot 5H_2O$/TEOS~0.2wt% [45]. The mixture was then stirred vigorously at 70°C for ten hours. After aging the sol solution at room temperature for another ten hours we immersed silica microspheres in the solution. The initial pure-silica microspheres were formed by heating the end of a tapered fiber tip with a CO_2 laser as described by Knight [46]. Multiple process cycles were used to build up a desired layer thickness. Each process cycle consisted of dipping the sphere for 20 minutes

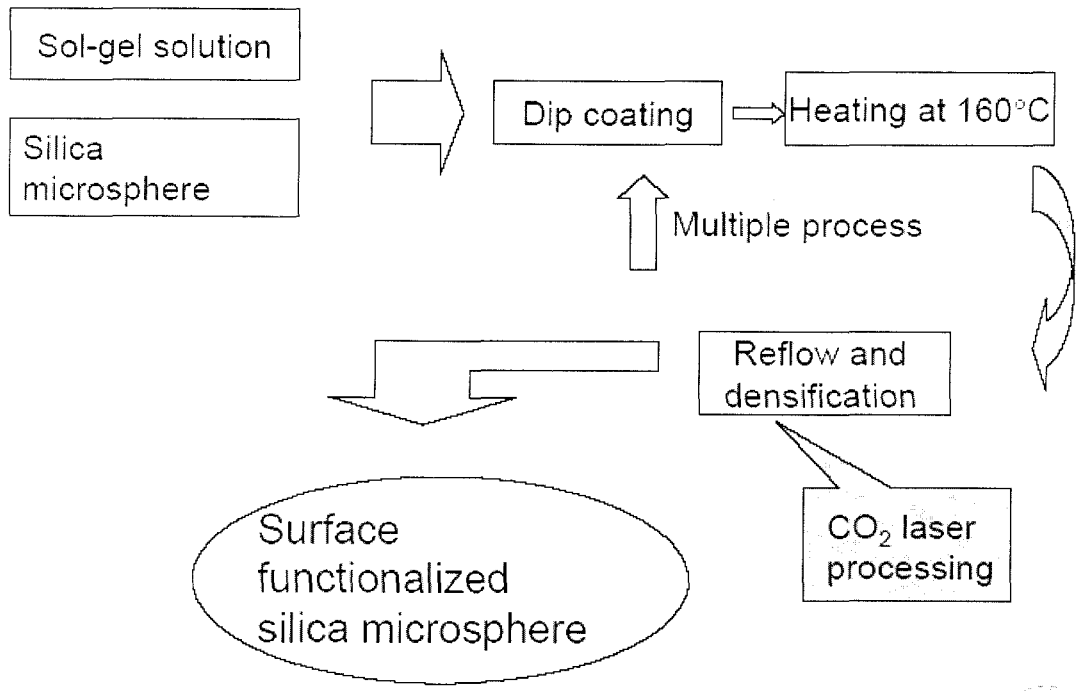

Figure 5.4. Schematic of surface functionalization of silica microsphere.

in the sol gel solution followed by heating in an oven at 160°C for 10 minutes. The layer thickness obtained in a processing cycle depended on the dipping time and solution viscosity. In this experiment, the build-up rate was estimated to be about 0.3 μm/cycle (determined by observation of layer thickness after multiple cycles). Every two cycles, the spheres were irradiated using the CO_2 laser for several seconds. The laser intensity was sufficient to induce flow and densification of the sol gel layer. In addition, micro-cracking that was present in the sol gel surface was annealed out by this process. By repeating this process, the coating thickness was varied. Silica spheres ranged in diameter from 50 to 80

μm and the coating thickness was varied from 1 to tens of microns. The Er^{3+} doping concentration of the resulting doped shell was estimated to be around 10^{19} cm^{-3}.

5.5 Coupling between fiber taper and microsphere

Optical coupling to the spherical microcavities both for the purposes of pumping as well as laser output extraction was performed using optical-fiber tapers. Taper coupling has been used previously to demonstrate microsphere-lasers in the telecommunication band. It makes possible the resonant excitation of specific whispering gallery modes and efficient pumping of a small gain volume within the sphere. As shown in fig. 5.5, the pump power was transmitted and coupled into the microsphere from one end of the fiber taper and the laser output was extracted and transmitted to some optical receivers connected to the other end. The typical waist diameter of the tapers used to couple pump power and collect laser emission was around 1.6 μm.

Whispering gallery mode (WGM) resonances correspond to light trapped in circulating orbits just within the surface of the spheroidal particle [47, 48]. The modal indices are similar to those used to characterize simple atomic systems with radial (n), orbital (l), azimuthal (m) and polarization (TE or TM) indices needed to completely specify a mode.

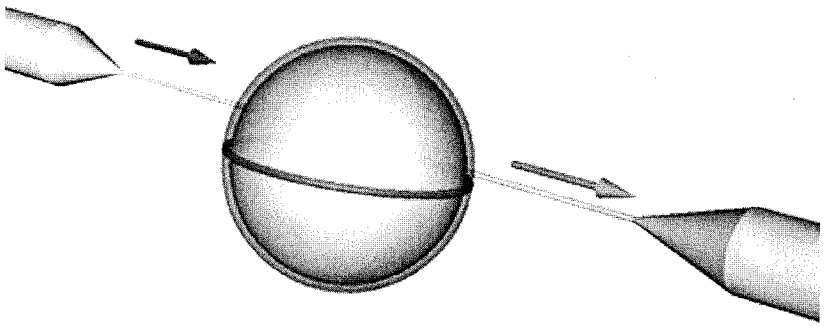

Figure 5.5. Schematic of a thin film coated microsphere laser coupled with a fiber taper. Red and green arrows represent input pump and output lasing waves, respectively.

In particular, the angular distribution of the modes is given by the spherical harmonics $Y_{lm}(\theta,\varphi)$ (see figure 5.6) and the WGM modes with best spatial overlap to the fiber taper have their power concentrated near the equatorial plane ($m \approx l$) with a low radial coordinate $n \approx 1$. These same modes are also best able to pump the active medium surface layer over a radial thickness given approximately by the material wavelength of the pump band. The pumped region will overlap with the emission band modes enabling lasing action. For a surface layer thickness somewhat less than the radial width of the pump mode, nearly complete inversion is expected within annular shaped equatorial bands. Conversely, when the thickness is substantially greater than the pump-mode radial width there will remain

unpumped regions that can provide saturable absorption to the longer-wavelength lasing modes. In addition to modifying the threshold characteristics, saturable absorption is known to modify lasing dynamics such that pulsation behavior is possible. This distinction between thick and thin shell behavior is investigated below.

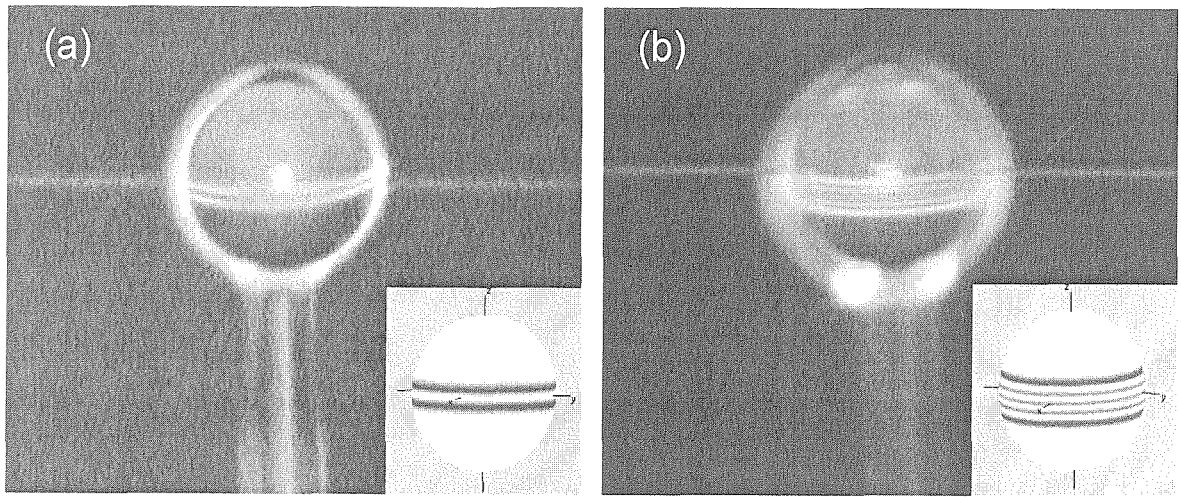

Figure 5.6. Image of the WGMs in the taper-sphere coupling zone: (a) l-m=1. (b) l-m=4. The green rings are up-converted photoluminescence. The inset shows spherical harmonics Ylm(θ,φ) for (a) l-m=1 and (b) l-m=4

5.6 Laser performance

The pump wave was in the 980nm wavelength band, and provided by a tunable single frequency, narrow-linewidth (<300kHz), external-cavity laser. The pump wavelength was scanned initially to survey pumping modes. These were observable by monitoring the transmission versus tuning and also by using a camera to monitor green, excited-state emission from the sphere as the pump laser tuned into resonance with various pump modes.

Figure 5.6 shows representative lateral emission distributions observed for different WGMs in the sphere-taper coupling zones. The pump power coupled to the sphere was measured as the difference of the launch power into the taper and the transmitted power after the taper.

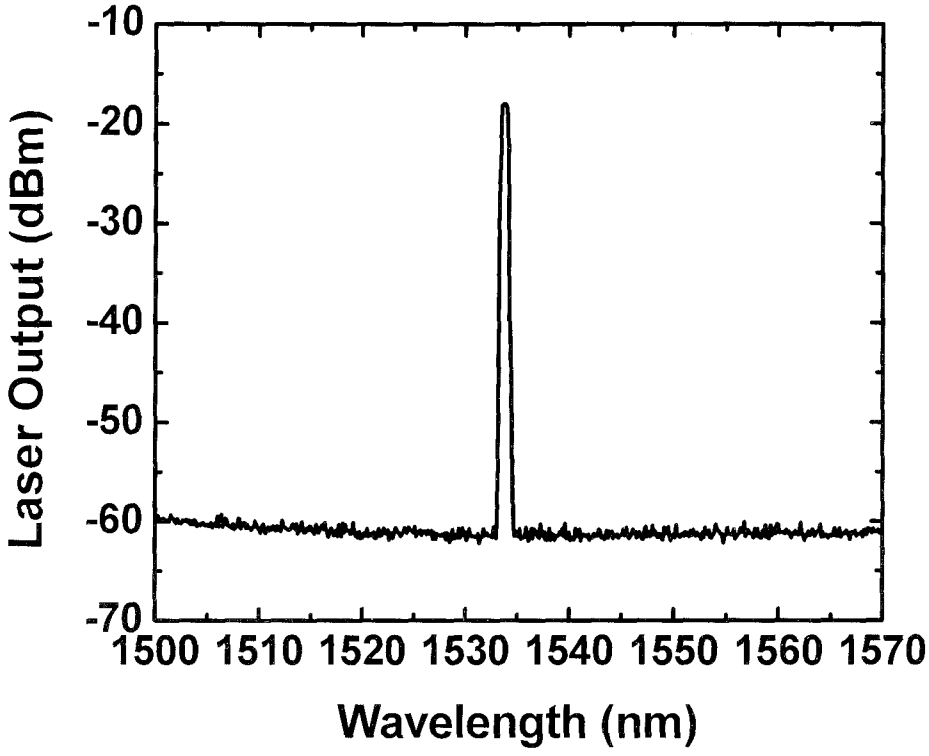

Figure 5.7. Emission spectrum of a microsphere laser

A typical laser spectrum for cw operation is presented in figure 5.7. This was measured using an optical spectrum analyzer with resolution bandwidth setting of 0.5nm. Multi-line operation was also observed and depended upon the pump wavelength selected. However,

by tuning the pump wave it was always possible to achieve single line operation. This is believed to result from strong spatial mode selection possible when the so-called whispering gallery mode (equatorial ring orbit) is resonantly pumped. Figure 5.8 shows the laser output versus the pump power absorbed by the microsphere for cw operation. The

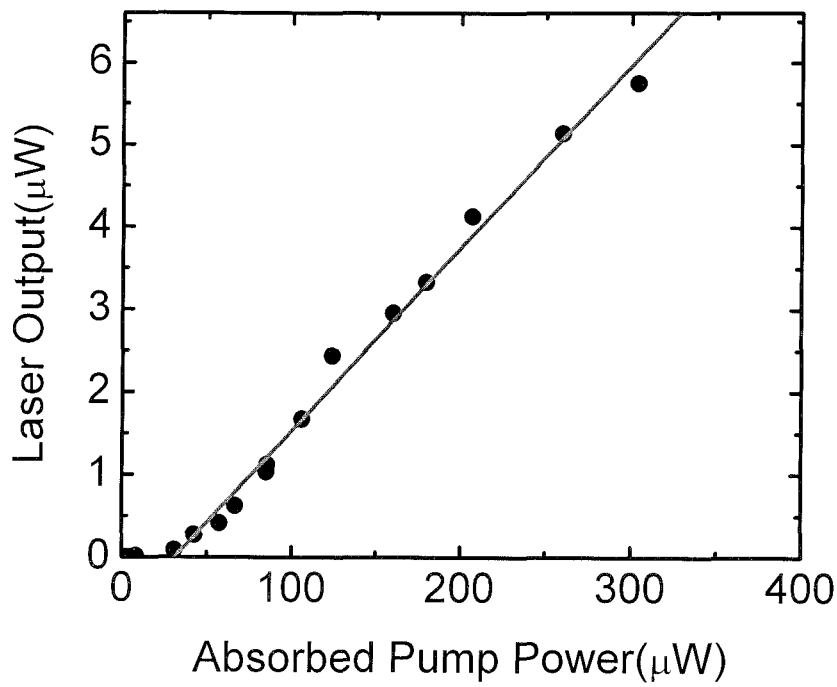

Figure 5.8. Laser output power versus absorbed pump power in the microsphere laser.

threshold was estimated to be around 28μW and the laser reaches an output power of 6μW. Above threshold, the laser output power varied linearly with absorbed pump power. A laser output power of up to 10μW was observed for single-mode pm operation. For convenience

during the experiments, the sphere was in contact with the taper (i.e., zero air gap). This greatly restricted control of coupling and potentially limited the optimization of laser output power. In addition, optimal coupling of the pump requires balancing of taper loading with round-trip loss (dominated by erbium absorption in the shell layer). Optimal coupling of laser emission also requires optimization of loading, but not necessarily for the same conditions as for the pump. Other factors affecting coupling are phase matching and field overlap between the taper and sphere modes in both the pump band and the emission band.

5.7 Effect of doping thickness on the laser dynamics

Erbium-doped fiber lasers have shown pulsing operation. If a saturable absorber effect is incorporated in the rate equations, a self-pulsing operation can be expected under certain circumstance. There are two possible saturable absorber mechanisms for the Er^{3+}-doped microcavities. First, there may be a small amount of rare earth which has absorption line close to the Er^{3+} laser but remain unpumped. The second possibility is a group of clusters where the space between the neighboring Er^{3+} is so close that they can exchange energy nonradiatively, subsequently some Er^{3+} originally pumped remain effectively unpumped and serve as saturable absorbers. Both effects drain the upper laser level and may lead to instability of the laser output.

Both continuous wave (cw) operation and pulsation mode (pm) operation were possible by controlling the sol gel coating thickness. CW laser operation was observed with coating thickness in the range of 1 micron, while pm laser operation was possible for coatings

around or above 5 microns in thickness. The thickness of the doped layer was estimated by observing the thickness of the sphere both before and after the coating process.

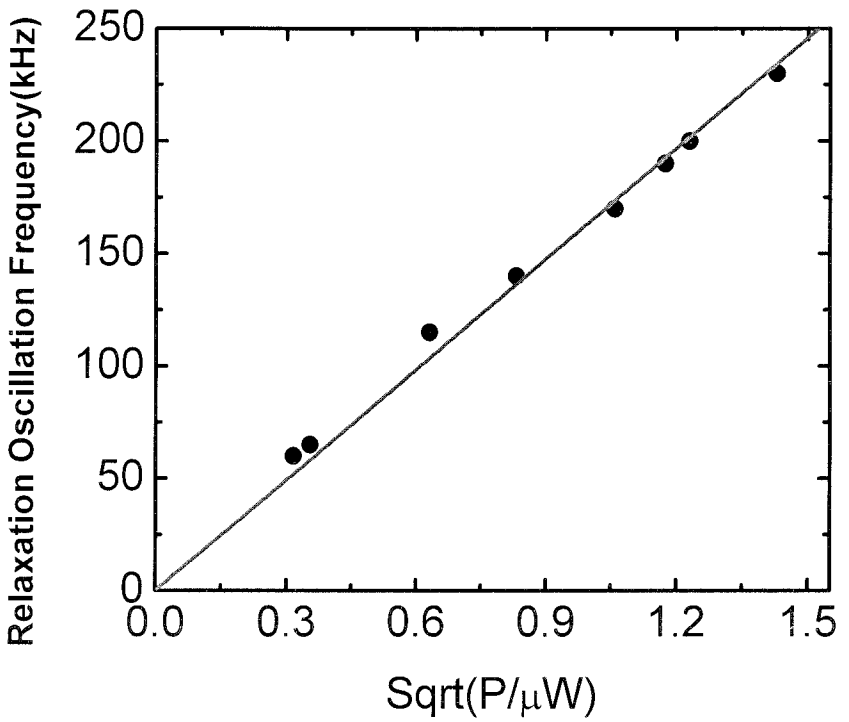

Figure 5.9. Measured pulsation frequency versus the square root of the laser output power P

Figure 5.9 shows the measured pulsation frequency versus the square root of the laser output power for pm operation. The frequency was in a range from tens of kilohertz to several hundred kilohertz. An electrical spectrum analyzer was employed for this

measurement. The observed linear behavior is consistent with un-damped relaxation oscillations [49]. The ability to induce pm operation by control of shell thickness is attributed to unpumped inner regions of the shell that can provide saturable absorption to the lasing mode. This conjecture is consistent with the observation of pm operation in prior microsphere laser work using bulk-doped glass for sphere fabrication. Azimuthal surface regions can also potentially provide saturable absorption. However, if present here, they were alone insufficient to induce instability.

5.8 Conclusion

In conclusion, we have demonstrated the gain functionalization of silica microspheres using doped sol gel films. This technique provides a way to achieve a range of possible gain media in the microsphere system. Likewise, other possible surface layers that target applications such as nonlinear optics in a micro-cavity may also benefit from this approach [11]. An important feature of the sol gel gain layer is the ability to quench previously observed pulsations in these devices, thereby achieving continuous wave laser operation. For shell thickness in the range of 1 micron, continuous wave laser operation was observed. This behavior as well as the onset of pulsations for thicker active shells is attributed to unpumped and hence saturable absorbing regions that can be present in thick shells.

Chapter 6

SURFACE FUNCTIONALIZATION OF SILICA MICROTOROID RESONATORS ON A SI CHIP

6.1 Introduction

Whispering-gallery type microlasers in which the cavity boundary is defined by surface tension (e.g., spheres and droplets) have attracted much attention because the combination of their very small mode volume and high, cold-cavity Q-factor enables ultra-low-threshold operation [3, 12, 50]. Recently, a new class of ultra-high-Q, surface-tension-induced microcavities fabricated on a silicon chip have been demonstrated. These structures feature a toroidal-shaped cavity and enable the integration of electronics and other functions with ultra-high-Q devices. In this paper we demonstrate surface-functionalization of these devices using erbium-doped sol-gel films. To the authors' knowledge, this is the first demonstration of a wafer-based rare-earth doped microlaser. In addition to being integrable with other optical or electric components, they are directly coupled to optical fiber using fiber tapers.

We have previously applied the surface functionalization method using silica microsphere resonators. Erbium-doped microlasers are especially interesting because their emission band falls in the important 1.5 μm window used for optical communications. However, microspheres, while useful as laboratory demonstration vehicles, are not suitable for integration with other optical or electronic functions. Their properties are also difficult to

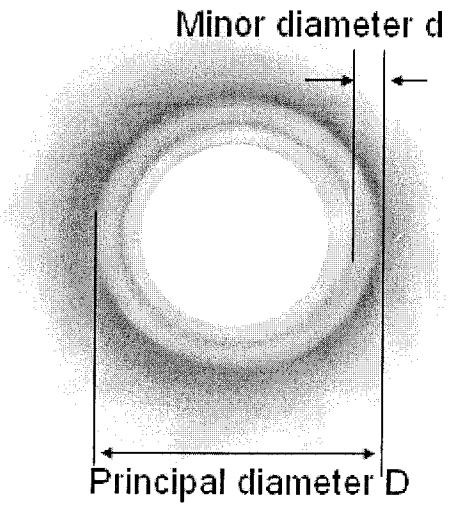

Figure 6.1. Optical micrograph top view of a microtoroid showing principal and minor diameters of the toroid.

control during fabrication. In contrast, microlasers on a chip can be fabricated in parallel and have characteristics that are more easily controllable using wafer-scale processing methods.

6.2 Characterization of Microtoroid cavities

Like all whispering-gallery type microresonators, microtoroids feature optical modes that are confined near the resonator periphery. The thickness of the microtoroid is generally much smaller than the microtoroid diameter. Thus, in contrast to microspheres, these structures support fewer azimuthal modes. This facilitates single-mode operation in the microtoroids. Figure 6.2 shows field intensity distribution of the modes for toroids with the

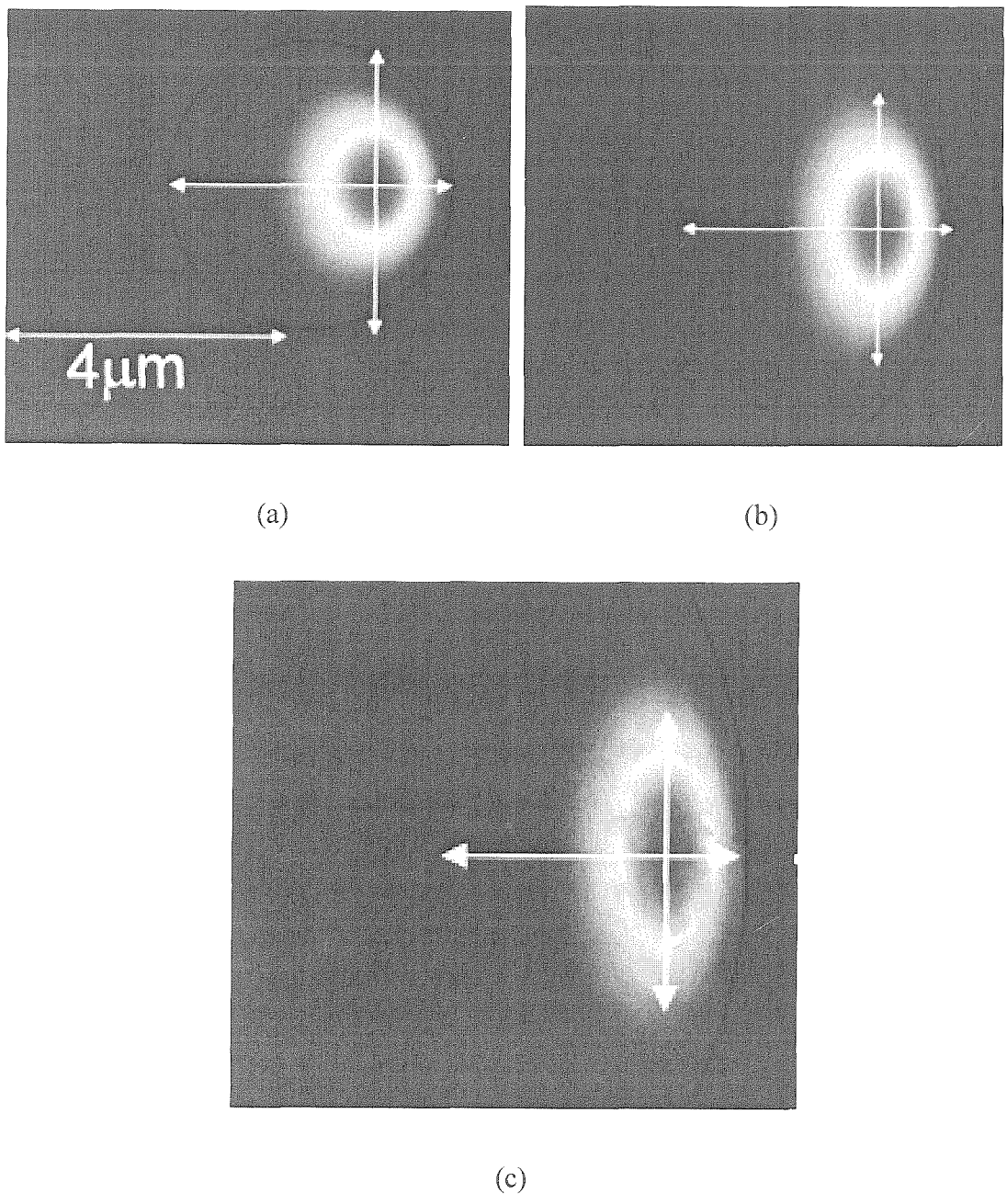

Figure 6.2. Simulation of fundamental TM modes for toroids with minor diameters of (1) 4 μm (b) 8 μm and (c) 16 μm. Their principal diameters are all 70 μm.

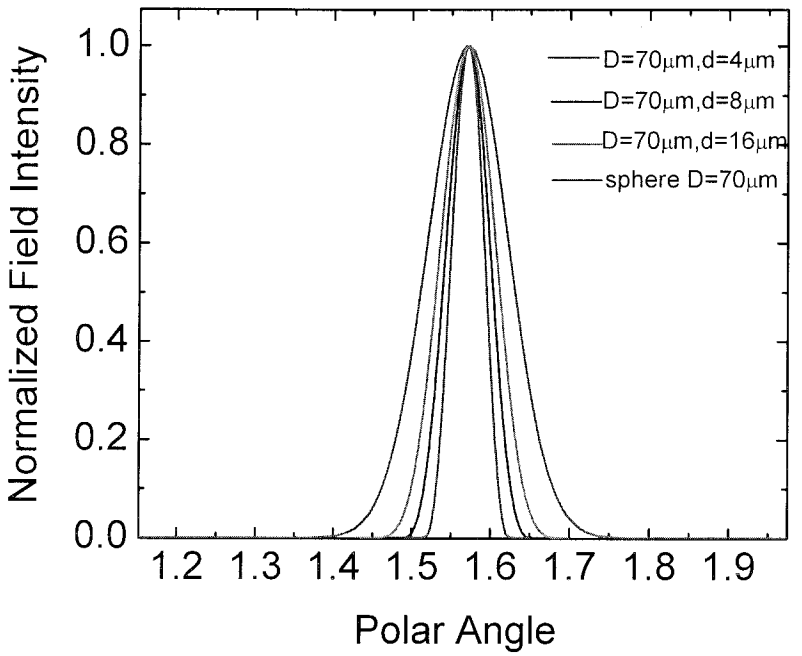

Figure 6.3. Field intensity distributions along the polar direction for different microtoroids.

same principal diameter, but different minor diameters. To further demonstrate the compression effect, in fig. 6.3 we plot the normalized field intensity along the polar direction at a radial location with maximum intensity. The compression of the modes in the polar direction is stronger with decreasing minor diameters. As the minor diameter increase gradually, the mode profile approaches that of the microsphere.

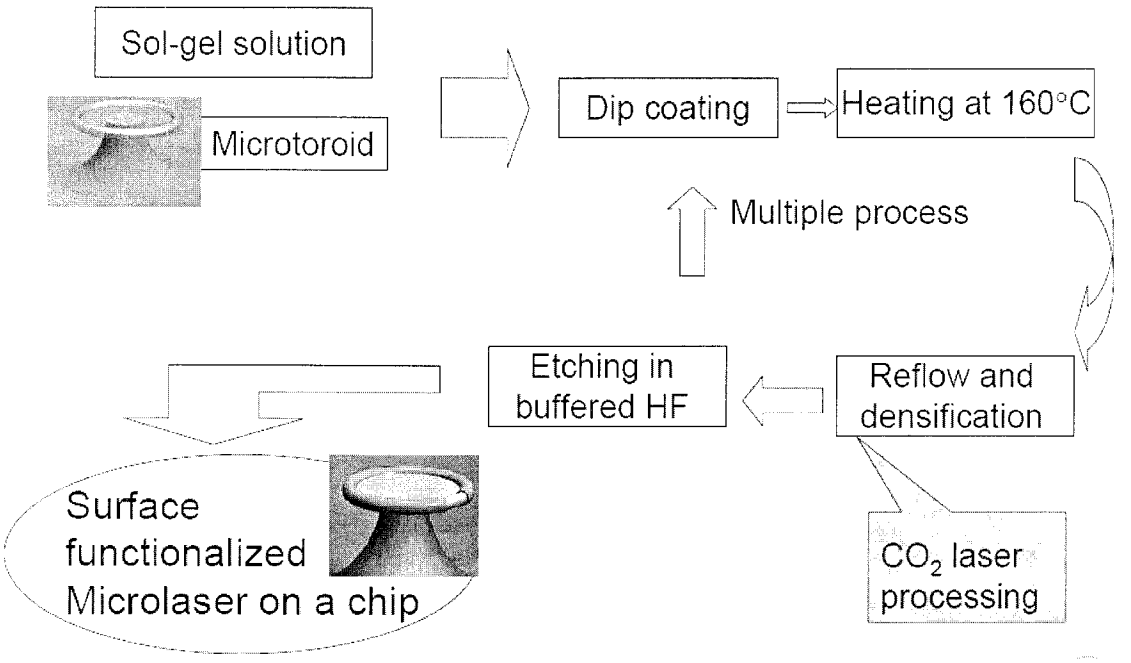

Figure 6.4. Schematic of surface functionalization of a microtoroid on a silicon chip

6.3 Surface functionalization of microtoroid cavities on a Si chip

Figure 6.4 shows a schematic for surface functionalization of a silica microtoroid cavity on a Si wafer. Silica toroid-shaped microresonators supported by a circular silicon pillar were fabricated upon a silicon wafer containing a 2 μm layer of thermal silica (SiO_2) [51]. The sol-gel starting solution was prepared as described in chapter 5. After aging the sol-gel solution at room temperature for 10 hours, we immersed silica microtoroids in the solution for 3-5 hours. Then the wafers were heated in an oven at 160°C for another 10 hours to drive off surface water. Microtoroids were then irradiated with a CO_2 laser (10.6 μm emission) in order to reflow and densify the sol-gel films. The CO_2-laser emission is

selectively absorbed by the silica layers. This and the relatively high thermal conductivity of silicon (~100 times more thermally conductive than silica [52, 53],) leads to selective reflow and densification of sol-gel at the all-important toroid periphery. Sol-gel deposited elsewhere was unaffected by this process step. Because of the large difference between the etching rate of densified and undensified silica films in buffered HF, sol-gel deposited on all regions of the wafer other than the densified perimeter of the toroid could subsequently be selectively removed. Microtoroids ranging in diameter from 60 to 85 μm were fabricated and the Er^{3+} concentration in the sol-gel layer was estimated to be around $10^{19}\,cm^{-3}$.

6.4 Fiber taper coupled microtoroid lasers on a Si chip

An important feature of gain functionalization of the surface is that it puts optical gain only where it is needed, i.e., where best overlap is possible with the fundamental whispering-gallery modes. Figure 6.5 illustrates both a sol-gel functionalized microtoroid and the taper coupling configuration used to both provide optical pumping and to extract laser optical power. Figure 6.6 is a photomicrograph showing a taper-coupled microtoroid laser. The pump wave was provided by a tunable, single-frequency, external-cavity laser operating in the 980 nm band and having a short-term linewidth less than 300 kHz. The sample chip was held in a rotator that was mounted upon a 3-axis translator for position control. Two CCD cameras were used to monitor the microtoroid samples and the taper, providing both

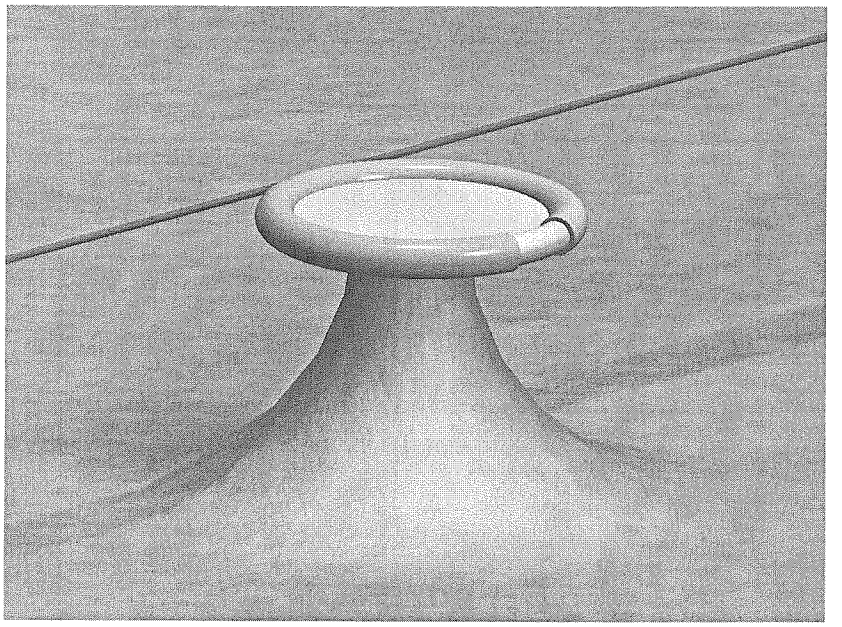

Figure 6.5. Illustration showing a micro-chip laser consisting of an Erbium-doped sol-gel thin film applied to a microtoroid. Also shown is a fiber taper used for both pump coupling and laser emission extraction.

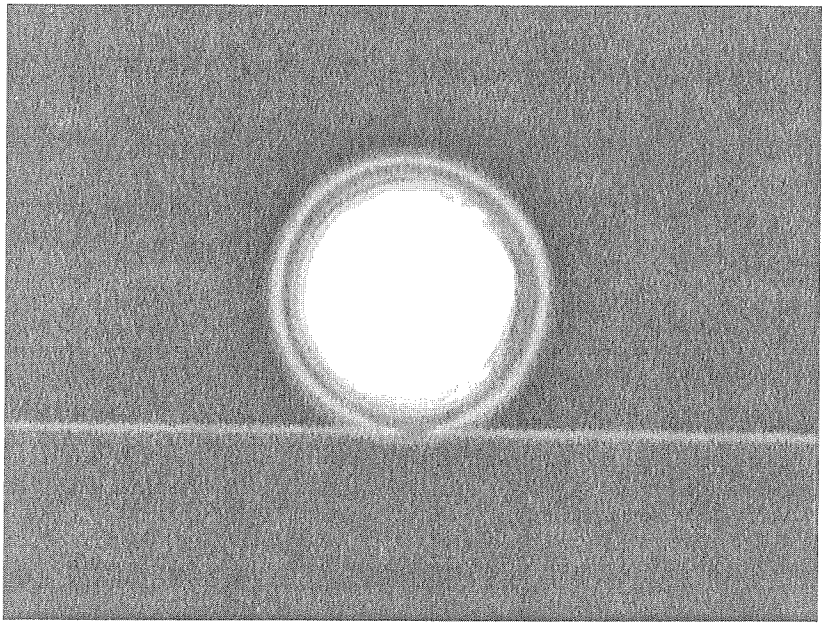

Figure 6.6. Photomicrograph top view of an Erbium microtoroid laser coupled by a fiber taper.

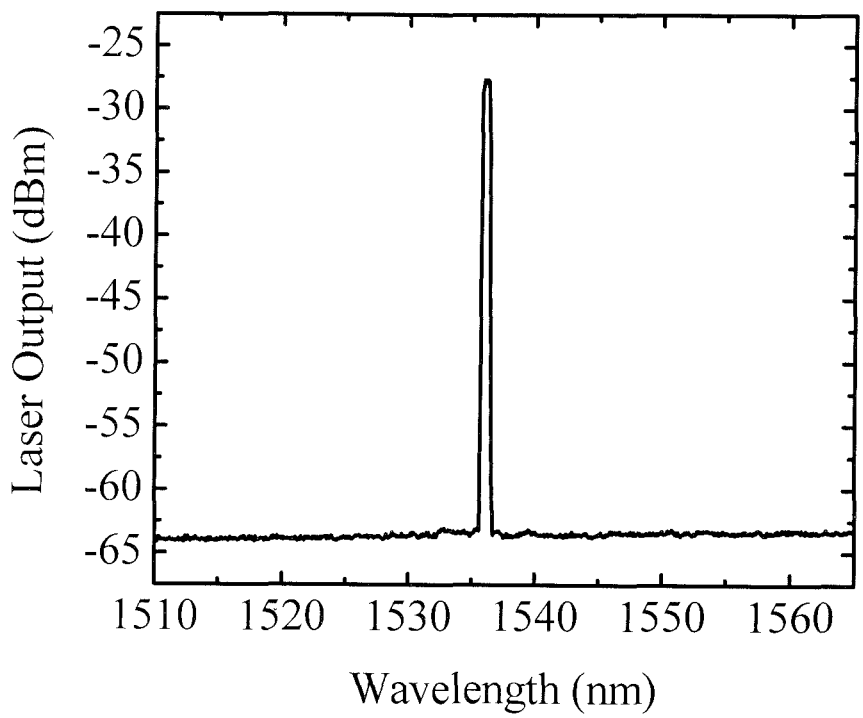

Figure 6.7. Emission spectrum of a microtoroid laser with approximate diameter of 80 μm.

horizontal and vertical views. The angle of the microtoroid relative to the taper was adjusted using the rotator to align the taper with the equatorial plane of the toroid.

An optical spectrum analyzer (OSA) with resolution of 0.5 nm was used to measure the laser emission. A typical laser spectrum is presented in fig. 6.7. Single line emission (within the resolution of the OSA) was most often observed, however, at increased pumping levels it was sometimes possible to induce oscillation in other longitudinal modes.

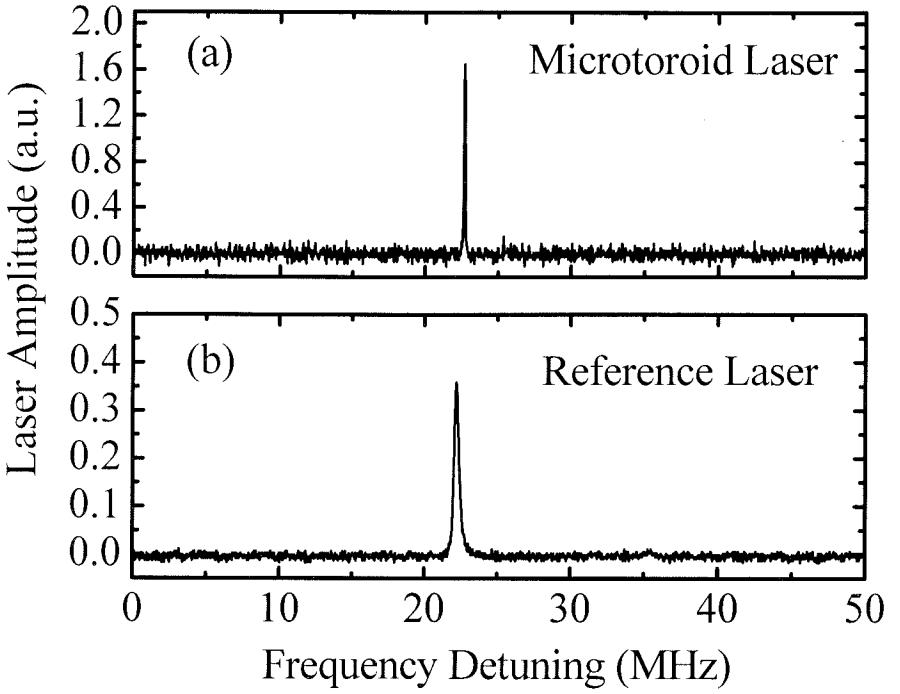

Figure 6.8. (a) Laser emission spectrum from Er-doped sol-gel thin-film coated microtoroid laser. (b) Reference laser emission spectrum from a 1550 nm single-mode laser with short-term linewidth of 300 kHz. Both spectra were measured using a high finesse scanning Fabry-Perot spectrometer.

To further resolve the single line observed in the OSA scan of fig. 6.7, a high finesse (~5000) Fabry-Perot etalon having a resolution of a few megahertz was also used to analyze the laser spectrum. A single-frequency, tunable, external-cavity laser emitting in the 1500 nm band and with known short-term linewidth of 300 kHz was measured as a reference. Both spectra are presented in fig 6.8.

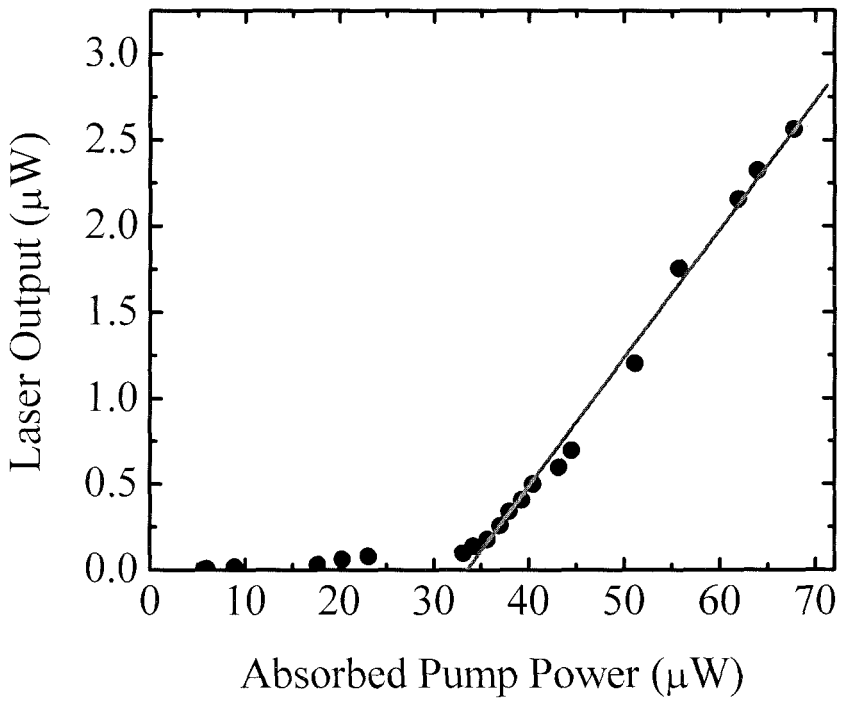

Figure 6.9. Measured laser output power plotted versus absorbed pump power for a microtoroid laser with a diameter of 80 μm.

The measured laser output power plotted versus the absorbed pump power is shown in figure 6.9. The threshold pump power in this data is 34 μW by extrapolation of the linear lasing region. The differential quantum efficiency was measured to be as high as 11% for the single-mode, unidirectional operation. During measurements, the microtoroids were in contact with the taper. While this creates a very stable coupling, it prevents optimization of the pump and emission coupling efficiencies. As a result, it might be possible to further

reduce the threshold in more optimally coupled structures. The effect of optimization of coupling will be part of a future study employing an improved experimental setup.

6.5 Conclusions

In summary, we have demonstrated Erbium-doped microtoroid lasers on a chip by use of a sol-gel surface-functionalization technique. Single-line laser emission and threshold pump powers as low as 34 μW were observed. Future work will be directed towards studies of optimal coupling and potential integration with other devices.

Chapter 7

FABRICATION AND CHARACTERIZATION OF MICROTOROID LASERS ON A SI CHIP

7.1 Introduction

Optical gain can be generated by a nonlinear optical process, Stimulated Raman Scattering (SRS), or rare-earth ions as a gain medium. These effects are the basis for a variety of devices, such as Raman amplifiers/lasers and rare-earth ions-doped amplifiers/lasers [11, 54-56]. In Raman laser, the gain appears at frequency shifted from the pump wave by an amount corresponding to the frequency of materials molecular vibration. While in rare-earth doped lasers, the operating wavelength are determined by the energy level of dopants, instead of the host materials itself. Many different rare-earth ions, such as erbium, neodymium, thulium, etc, can be used to realize amplifiers operating at different wavelength covering from visible to infrared light.

Recently, a chip-based silica resonator structure in the form of a microtoroid has demonstrated ultra-high-Q-factors in the range of 100 million [51]. By coating these high-Q microcavities with erbium-doped solgel films or by beginning with erbium implanted silica layers, low threshold rare-earth-doped microlasers on a chip have been demonstrated [57, 58]. In another study, the realization of integrated Raman microlasers beginning with a layer of thermally-grown silica has been achieved [59]. The fabrication of both low threshold Raman microlasers and Rare-earth doped microlasers made from silica-on-silicon

is especially interesting because they are integrable with other optical or electronic components and make integrated photonics circuits possible [57-59]. A number of methods have been used to fabricate SiO_2 films on silicon substrate, such as flame hydrolysis deposition and chemical vapor deposition [60, 61]. An alternative route to fabricate silica films is the sol-gel technique. Compared with other methods, the sol-gel method has several advantages: First, it is a versatile technique that involves wet chemical synthesis, therefore the chemical composition of the materials can be stoichiometrically controlled at the molecular level, and the distributions of dopants are homogeneous. Second, it is cost effective due to reaction at low temperature without expensive and delicate vacuum system. This technique allows a wide variety of thin films to be deposited on various substrates. Different optical devices, such as erbium doped waveguide amplifiers (EDWA), one-dimensional photonics crystal devices, microlenses, external-cavity distributed Bragg reflector and size-tunable silica nanocubes have been fabrication by sol-gel or mediated sol-gel methods [62-64]. However, even after heat treatment at high temperature, the loss of the sol-gel materials is still not satisfactory for high-quality optical devices. On the other hand, Lasers have been used to treat the surface of ceramics by melting and re-solidification to produce homogeneous and pore-free surfaces. Herein, we will demonstrate a novel CO_2 laser assisted sol-gel method for fabrication of low loss and low threshold microlasers on a Si chip from sol-gel silica thin films. The main advantages of the approach are that it is adaptable to large-scale wafer based fabrication, the materials composition is easily tailored using sol-gel method, and the materials optical loss is decreased dramatically by using laser reflow process. In one series of experiments, Erbium-doped solgel films are used to create low threshold microlasers. In a second set of experiments, pure silica solgel

layers are processed into ultra-high-Q Raman microlasers. Both of these cases demonstrate the ability to use spin coating of solgel films as a processing alternative to deposition or oxidation methods for silica layer formation.

7.2 Fabrication and characterization of microdisk and microtoroid cavities from the sol-gel films

7.2.1 Fabrication of sol-gel films on a silicon wafer

The starting solution was prepared by hydrolyzing tetraethoxysilane (TEOS) using water in acid condition with the molar ration of water to TEOS around 1~2. The silica precursor, tetraethoxysilane(99.95%) and cosolvent, Isopropanol (99%) was purchased from Alfa Aesar. The silica sol-gel catalyst, hydrochloric acid (36%), was a product from J. T. Baker. Deionized water was used during the thin film fabrication process. Er^{3+} ions were introduced by adding $Er(NO)_3$ to achieve the desired Er^{3+} concentration. First 10 g of TEOS water was added to 12 g isopropanol, and 1.4 g of deionized water was added to initiate the hydrolysis and condensation reactions, thereafter 1.2 g of HCl (36%) was added as catalyst to accelerate the reaction. The hydrolysis and polycondensation reactions were allowed to proceed for 3 hours at 70 °C. After the solution aged at room temperature for 24 hours, sol-gel silica thin film was deposited on one side polished silicon (111) substrate by spin-coating method, with spin speed of 3000 rpm for 30 s. During the spin-on process, most of the solvent evaporates rapidly and the sol cross-linked into a network with the form of gel. Subsequently, the Si wafer was annealed at 1000 °C for 3 hours under ambient

atmosphere to remove the residual solvent and residual organic groups inside the sol-gel silica network. Different thicknesses of the solgel films were obtained by changing the viscosity of the solgel solution and spin speed, with multiple coating steps employed to build up the thin film to a desired thickness. The thickness of the solgel film in this work was 1 μm after three cycles of spin-coating.

7.2.2 Fabrication of microdisk microtoroid cavities from the sol-gel films

The silica microlasers on a Si chip was fabricated by the combination of sol-gel method, optical photolithography, XeF_2 etching and finally CO_2 reflowing. Figure 7.1 depicts the fabrication process flow of the microlasers beginning with the solgel layers on the Si wafer. Corresponding optical micrographs, taken after each processing step, are also shown in fig. 7.1. First, thin layer of silica sol-gel films with thickness of 1.2 um were deposited on a silicon (111) substrate. Then series of silica circular pad were created on the silicon wafer through a combination of photolithography technique and buffered HF etching. Subsequently, these pad served as etch masks for silicon etching using XeF_2 gas, leaving an under-cut silica disks supported by Si pillars. Figure 7.2 shows a transmission spectrum of a fiber taper couple sol-gel silica microdisk. The optical image of the microdisk is presented in the inset of fig. 7.2. Finally, a CO_2 laser is used to selectively reflow the microdisk into the microtoroid. The absorption depth of CO_2 radiation in silica was found to vary from 4 to 34 μm depending on the temperature of the materials [52]. This indicates that complete reflow, instead of surface heating, is possible for silica films around 1 to 2

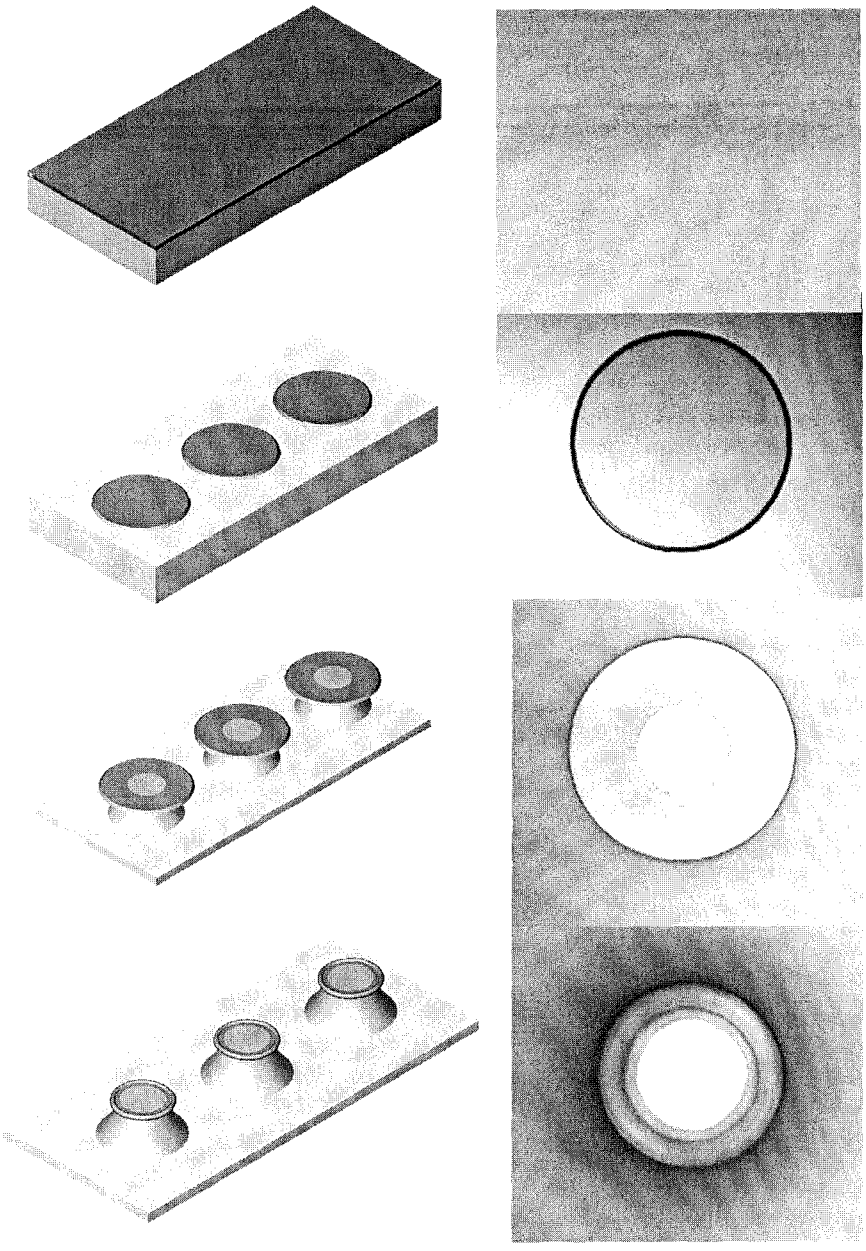

Figure 7.1. Schematic process flow for creation of solgel microcavities on a Si wafer (left) and photomicrograph plan view (right) after each processing step (a) Sol-gel layer spun on a Si wafer; (b) circular pads are etched; (c) XeF_2 isotropic silicon etch; (d) CO_2 laser reflow.

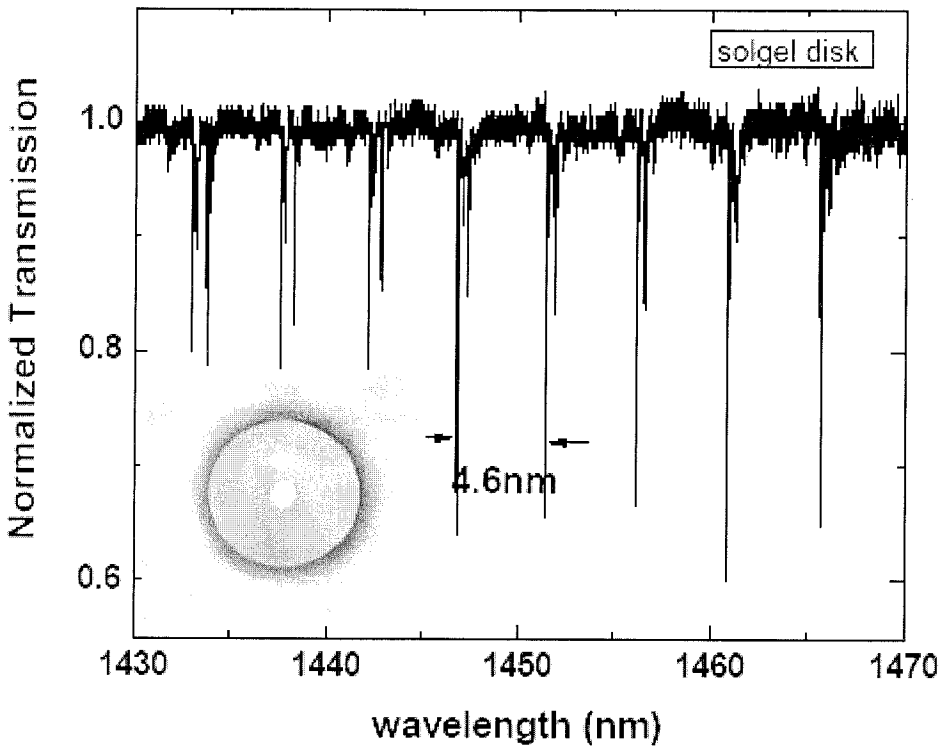

Figure 7.2. Transmission spectrum of a fiber taper coupled microdisk with diameter of 100 micron.

μm. In addition, silica has a strong absorption for CO_2 laser while silicon has much weaker absorption. As a result, during the laser irradiation process, only the periphery of the disk melted, and collapse onto the silicon pillar to form a toroid shaped microcavity due to surface tension. Meanwhile, the inner region of the silica disk which is directly on top of the silicon pillar transfer the heat to silicon pillar, which is 100 times more thermal conductive than silica and helps to dissipate the heat, therefore the inner region is not reflowed. The exceptionally smooth surface of the reflowed toroid cavities endows these structures with their high-Q properties.

7.2.3 Characterization of microdisks and microtoroids with optical microscope and Scanning Electron Microscope (SEM).

Optical microscope:

Figure 7.3 shows Photomicrograph plan view of the circular pads, microdisk, and microtoroid fabricated from sol-gel silica compared with those made from thermal silica. It demonstrates that there is not much difference between the structures prepared in different ways.

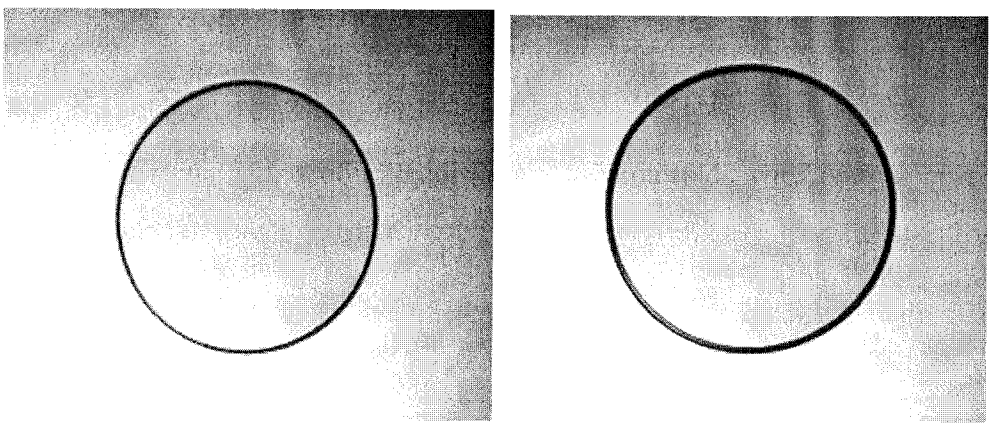

(a)

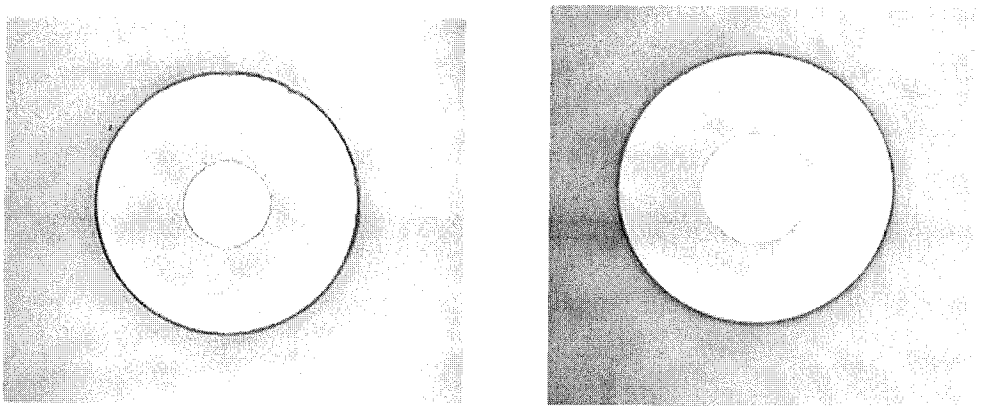

(b)

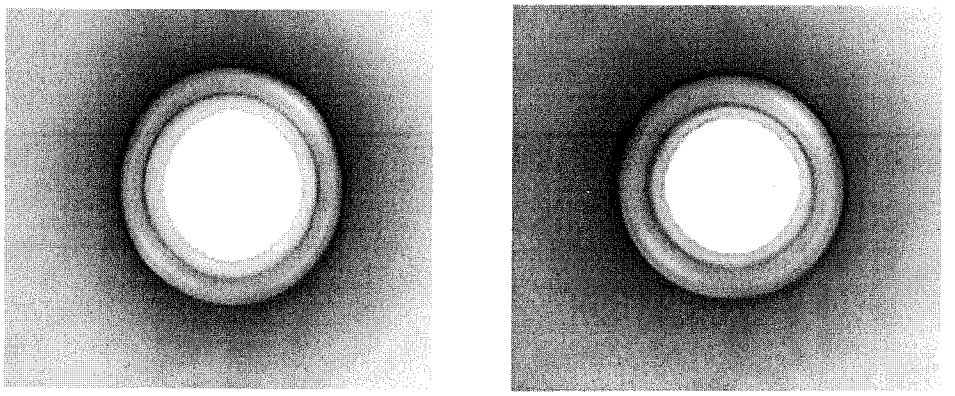

(c)

Figure 7.3. Optical photomicrograph of (a) circular pads on silicon wafer (b) under-etched silica disk (c) Microtoroid after CO_2 laser reflow, from 2 μm thermal silica (left) and 1.2 μm solgel silica (right).

Scanning Electron Microscope (SEM)

The resolving power of optical microscope is limited by the wavelength of imaging light, while SEM uses electron with energies of a few thousand electron volts (eV), which is a thousand times greater than that of the visible light (2 to 3 eV). Therefore, a SEM is used to obtain a finer image of the microdisks and microtoroid. The scanning electron microscopy (SEM) images of the microcavities are shown in Fig. 7.4. Figure 7.4a shows an array of microdisk on the Si chip before CO_2 laser reflow. An enlarged image of the disk in Fig. 7.4b shows the thickness of the disk is about 1.4 microns. A series of microtoid after CO_2 laser reflow was shown in fig. 7.4c. An enlarged image in Fig. 7.4d shows that the toroid has a very smooth surface.

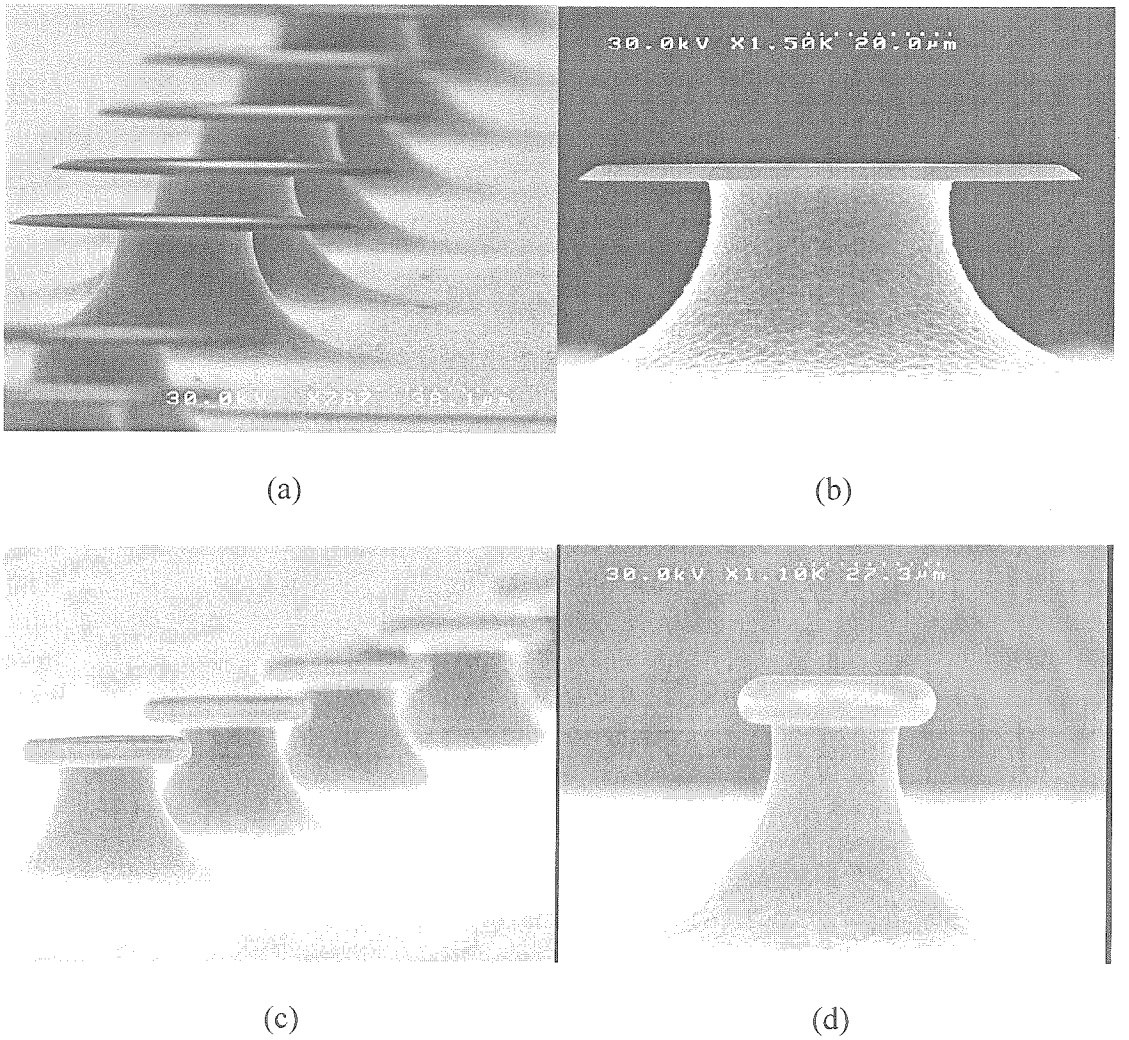

(a) (b)

(c) (d)

Figure 7.4. a)SEM image of an array of microdisks; b) Enlarged SEM image of a microdisk; c)SEM image of an array of microtoids; d)enlarged SEM image of an individual microtoroid.

7.3 Raman Microlasers from sol-gel films on a Si chip

Because silica has a small Raman gain coefficient [65], most silica based Raman sources need high pump power and are macroscale (i.e., table-top devices) [66]. Recently, however,

sub-milliwatt (sub 100 microwatt in thermal silica) threshold Raman micro-lasers on a Si chip have been reported [59]. These devices leverage the very high quality factors and microscale mode volumes possible in the micro-toroid design. To investigate the possibility of Raman oscillation in sol-gel microcavities, microtoroids were fabricated from an undoped sol-gel layer. Specifically, as described above, the CO_2 laser reflow process improves the surface smoothness of the microcavity. Additionally, it is also found to improve sol-gel homogeneity, lowering optical losses substantially [67]. The quality factor of the initial microdisk preform was 7.1×10^4, whereas after the CO_2 laser reflow the microtoroid achieved quality factors as high as 2.5×10^7 at 1561 nm. This corresponds to a waveguide loss of 0.009 dB/cm, which is the lowest loss reported to date for solgel silica-on-silicon technology [68, 69]. These high quality factors allow the observation of Raman emission with threshold pump powers below a milliwatt. In this case, a single-frequency tunable external-cavity laser operating around 1550 nm band was used to pump the microcavity. Figure 7.5 shows a typical Raman laser spectrum taken on a microtoroid with a quality factor of 2.5×10^7 at 1561 nm. In the figure both pump wave at 1561nm and Raman lasing at 1679 nm are visible. The Raman shift corresponds to the frequency of the vibration mode of the silica at 460 cm^{-1}. The inset in figure 7.5 presents a measurement of Raman laser output power as a function of absorbed pump power, and shows a sub-milliwatt threshold at 640 μW.

7.4 Er^{3+}-doped Microlasers from sol-gel films on a Si chip

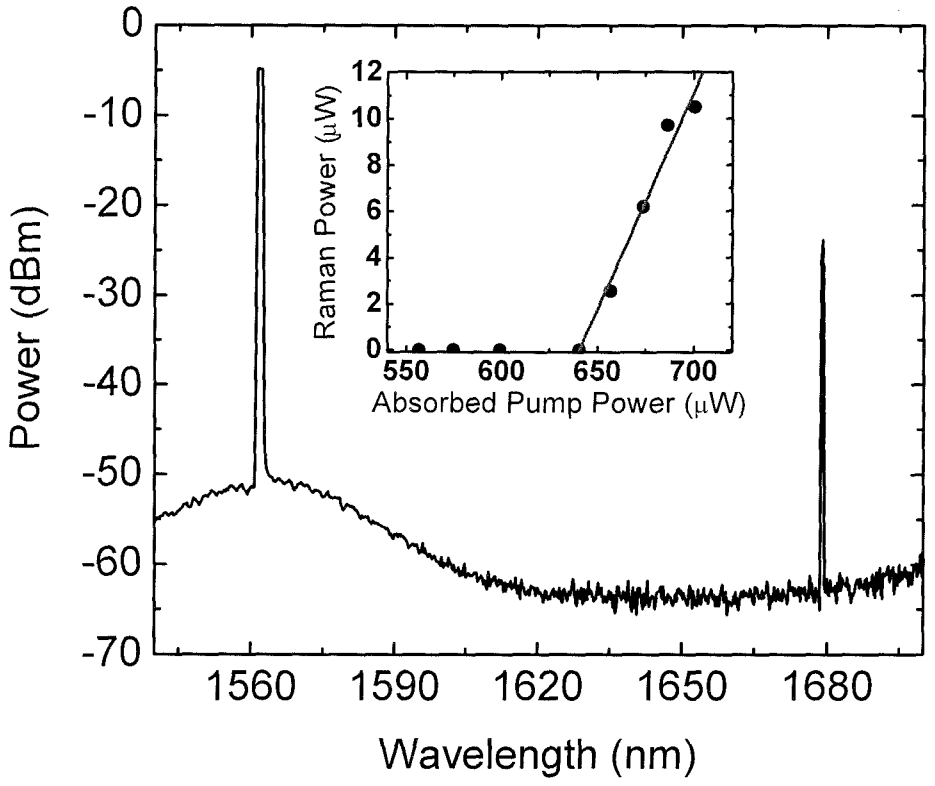

Figure 7.5. Raman emission spectrum of an undoped microtoroid with principal diameter of 49 μm.The pump wavelength is at 1561 nm and Raman oscillation occurs at 1679 nm. The inset shows the measured Raman laser output power versus the absorbed pump power.

From Er-doped sol-gel films, a low threshold Er-doped microlasers was created on a Si chip. The principal diameters of the microtoroids studied in this work ranged from 50 to 60 μm. Tapered optical fibers were used to couple optical power both into and out of the

resonator, with a fiber taper having a waist diameter of 1-2 μm used in order to couple to the resonator with high efficiency. To vary the air gap between the microcavity and the taper, the sample chips were mounted on a three-axis translator for position control. A tunable, single-frequency, narrow linewidth (<300 kHz) external-cavity laser emitting in the 1480 nm band was used to pump the erbium-doped microlaser. The fiber output was connected to a 90/10 fused fiber coupler, with the 10% port connected to an optical spectrum analyzer to monitor both the pump and signal spectra. The 90% port was connected to an oscilloscope to observe the laser dynamics. The pump laser was scanned repeatedly around a single whispering gallery mode. The absorbed pump power was measured as the difference of launched power into the taper and the transmitted power after the taper. Figure 7.6 shows photomicrograph of a fiber taper coupled microlaser. The green ring around the toroid periphery is due to upconverted photoluminescence from Er^{3+}. Figure 7.7 show a single line laser spectrum of an Er-doped microtoroid laser made from Er-doped sol-gel films. The resolution of the optical spectrum analyzer is 0.5 nm. The pump wavelength is at 1442 nm and the lasing wavelength is at 1553 nm. Single-mode operation could be obtained by proper choice of the coupling condition. The laser output as a function of absorbed pump power is shown in the inset of figure 7.7. Benefit from both the high quality and small mode volume of the cavity, a threshold pump power of 3 μw was achieved. A further optimization of the coupling condition can further decrease the threshold to sub-microwatt regime, which will be discussed later.

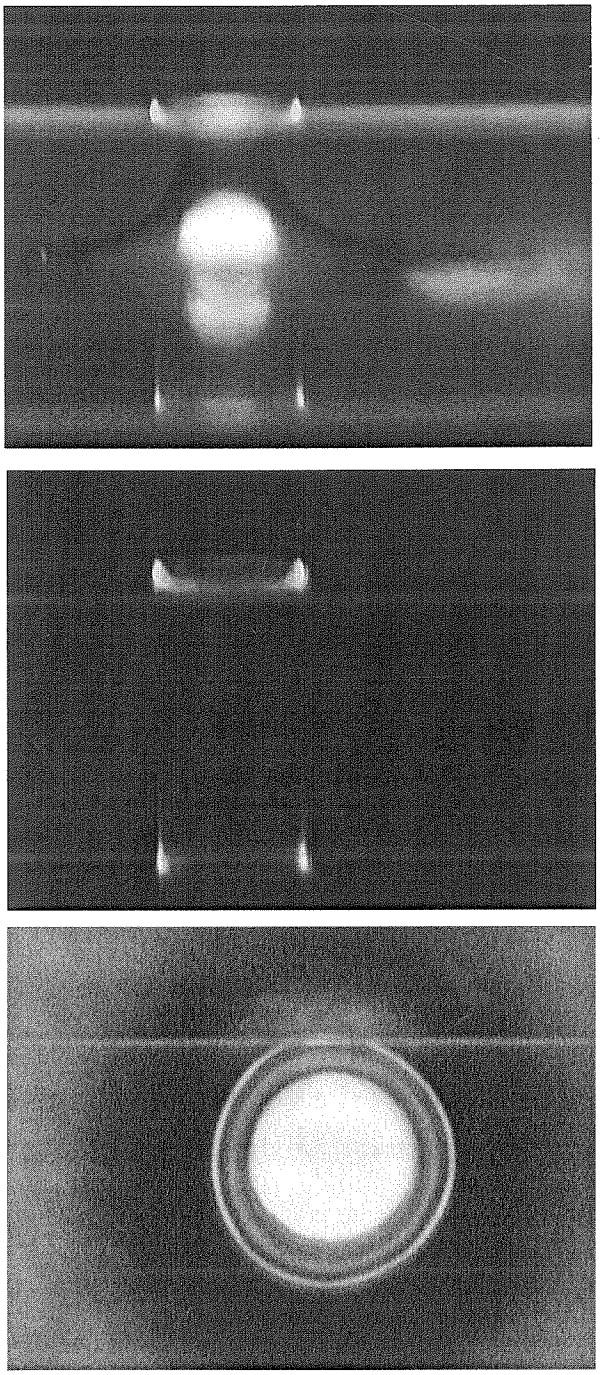

Figure 7.6. Photomicrograph view (horizontal and vertical) of an Er^{3+}-doped solgel silica microtoroid laser with principal diameter of 60 μm coupled by a fiber taper. The green ring is due to upconverted photoluminescence from Er^{3+}.

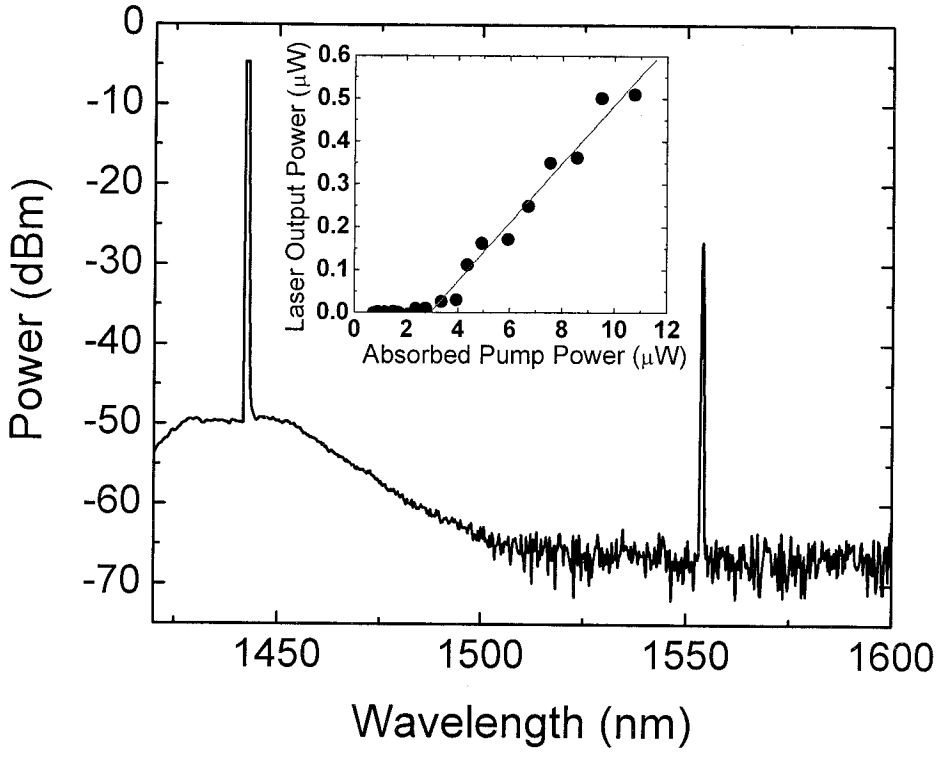

Figure 7.7. Typical laser spectrum of an Er-doped solgel silica microtoroid laser. The pump wavelength is at 1442 nm and the laser line appears at 1553 nm. The inset shows the measured laser output power plotted versus the absorbed pump power.

By varying the erbium concentration in the starting solgel solution, we could adjust the final doping concentration in the microcavities, which ultimately modifies the laser dynamics as previously described for the case of microsphere lasers [16]. In particular, for a heavily doped (Er_2O_3~0.15 mol%) microcavity, pulsation behavior, as opposed to continuous wave (cw) operation, is observed. The pulse repetition rate is 0.9 MHz at laser output power of 3.8 μW and as described in [16] is attributed to the presence of saturable

absorption in the cavity owing to unpumped or incompletely-pumped erbium regions and ion-pair induced quenching. The self-pulsing operation will be discussed in details in chapter 8.

7.5 Analysis of Er^{3+}-doped microlasers

The energy levels of Er^{3+} are composed of well separated multiplet, each of which is made up of a number of broadened individual sub-levels. When 1480 nm is the source as pump power, the pump level and upper laser level belong to the same multiplet. Therefore we can use a two level system model to study the systems interaction with the pump and laser fields. The population density in the upper and lower multiplets are N_2 and N_1, respectively. And the total population density is given by $N_T = N_1 + N_2$.

The equation of motion for the pump and signal field can be written as [54, 70, 71]:

$$\frac{da_s}{dt} = \left(-\frac{1}{2\tau_s^0} - \frac{1}{2\tau_s^{ext}} + g_s^{Er} \right) a_s \tag{7.1}$$

$$\frac{da_p}{dt} = \left(-\frac{1}{2\tau_p^0} - \frac{1}{2\tau_p^{ext}} + l_p^{Er} \right) a_p + i\kappa_p s \tag{7.2}$$

where a_s and a_p are internal signal and pump fields in the cavity; τ_S^0 and τ_P^0 are the decay time due to the intrinsic loss of the cavity for the laser and pump power, respectively; τ_S^{ext} and τ_p^{ext} are the decay time due to coupling to the fiber taper for the laser and pump

power, respectively; κ_p is the field coupling coefficients between the resonator and the waveguide modes at pump wavelength and is equal to $\sqrt{1/\tau_p^{ext}}$; s denotes the input field in the waveguide($|s|^2$ is the input pump power); and g_s^{Er} and l_p^{Er} are the round-trip gain and loss coefficient for the signal and pump wave, respectively. From the propagation equation of pump and signal fields in the cavity [54], we derive the expression for the intracavity gain and loss coefficients, g_s^{Er} and l_p^{Er} :

$$g_S = \frac{c}{2n_s}\left[\left(\sigma_s^e + \sigma_s^a\right)N_2 - \sigma_s^a N_T\right] \tag{7.3}$$

$$l_p = \frac{c}{2n_s}\left[\left(\sigma_s^e + \sigma_s^a\right)N_2 - \sigma_s^a N_T\right] \tag{7.4}$$

where c is the speed of the light, n_s and n_p are the refractive indices at the signal and pump wavelength, respectively, $\sigma_{s(p)}^e$ and $\sigma_{s(p)}^a$ are the emission and absorption cross section of erbium ions at signal(pump) wavelength, respectively.

At steady state, the time derivatives of the pump and laser field in the cavity are zero, which lead to

$$N_2 = \frac{\frac{n_s}{c}\left(\frac{1}{\tau_s^0} + \frac{1}{\tau_s^{ext}}\right) + N_T\sigma_s^a}{\left(\sigma_s^e + \sigma_s^a\right)} \tag{7.5}$$

$$\frac{a_p}{s} = \frac{i\sqrt{\frac{1}{\tau_p^{ext}}}}{\frac{c}{2n_s}\left[\left(\sigma_s^e + \sigma_s^a\right)N_2 - \sigma_s^a N_T\right] + \frac{1}{2}\left(\frac{1}{\tau_p^0} + \frac{1}{\tau_p^{ext}}\right)} \tag{7.6}$$

7.5.1 Transmission spectrum of the pump

The transmission of the waveguide coupled cavities is [72]:

$$T = \left|1 + i\kappa_p \frac{a_p}{s_p}\right|^2 \tag{7.7}$$

From equation (7.6) and (7.7), the transmission of the pump power of a fiber taper coupled Er^{3+}-doped microcavity can be written as

$$T = \left|1 - \frac{\frac{1}{\tau_p^{ext}}}{\frac{c}{2n_s}\left[\left(\sigma_s^e + \sigma_s^a\right)N_2 - \sigma_s^a N_T\right] + \frac{1}{2}\left(\frac{1}{\tau_p^0} + \frac{1}{\tau_p^{ext}}\right)}\right|^2 \tag{7.8}$$

Figure 7.8 shows the transmission of the pump power of a fiber taper coupled Er^{3+}-doped microtoroids. Similar to that of a un-doped cavities, the coupling of the cavity to the waveguide can be divided into three different regimes, which include over-coupled(0<T<1), critical coupled(T=0), and under-coupled regimes(0<T<1).

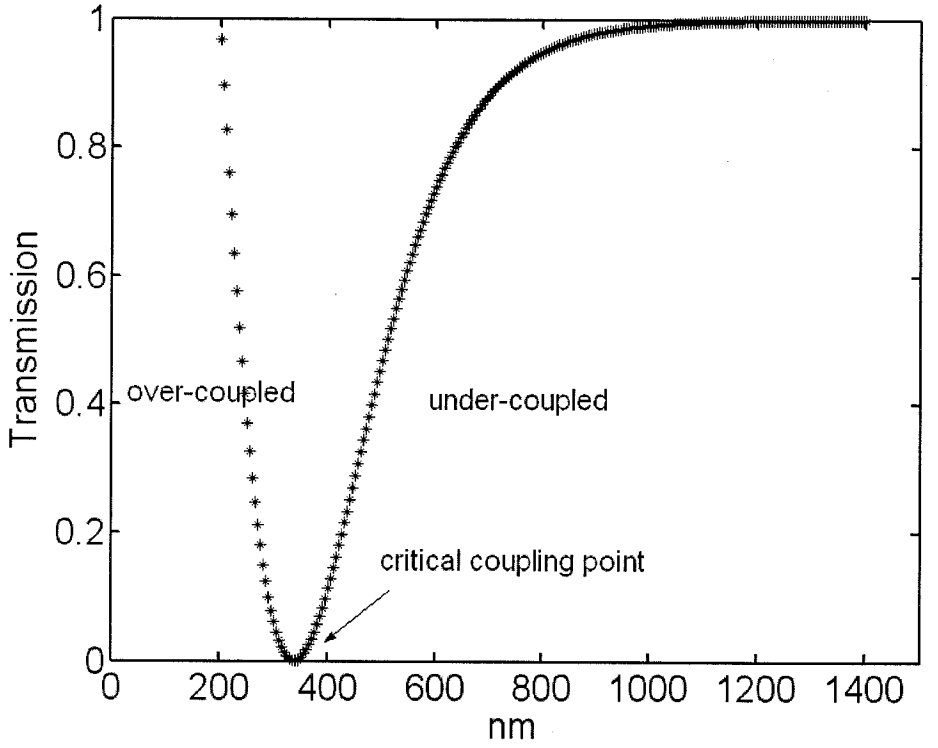

Figure 7.8. Normalized transmission of pump power as a function of air gap between the fiber taper coupler and the microlaser. The diameter of the microlaser is 60 μm. The intrinsic quality factor is 1×10^7.

At zero coupling, no pump power is coupled into the cavity, so this is no laser output power. On the other hand, if we keep increasing the coupling until the cavity is then in the extremely over-coupled regime where no pump power is coupled into the cavity, as a result the laser output power will be zero again. Between those two extreme cases there should exist an optimum coupling condition at which the laser output power is at its maximum. This principal also works for the threshold power and the slope efficiency of the fiber taper coupled cavities

7.5.2 Laser output power of the fiber taper coupled microlasers

The atomic rate equations that describe the population density of levels 1 and 2 in the present of a photon flux of ϕ_s are:

$$\frac{dN_1}{dt} = \frac{N_2}{\tau_{sp}} + (N_2\sigma_e^s - N_1\sigma_a^s)\phi_s + R_{21} \qquad (7.9)$$

$$\frac{dN_2}{dt} = -\frac{N_2}{\tau_{sp}} - (N_2\sigma_e^s - N_1\sigma_a^s)\phi_s + R_{12} \qquad (7.10)$$

where N_1 and N_2 are the population density of level 1 and 2, respectively, R_{21} and R_{12} are the pumping rates into these level, and τsp is the spontaneous lifetime of Er in level 2. Because the lifetime of Er in level 3(~10μ) is much shorter that that in level 2(~10ms), we can assume most of the Erbium stay in level 1 and 2, so $N_1+N_2=N_T$, where N_T is the total population density.

In a steady state situation, we have $\frac{dN_1}{dt} = \frac{dN_2}{dt} = 0$, so we can solve (7.9) to obtain

$$N_2 = \frac{N_T\sigma_a^s\phi_s + R}{\frac{1}{\tau_{sp}} + (\sigma_e^s + \sigma_a^s)\phi_s} \qquad (7.11)$$

where $R=R_{12}=-R_{21}$. The linear gain coefficient g is:

$$g = N_2\sigma_e^s - N_1\sigma_a^s = \frac{N_T\sigma_a^s\phi_s + R}{\frac{1}{\tau_{sp}(\sigma_e^s + \sigma_a^s)} + \phi_s} - N_T\sigma_a^s \tag{7.12}$$

At steady state, the round trip gain is equal to the round trip loss:

$$e^{gl_0}(1-L) = 1 \tag{7.13}$$

where l_0 is the round trip distance and L is the faction of round trip loss. In the case of very small loss(L<<1), so $e^{-gl_0} \cong 1 - gl_0$ and equation (7.13) can be written as

$$gl_0 = L. \tag{7.14}$$

So at steady state when the pump power exceed the threshold power, the actual gain g felt by the laser oscillation is clamped at the threshold value g_t.

In equation (7.14), replace g with equation (7.12) and the laser photon flux is

$$\phi_s = \frac{1}{L}\left(Rl_0 - \frac{N_T\sigma_a^s l_0}{\tau_{sp}(\sigma_e^s + \sigma_a^s)}\right) - \frac{1}{\tau_{sp}(\sigma_e^s + \sigma_a^s)} \tag{7.15}$$

where the pumping rate is

$$R = \left(N_1\sigma_a^p - N_2\sigma_e^p\right)\phi_p = \left(N_T\sigma_a^p - N_2\left(\sigma_a^p + \sigma_e^p\right)\right)\phi_p \tag{7.16}$$

and the round trip loss L is

$$L = \frac{n_s l_0}{c}\left(\frac{1}{\tau_s^0} + \frac{1}{\tau_s^{ext}}\right) \tag{7.17}$$

with ϕ_p denotes the photon flux at the pump wavelength and the population density N_2 at steady state is given by equation (7.5) . The laser power in the cavity is

$$P_S = Ah\nu_s\phi_s = \frac{V_0 h\nu_s}{L}\left(R - \frac{N_T\sigma_a^s}{\tau_{sp}(\sigma_e^s + \sigma_a^s)}\right) - \frac{Ah\nu_s}{\tau_{sp}(\sigma_e^s + \sigma_a^s)} \tag{7.18}$$

where A is the cross section area of the laser mode, h is the Plank constant, and v_s is the optical frequency of the laser mode. Figure 7.9 shows the laser output power as a function of the loading condition, i.e. the air gap between the fiber taper coupler and the microlaser, for different intrinsic quality factor. When the intrinsic quality factor of the microlaser is 5×10^6, the maximum laser output power point is in the under-coupled regime and the power drops to zero before the critical coupling point for the pump power. As the intrinsic quality factor increases to 1×10^7, the maximum laser output power point is still in the under-coupled regime, but at the critical coupling point there is still some laser output. If the intrinsic Q increases further, the maximum laser output power point almost overlap with the critical coupling point. It shows that with the increasing intrinsic quality factor Q_0, the maximum laser output point approaches the critical coupling point gradually.

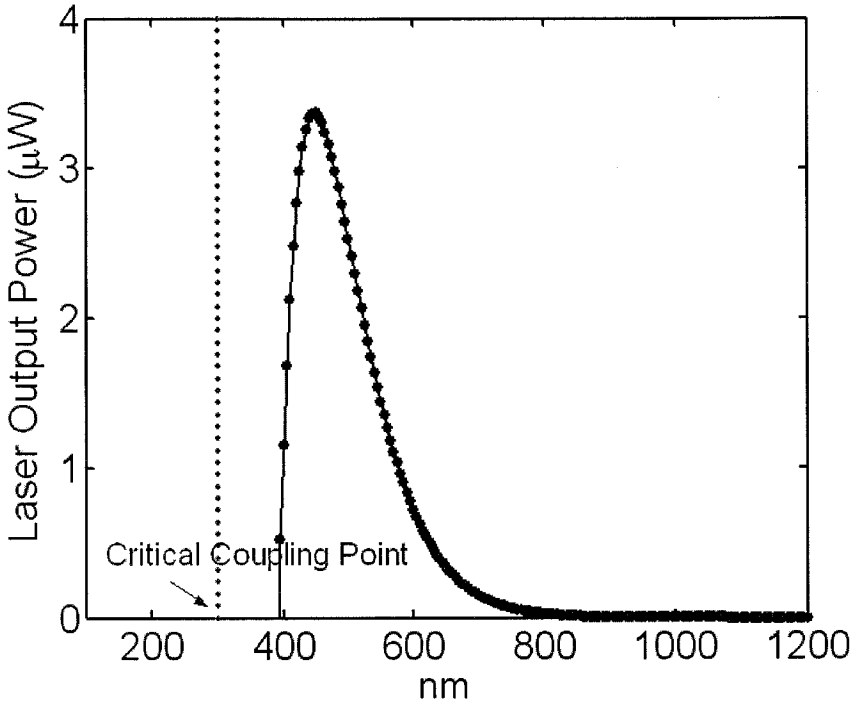
Laser Output Power (μW)
4
3
2
1
0
Critical Coupling Point
200
400
600
800
1000
1200
nm

(a)

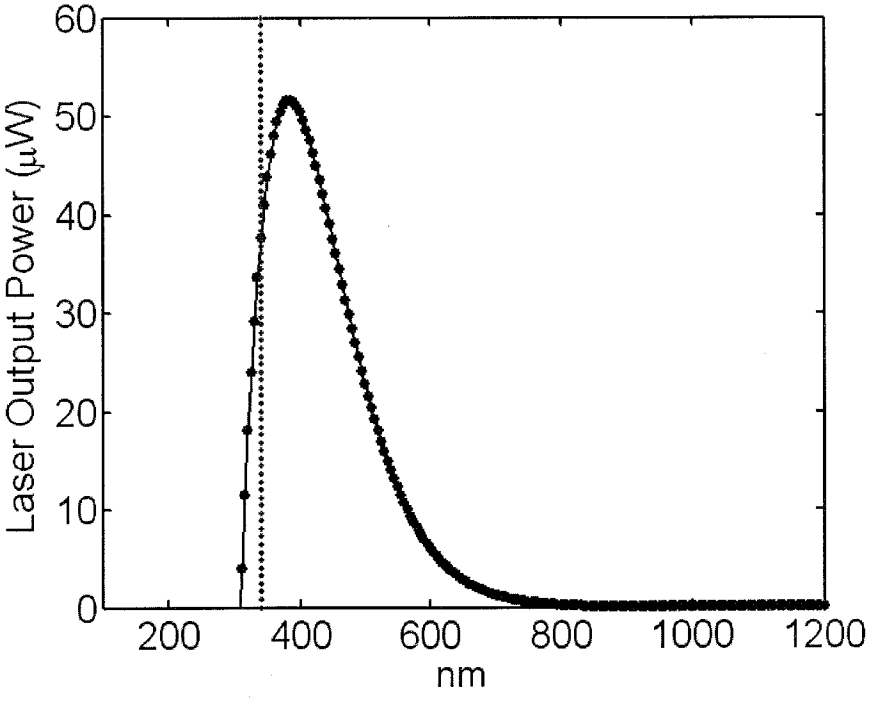
Laser Output Power (μW)
60
50
40
30
20
10
0
200
400
600
800
1000
1200
nm

(b)

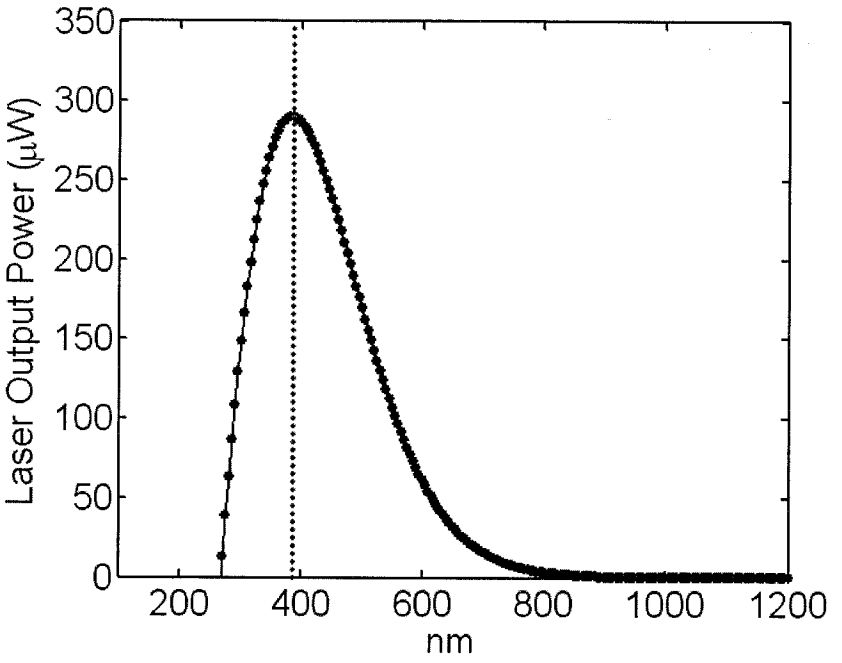

(c)

Figure 7.9. Laser output power as a function of air gap between the fiber taper coupler and the microlasers with different intrinsic Q of (a) 5×10^6 (b) 1×10^7; and (c) 5×10^7. The red dashed line marks the critical coupling point of the pump power.

7.5.3 Threshold power of the microlasers

When pump is at its threshold value, the laser output power is zero. From equation (7.15), the threshold pumping rate is obtained by setting the laser photon flux equal to zero

$$R_{th} = \frac{N_T \sigma_a^s}{\tau_{sp}\left(\sigma_e^s + \sigma_a^s\right)} - \frac{L}{\tau_{sp}\left(\sigma_e^s + \sigma_a^s\right)\gamma_0} \tag{7.19}$$

According the equation (7.16), the pump field in the cavity is

$$\left|a_p\right|_{th}^2 = \frac{\phi_p^{th}}{c} h\nu_p V_p = \frac{R_{th}}{c\left(N_T\sigma_a^p - N_2\left(\sigma_a^p + \sigma_e^p\right)\right)} h\nu_p V \tag{7.20}$$

The input pump power in the fiber can be calculated from equation (7.6)

$$\left|s\right|_{th}^2 = \tau_p^{ext}\left[\frac{c}{2n_s}\left[\left(\sigma_s^e + \sigma_s^a\right)N_2 - \sigma_s^a N_T\right] + \frac{1}{2}\left(\frac{1}{\tau_p^0} + \frac{1}{\tau_p^{ext}}\right)\right]^2 \left|a_P\right|_{th}^2 \tag{7.21}$$

And the absorbed pump power can be calculated from equation (7.8) for transmission of the pump power

$$P_{th}^{abs} = (1-T)\left|s\right|_{th}^2 \tag{7.22}$$

Figure 7.10 shows the input and absorbed threshold pump power in the fiber as a function of the air gap between the fiber taper coupler and the cavity. The critical coupling point of the pump is marked by a red dotted line. In the under-coupled regime, when the fiber taper approaches the cavity gradually, i.e. the air gap decreases gradually, the threshold pump power in the fiber decrease gradually because for a given power in the fiber more pump power can be coupled into the cavity. Before the critical coupling point, the threshold pump power in the fiber reaches its minimum value and begins increase when the air gap keeps decreasing. At the critical coupling point, the threshold pump power in the fiber is already much larger than its minimum value. The reason can be that before reaching the critical coupling point, although more input pump power can be coupled into

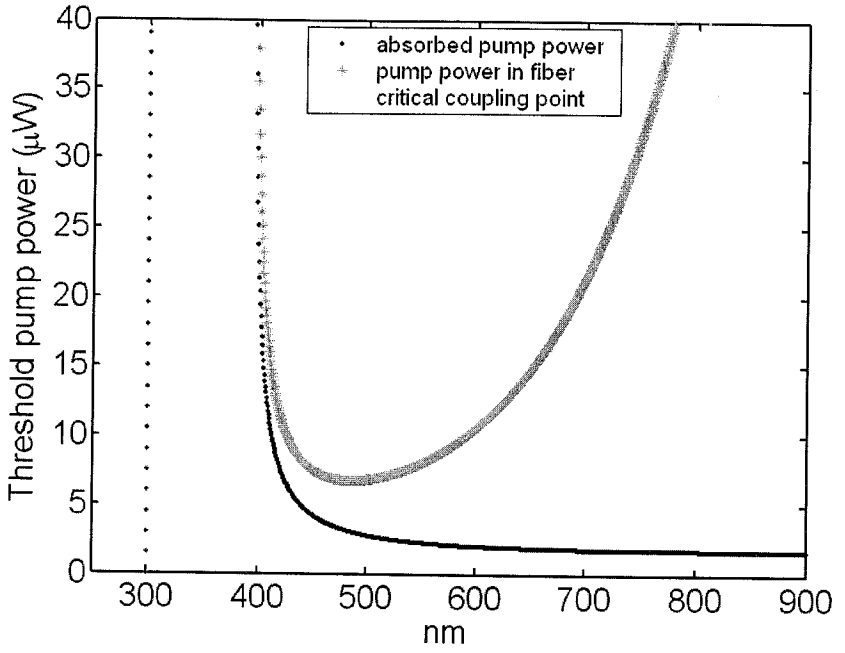
absorbed pump power
pump power in fiber
critical coupling point
Threshold pump power (μW)
nm
0
5
10
15
20
25
30
35
40
300
400
500
600
700
800
900

(a)

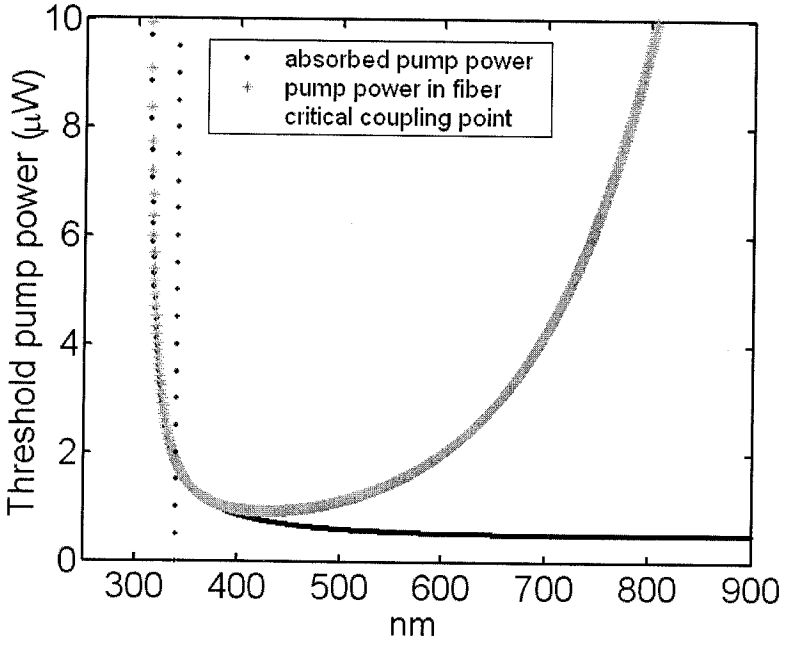
absorbed pump power
pump power in fiber
critical coupling point
Threshold pump power (μW)
nm
0
2
4
6
8
10
300
400
500
600
700
800
900

(b)

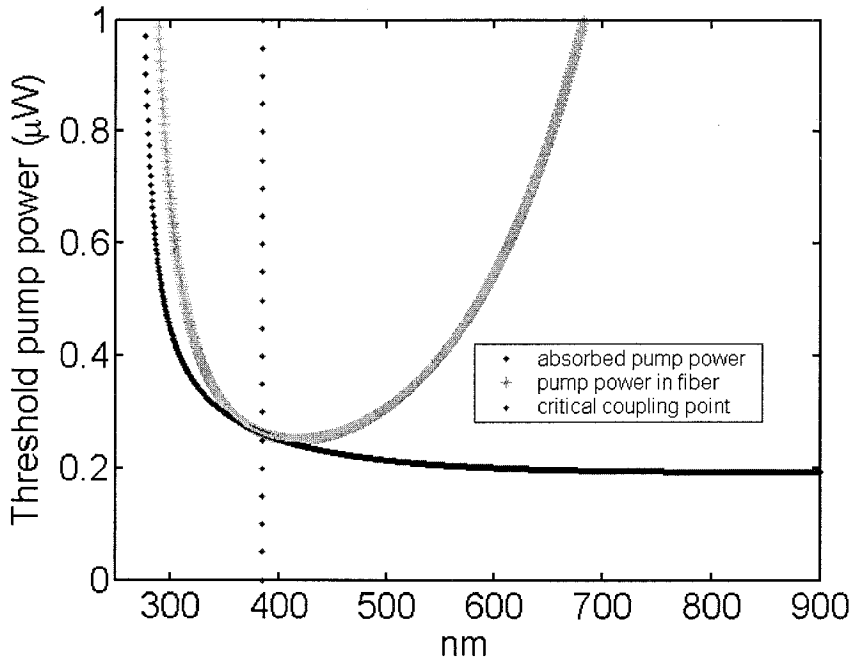

(c)

Figure 7.10. Threshold pump power as a function of air gap between the fiber taper coupler and the microlasers with different intrinsic Q of (a)5×10^6; (b) 1×10^7 ; and (c) 5×10^7. The dashed red line marks the critical coupling point of the pump power.

the cavity when the air gap is smaller, but also more laser power can be coupled out of the cavity which means that the coupling loss for the lasing mode increases, therefore after certain point in the under-coupled region, the effect of increasing coupled pump power can not compensate that of the increasing coupling loss of the lasing mode on the threshold; as a result the threshold increase again. On the other hand, the absorbed threshold keeps increasing when the air gap between the fiber taper and the cavity decreases. For the lasing mode the coupling loss increases monotonically with the decreasing air gap, so the

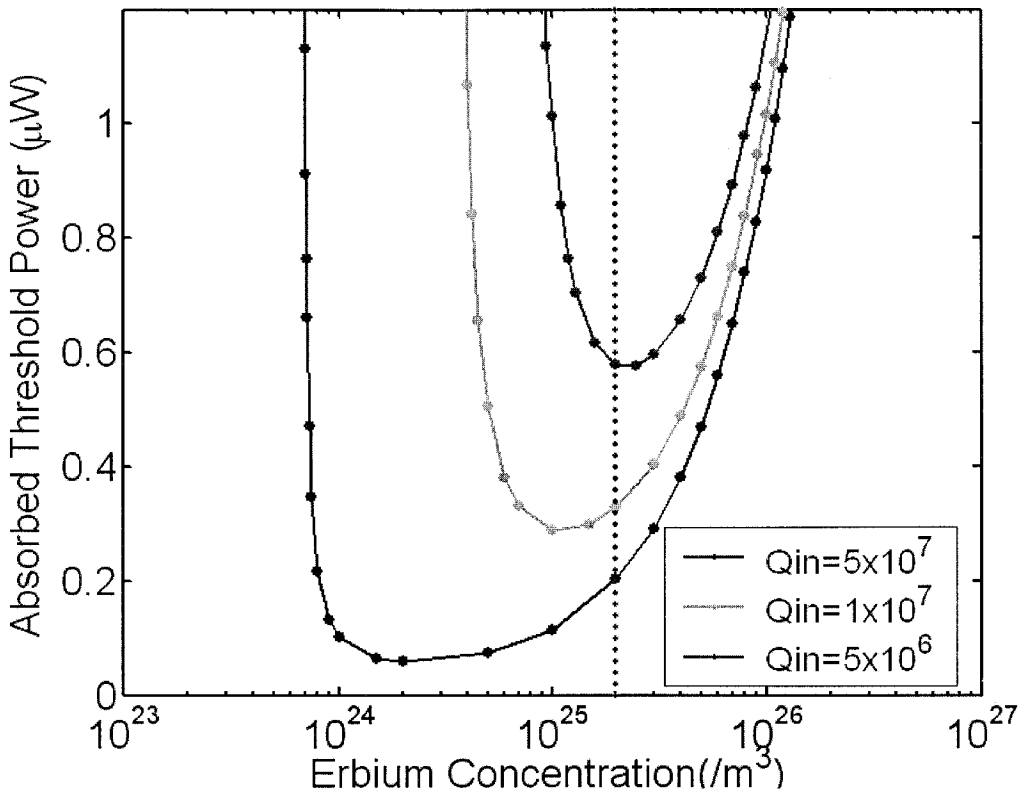

Figure 7.11. Threshold pump power as a function of erbium concentration in the microlasers with different intrinsic Q of (a) 5×10^6; (b) 1×10^7; and (c) 5×10^7. The red dotted line marks the concentration of $2\times10^{19}cm^{-3}$.

minimum absorbed pump power, i.e. threshold, needed to get the laser output increases gradually.

Equations (7.19), (7.20) and (7.21) show that the threshold power also changes with the Er^{3+} concentration in the cavity. Figure 7.11 illustrates the minimum absorbed threshold power as a function the Er^{3+} concentration. It shows that the threshold power is minimized at a certain erbium ion concentration. This optimal erbium ion concentration depends, in

turn, on the intrinsic quality factor of the pump mode. In the low concentration limit, the threshold power increases sharply because Er^{3+} ions are not able to give sufficient gain required for loss compensation; while in high concentration limit, the threshold again increases due to increases of concentration-dependent loss mechanism, such as up-conversion and ion-pairs-induced quenching.

7.5.4 Differential Quantum Efficiency of the microlasers

The differential quantum efficiency of the laser is defined as

$$\eta = \frac{P_{laser}}{P_{pump} - P_{th}} \cdot \frac{v_{pump}}{v_{laser}} \tag{7.23}$$

In sections (7.5.2) and (7.5.3), the laser output power and the input pump threshold have been obtained as the functions of the air gap between the fiber taper and the cavity. Plug those expressions in equation (7.23) and the differential quantum efficiency of the laser as a function of the air gap is presented in figure 7.12. Similar to the case for the laser output power, there is an optimum coupling point where the differential quantum efficiency reaches its maximum value. Compared with the optimum laser output coupling point, the optimum differential quantum efficiency coupling point is at a little more under-coupled point, i.e. larger air gap. It means when the taper fiber approaches the cavity, in general the maximum differential quantum efficiency point will be met first, then the maximum laser output point.

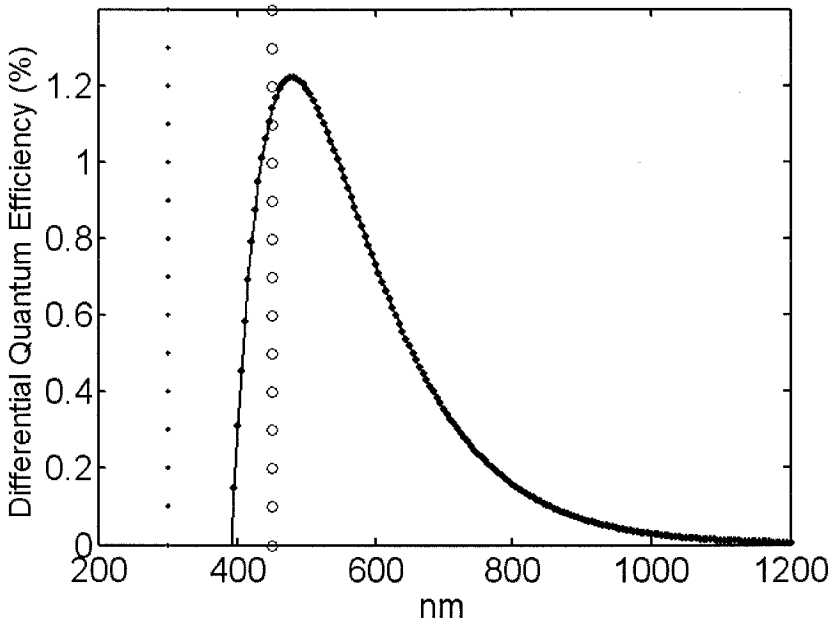
Differential Quantum Efficiency (%)
0
0.2
0.4
0.6
0.8
1
1.2
200
400
600
800
1000
1200
nm

(a)

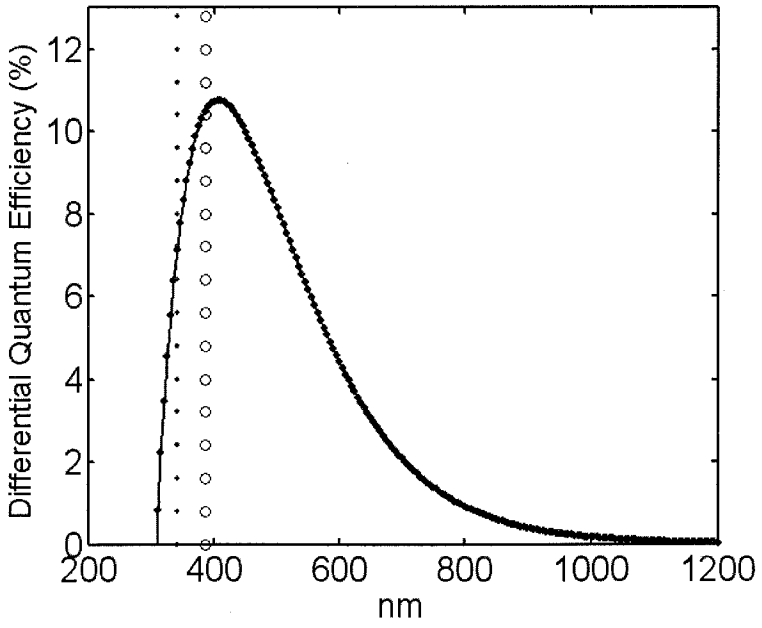
Differential Quantum Efficiency (%)
0
2
4
6
8
10
12
200
400
600
800
1000
1200
nm

(b)

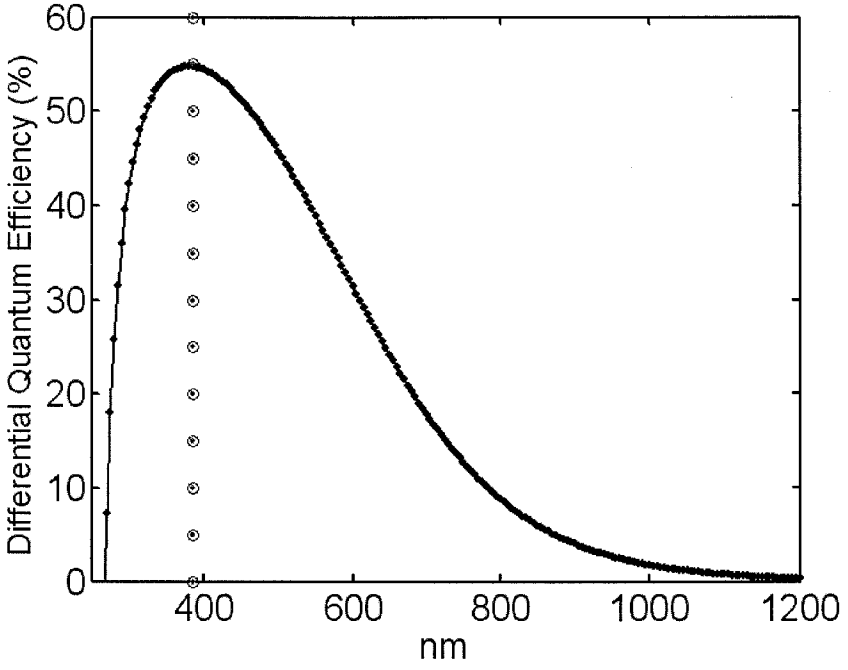

(c)

Figure 7.12. Differential quantum efficiency as a function of air gap between the fiber taper coupler and the microlasers with different intrinsic Q of (a) 5×10^6; (b) 1×10^7; and (c) 5×10^7. The blue and red dotted line marks the maximum laser output point and critical coupling point of the pump mode.

7.5.5 Experimental Results

Er^{3+}-doped microtoroids on a silicon chip were fabricated by the sol-gel method as described in the beginning of this chapter. Different microtoroids were tested and the maximum laser output power always appeared in the under-coupled regime. Figure 7.13 shows the laser output power as a function of the air gap from a microtoroid with diameter of 65 μm and Er^{3+} concentration of 10^{19} cm^{-3}. The differential quantum efficiency versus

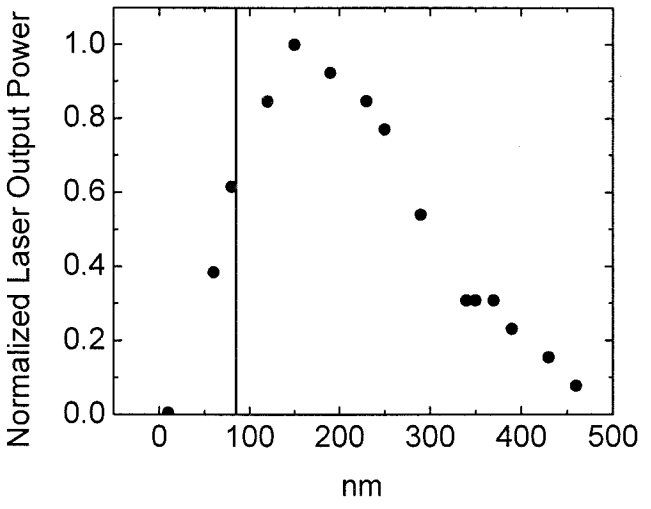

Figure 7.13. Normalized laser output power as a function of air gap between the fiber taper coupler and the microlasers

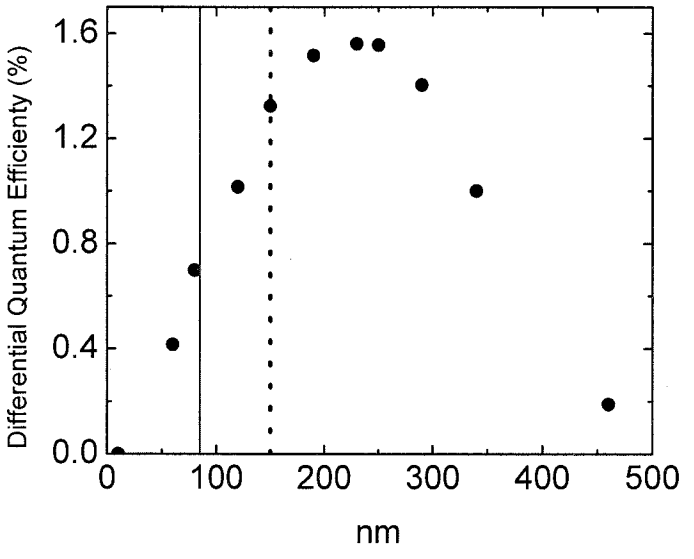

Figure 7.14. Differential quantum efficiency as a function of air gap between the fiber taper coupler and the microlasers

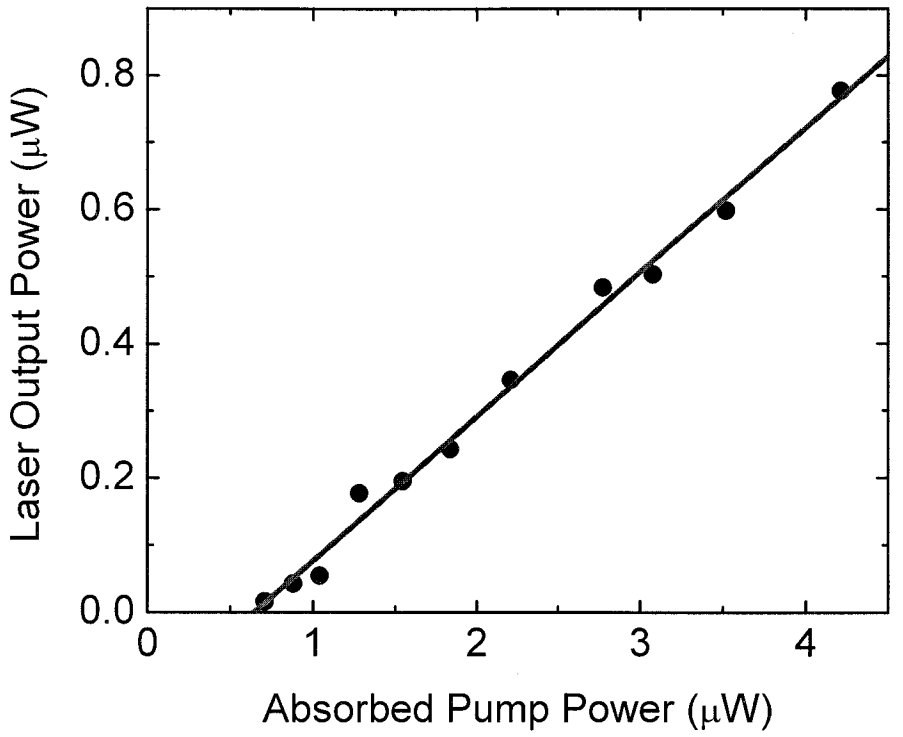

Figure 7.15. Measured laser output power plotted versus the absorbed pump power for a microtoroid laser with principal diameter of 60 μm. The lasing threshold is 660 nW with pump wavelength at 1442 nm and lasing wavelength at 1553 nm.

the air gap is shown in fig. 7.14 with the critical coupling point and maximum laser output power point marked. As the fiber taper get close to the cavity, the pump power coupled into the cavity increases while the coupling loss of the lasing mode also increase, the maximum differential quantum efficiency point is met. When the taper approaches the cavity further,

the differential quantum efficiency begins to decrease while the laser output still increases and reaches its maximum value when it's about 70 nm away from the critical coupling point. The experiment results are consistent with the model derived above. Figure 7.11 shows that a toroid with a principal diameter of 60 μm and intrinsic quality factor (pump mode) between 5×10^6 and 1×10^7, thresholds in the range of 400~600nW can be achieved with an Er^{3+} concentration of 2×10^{19} cm^{-3}. The measured laser output power plotted versus the absorbed pump power from a microtorid with properties as described above is presented in figure 7.15. The threshold was estimated to be as low as 660 nW, which is about three times lower than that of the most recently reported Er-implanted microtoroid resonator [58]. This ultra-low threshold originates from the small mode volume, high quality factor of the microcavity, and homogeneous distribution of the Er^{3+} inside the cavity, which enable the optimized overlap between the active region and the pump modes. Above threshold, the laser output power increases linearly with the absorbed pump power, as expected.

7.6 Conclusion

In conclusion, with the help of both tradition furnace annealing and CO_2 laser-assisted reflow technique, high quality factor microcavities can be fabricated on a Si chip. After the CO_2 laser reflow, a surface roughness within 3 nm can be achieved which enable the very low round trip loss for the microcavities. Without doping inside the silica, a low threshold Raman microlaser can also be achieved. Furthermore, Er-doped silica microlasers can be

successfully fabricated from Er-doped sol-gel films and the small mode volume and very low loss of the modes made record threshold in the sub-μW range possible for the Er^{3+}-doped lasers tested. The analytical model derived for Er^{3+}-doped lasers shows the maximum laser output point is in the under-coupled regime and approaches the critical coupling point of the pump mode as the intrinsic quality factor increases. The maximum differential quantum efficiency point follows the same trend while it is at a more under-coupled point. In addition, the minimum absorbed threshold power for different doping concentration was also investigate to help optimize the doping level to obtain ultra-low threshold microlasers. The results demonstrate the great potential of solgel technology in fabrication of high optical quality materials for integrated optical components on silicon chips.

Chapter 8

PAIRED IONS INDUCED SELF-PUSLING IN ERBIUM-DOPED MICROTOROID LASRES

8.1 Introduction

The dynamics of laser has been an interesting field for investigation since Maiman observed a train of un-damped oscillations in the ruby laser in 1960 [73]. Self-pulsing in laser is interpreted as an intrinsic instability of the laser itself. Different physical origins, such as bidirectional propagation in 'high loss cavity', additional saturable absorber and paired ions, have been observed in some self-pulsing systems [74, 75]. Among them the paired ions induced quenching effect is appropriate for theoretical explanation of self-pulsing operation in heavily Er^{3+}-doped lasers. It has been reported that self-pulsing in erbium-doped fiber lasers is attributed to the existence of ion pairs distributed within the fiber, which is one type of the saturable absorber for the fiber laser system. As the doping concentration increases, the average distance between the ions decrease, which enhance the ion-ion interaction. When both of such ions are in the $^4I_{13/2}$ state, one ion can transfer its energy to the other one, producing one up-converted ion in $^4I_{9/2}$ and one in ground state. Subsequently, the up-converted ion decay rapidly back to $^4I_{13/2}$ state through non-radiatively relaxation. The net effect is loss of one excited ion. For the low paired ion

concentration (x<5%, x is the percentage of paired ions), the quenching effect is negligible and Er^{3+}-doped fiber lasers operate in cw(continuous wave) regime, whereas for high paired ion concentration (x>5%), the lasing is in self-pulsation regime [76].

In this chapter, we develop a model to analysis the self-pulsing operation in Er^{3+}-doped microlasers to understand the mechanism underlying the observed phenomena. In the model, Er^{3+} ions are divided into two groups, single ions and paired ions. Five coupled first-order differential equations are used to describe the dynamical behavior of the system, with two for isolated ions, two for paired ions, and one for the lasing photon. In particular, the pulsation oscillation frequency as a function of the pumping level is studied. The experimental result is presented in the end, which shows consistence with the theoretical prediction.

8.2 Model for ion pairs inducing self-pulsing

As described before, the energy level of Er^{3+} ions are composed of different well-separated levels, each of which is made up of number of individual sub-levels. The isolated ions can be assumed as a three energy level system, which is composed of pumping level, upper laser level and lower laser level. The energy level $^4I_{15/2}$ and $^4I_{13/2}$ are lower laser (ground) and upper laser level, respectively. The pumping level depends on the pump source we use. When the pump wavelength is in the 980 nm band, $^4I_{11/2}$ is the pumping level. For the particular case when 1480 nm laser is used as the pump source, the pumping

level and upper lasing level belong to the same energy level $^4I_{13/2}$ with the pumping level (higher sub-level) closer to the top of the level than the upper lasing level (lower sub-level). Nevertheless, for both cases we can assume that ions in pumping level decay rapidly to the upper laser level through non-radiation relaxation.

Three energy level, $^4I_{15/2}$, $^4I_{13/2}$ and $^4I_{9/2}$, are involved in ion pair interaction [77]. As described in figure 8.1, when both of the neighboring ions are in the $^4I_{13/2}$ energy level, ion 1 transfer its energy to ion 2, causing ion 2 up-converted to energy level $^4I_{9/2}$ with ion 1 itself relax non-radiatively to ground level $^4I_{15/2}$. The up-converted ion 2 quickly decays to the $^4I_{13/2}$ energy level through non-radiative relaxation. The net effect of this process is loss of one excited ion, i.e. decrease of population inversion with no contribution to the laser field. The decay time of the paired Er^{3+} ranges from 1 to 100 μs [78]. We use the atomic state of each ion to describe the state of the paired ions so that the atomic state of the paired ions can be written as (α, β), where α and β are the atomic states of the two neighboring ions, respectively. Four states of paired ions contribute to the paired ions interaction and can be written as $(^4I_{15/2}, ^4I_{15/2})$, $(^4I_{15/2}, ^4I_{13/2})$, $(^4I_{13/2}, ^4I_{13/2})$ and $(^4I_{15/2}, ^4I_{9/2})$. The decay time of Er^{3+} in level $^4I_{9/2}$ relaxes to the lower level much faster than its decay time in level $^4I_{13/2}$. As a result, ion in level $(^4I_{15/2}, ^4I_{9/2})$ relaxes quickly to $(^4I_{13/2}, ^4I_{13/2})$ and we can ignore the population of paired ions in level $(^4I_{15/2}, ^4I_{9/2})$. Similar to what we did for the single ions, we

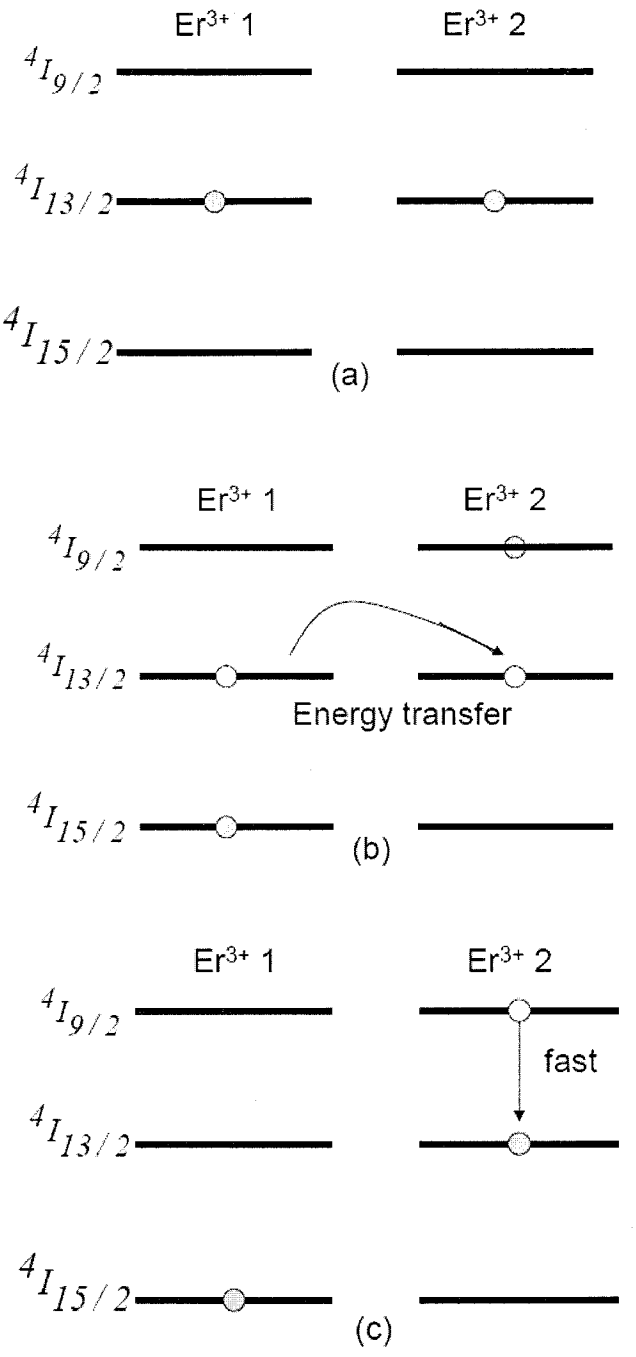

Figure 8.1. Cross-relaxation process between paired ions. (a) two neighboring ions in the $^4I_{13/2}$ level. (b) Energy transfer between two ions. (c)Non-radiative relaxation of ion 1 to $^4I_{15/2}$ level.

describe the paired ions using a three level system as shown in figure 8.2. The $({}^4I_{15/2}, {}^4I_{15/2})$ is called the 0-photon state, where both ions are in the ground state, the $({}^4I_{15/2}, {}^4I_{13/2})$ is called the 1-photon state, where on ion is in the excited state, and the $({}^4I_{13/2}, {}^4I_{13/2})$ is designated as the 2-photon state, where both ions are in the excited state. The decay time of level 2-photon state to 1-photon state ranges from 1 to tens of μs. While for the 1-photon state, one ion is in the ground state and doesn't have cross-relaxation with the other ion, therefore the decay time of 1-photon state to 0-photon state can be assumed to be the same as that of the single ion.

For the single ions, when the ions in ground state are pumped to the pump level, which can be level ${}^4I_{11/2}$ for the 980 nm pump source or a sublevel in ${}^4I_{13/2}$, they relaxes non-radiatively very fast to the meta-stable upper laser level, from where they relaxed to the ground level with emission of one photon through spontaneous emission or stimulated emission. The photons emitted through stimulated emission contribute to the lasing field, while only a small portion of the photons emitted through spontaneous emission can fall into the lasing mode.

According to the analysis of the energy level of the single ions and paired ions above, the rate equations that can be used to describe the dynamical behavior of the Er^{3+}-doped lasers including paired ions are

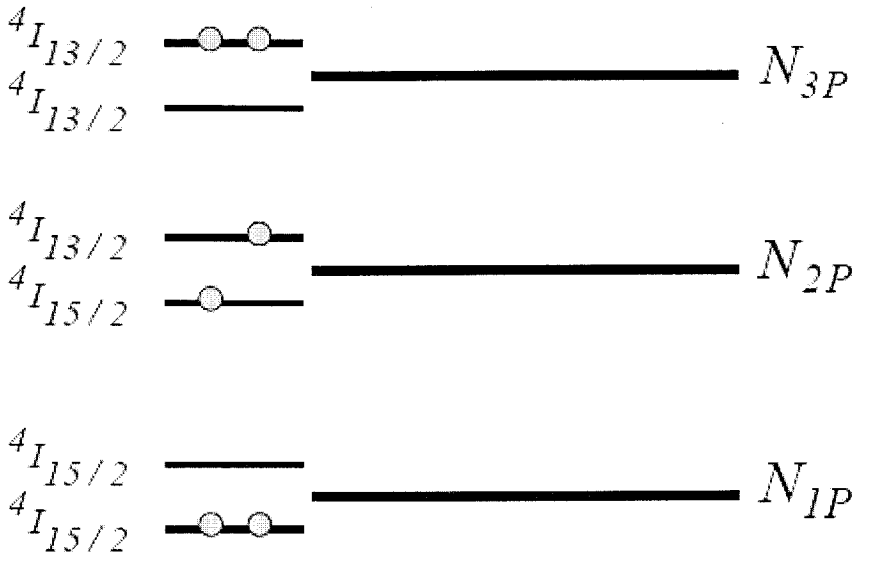

Figure 8.2. Energy level diagram in current model for paired ions

For single ions:

$$\frac{dN_{3S}}{dt} = \left(c\sigma_p^a N_{1s} - c\sigma_p^e N_{3s}\right)P - \frac{N_{3S}}{\tau_{32}}$$

$$\frac{dN_{2S}}{dt} = \frac{N_{3S}}{\tau_{32}} - \frac{N_{2S}}{\tau_{SPS}} - (c\sigma_s^e N_{2S} - c\sigma_s^a N_{1S})S$$

For paired ions:

$$\frac{dN_{3P}}{dt} = -(2c\sigma_p^e P + 2c\sigma_s^e S + \frac{2}{\tau_{SPP}})N_{3P} + (2c\sigma_p^a P + 2c\sigma_s^a S)N_{2P}$$

$$\frac{dN_{2P}}{dt} = (2c\sigma_p^e P + 2c\sigma_s^e S + \frac{2}{\tau_{SPP}}) N_{3P} + (2c\sigma_p^a P + 2c\sigma_s^a S) N_{1P} -$$

$$(2c\sigma_p^a P + 2c\sigma_p^e P + 2c\sigma_s^e S + 2c\sigma_s^a S + \frac{2}{\tau_{SPS}}) N_{2P}$$

For photon density:

$$\frac{dS}{dt} = \gamma \frac{N_{2S}}{\tau_{SPS}} + (c\sigma_s^e N_{2S} - c\sigma_s^a N_{1S}) S - \frac{S}{\tau_{LOSS}} - (2c\sigma_s^a N_{1P} - 2c\sigma_s^e N_{3P}) S$$

The equations above can be used to solve the dynamical behavior of the Er^{3+}-doped lasers. The steady state solution can be obtained by setting the time derivatives of the variables as zero. In these equations, S and P are used to denote the photon density corresponding to the pump and lasing frequency, respectively. The population densities of single ions in the pump level, upper laser level, and lower laser level are labeled N_{1S}, N_{2S}, and N_{3S}, respectively. N_{1P}, N_{2P}, and N_{3P} are the population densities of paired ions in 0-photon state, 1-photon state and 2-photon state. τ_{32} and τ_{SPS} is the lifetime of single ions in pump level and upper laser level, τ_{SPP} is the non-radiative decay time of paired ions from 2-photon state to 1-photon state, and τ_{loss} is the lasing photon decay time in the cavity. σ_p^a and σ_p^e are the absorption and emission cross sections in Er^{3+} for the transition corresponding to the pump frequency, and σ_s^a and σ_s^e are the absorption and emission cross sections in Er^{3+} corresponding to the lasing frequency. c is the speed of light in vacuum. γ is the ratio of spontaneous emission falling into the lasing mode. The

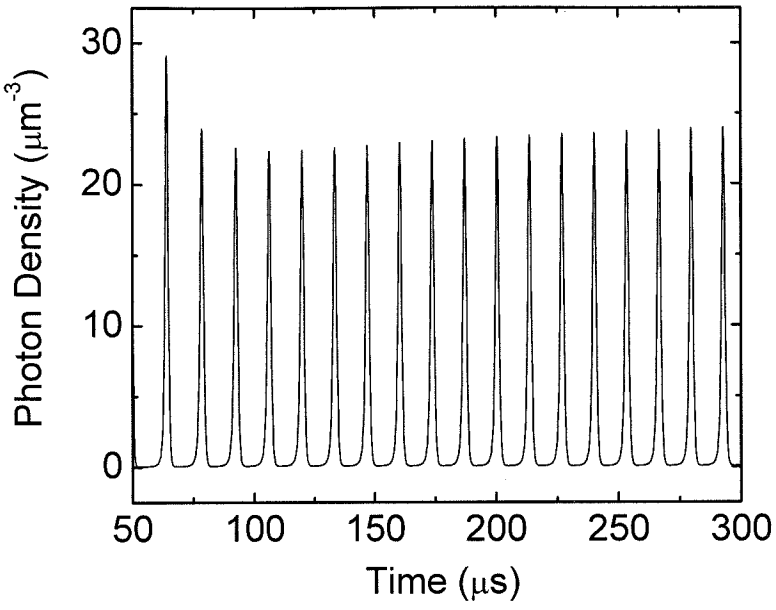
Photon Density (μm-3)
30
20
10
0
50
100
150
200
250
300
Time (μs)

(a)

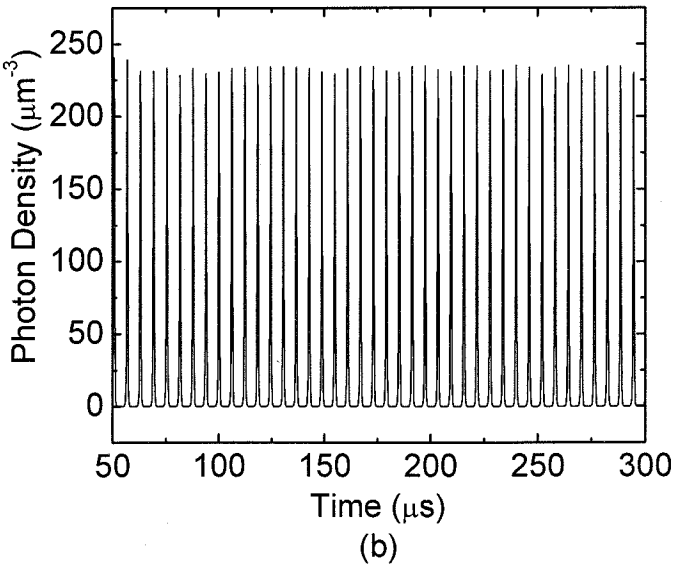
Photon Density (μm-3)
250
200
150
100
50
0
50
100
150
200
250
300
Time (μs)

(b)

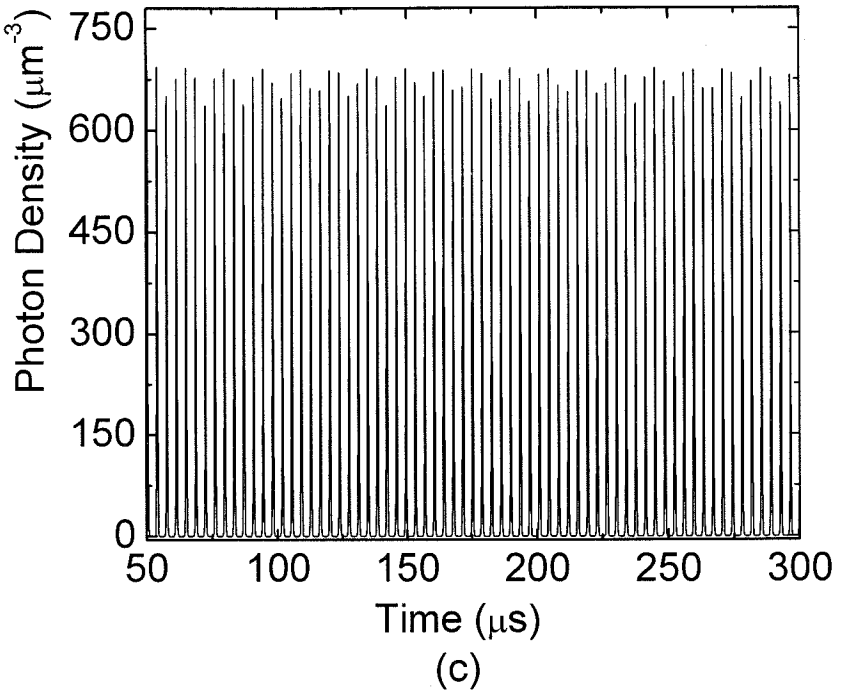

Figure 8.3. Numerical simulation of photon density as a function of time at different pumping level (a) P/Pth=2; (b) P/Pth=8; and (c) P/Pth=20

spontaneous emission factor γ is very small and can be ignored for steady state solution. However, for study of dynamical behavior of the Er^{3+}-doped laser, it's very important to include γ in the system so that the lasing photon density can build up from zero. Dynamical behavior of the Er^{3+}-doped laser is studied with this model. Figure 8.3 gives the numerical simulation of the time evolution of the photon density at different pumping level for the ratio of paired ions being around 10%. The ratio of the pump power to the threshold power is denoted by γ. It shows that self-pulsing oscillation frequency increases with the

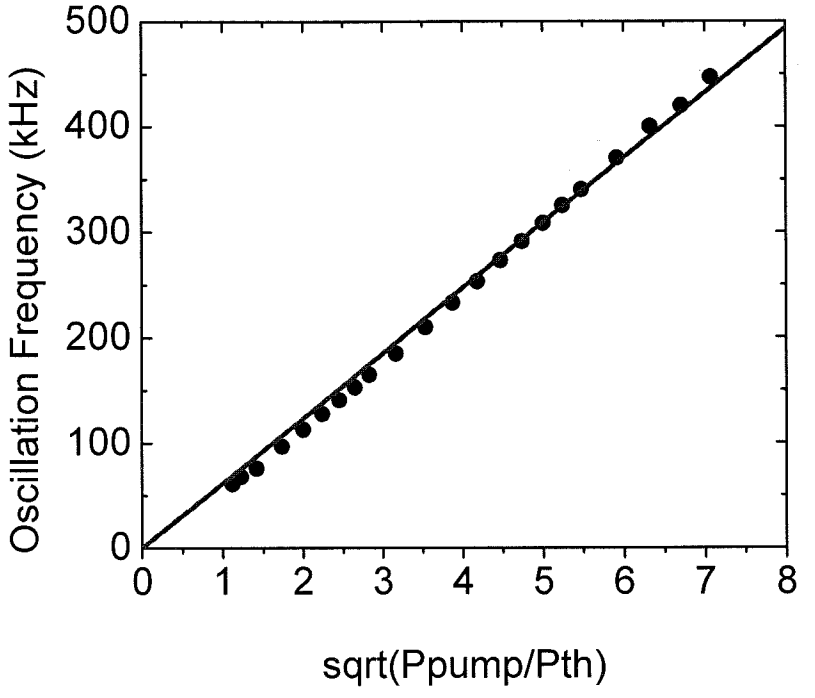

Figure 8.4. Numerical simulation of evolution of the self-pulsing frequency as a function of square root of γ, which is ratio of the pump power with the threshold power

increased pumping level. A linear relation between the oscillation frequency and the square root of γ is presented in Figure 8.4. Table 8.1 list the value of the parameters used for the simulation presented here.

8.3 Experimental results on self-pulsing operation

Table 8.1. Values of parameters used in simulation

Er^{3+} concentration	2.0×10^{19} cm^{-3}
γ: ratio of spontaneous emission captured in laser emssion	1.0×10^{-4}
Absorption cross section of the lasing transition σ_a	6.67×10^{-21} cm^2
Emission cross section of the lasing transition σ_e	7.0×10^{-21} cm^2
Absorption cross section of the pump transition σ_a	6.0×10^{-21} cm^2
Emission cross section of the pump transition σ_a	5.5×10^{-21} cm^2
Upper laser level decay time for single ions τsps	6 ms
Pump level decay time for single ions τ_{32}	10 μs
2-photo state decay time for paired ions τspp	10 μs
Photon decay time in cavity τloss	0.004 μs
Ratio of paired ions K	10%

The influence of the paired ions on the dynamics of the Er^{3+}-doped microtoroid laser has been observed. A tunable single frequency external cavity laser in 1480 nm band is used as the pump source to investigate the dynamical behavior of an Er^{3+}-doped microtoroid laser. Figure 8.5 shows various self-pulsing operation obtained for increasing laser output power, i.e. increasing pumping level. When the laser output is about 1.74 μW, the pulsation frequency is about 578 kHz. When the laser output power increases gradually up to 2.89 μW, a train of pulses with higher frequency of 763 kHz appears. With further increase of the laser output power to 3.71 μW, the self-pulsing frequency reaches 910 kHz. Figure 8.6 shows that the pulsing frequency increases linearly with the square root of the laser output power, which is predicted by the simulation model using paired ions as saturable absorber. As explained before, the lifetime of the paired ions in the 2-photon state is very short, a few

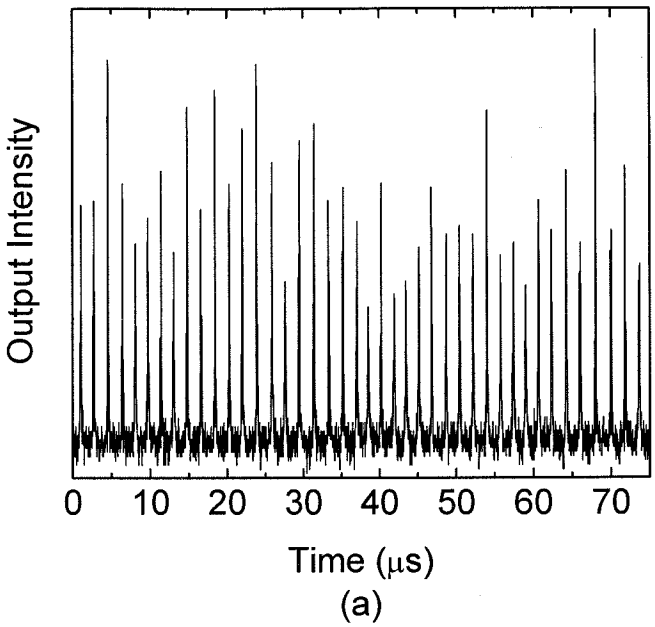
Output Intensity
0
10
20
30
40
50
60
70
Time (μs)

(a)

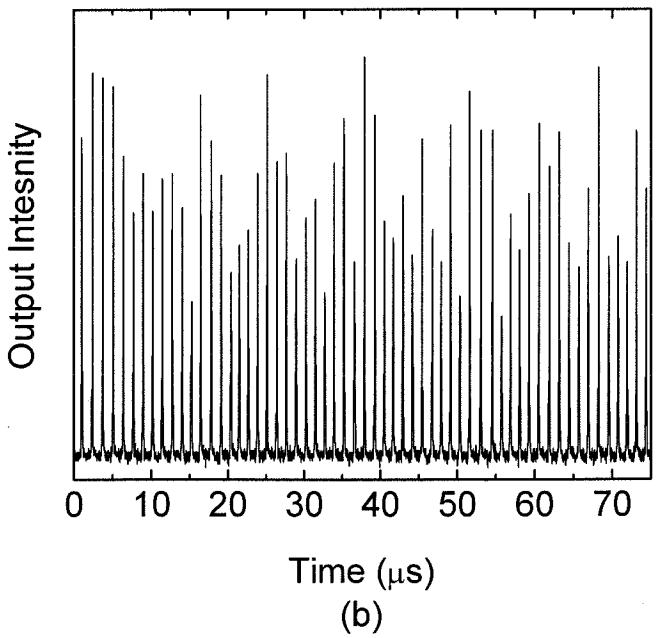
Output Intesnity
0
10
20
30
40
50
60
70
Time (μs)

(b)

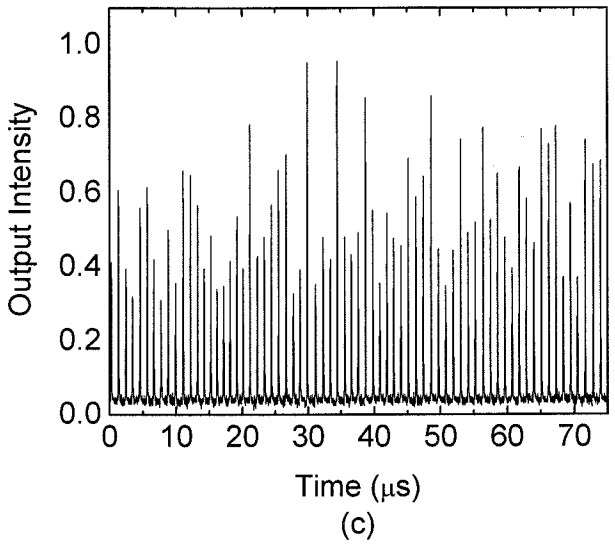

Figure 8.5. Self-pulsing operation of an Er^{3+}-doped microtoroid laser with laser output power of (a) 1.0 μW(b) 1.6 μW and (c)2.1 μW.

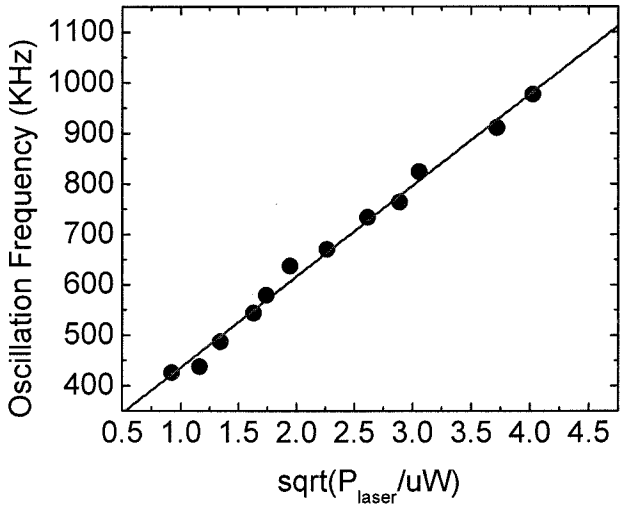

Figure 8.6. Evolution of the self-pulsing frequency as a function of square root of the laser output power. The pump is in 1460 nm band.

μs, so the paired ions may not be sufficiently pumped and act as additional absorber. This saturable absorber make the laser system unstable and thus cause the self-pulsation operation.

8.4 Conclusion

We have shown experimentally and theoretically that self-pulsation operation is possible due to the quenching effect caused by the cross-relaxation between two neighboring excited ions. The time evolution of the laser intensity changes with the pumping level. Furthermore, both the theoretical model and experiments shows that the pulsation frequency increases linearly with the pump power or laser output power. Therefore by varying the doping concentration of erbium in the solgel layers, the laser dynamics can be controlled.

Chapter 9

CONCLUSION AND FUTURE WORK

The research in this thesis presents preparation and characterization of Er^{3+}-doped microsphere lasers and microtoroid lasers on a silicon chip by the sol-gel method. Different schemes are used to gain functionalize different microcavities. For the non-planar structure, microsphere, Er^{3+}-doped sol-gel silica films were deposited outside the microspheres to create gain medium in the microcavities. The same method was also used to surface functionalize the microtoroid cavities on a silicon chip, while in this case due to the unique properties of the microtoroird, only the periphery of the toroids were selectively coated with the sol-gel films. In another method, sol-gel silica is not used just a layer of film outside a given base resonators. Instead, the sol-gel films were deposited on a single silicon chip and toroidal shaped microcavities were fabricated from the sol-gel films directly. It is demonstrated in this work that low threshold Raman microlasers and can be fabricated from un-doped sol-gel silica films and very low threshold Er^{3+}-doped microlasers on a silicon chip can be created from Er^{3+}-doped sol-gel silica films. A continuous lasing with a threshold of 660 nW for Er^{3+}-doped microlaser was also obtained. Furthermore, by varying the Er^{3+} concentration of the starting sol-gel materials, the laser dynamics of the microlasers changes accordingly.

Analytic formulas were derived to predict the laser performance, such as the laser output power, the threshold power, and the differential quantum efficiency, under different loading condition, i.e. the air gap between the fiber taper coupler and the cavities. In addition, the minimum absorbed threshold power for different doping concentration was also investigate to help optimize the doping level to obtain ultra-low threshold microlaser. The experimental results together with the theoretical analysis give us a better understanding of the laser performance.

By increasing the Er^{3+} concentration in the microcavities, self-pulsing in the microlasers was observed. It is well known that self-pulsing can be achieved with adequate saturable absorber in the laser system. We presented a theoretical model in which we included paired ions as the saturable absorber. It shows that self-pulsing operation can be expected with paired ions induced quenching in the system. The pulsation oscillation frequency increases linearly with the square root of the pumping level, which is consistent with the experimental observation.

The sol-gel method provides a versatile way to fabricate different materials system for various photonics application. It's worthy to exploit their advantages to the maximum in application where they can provide properties not attainable by other methods. There is still a great deal of further work remains to be done.

- Co-doping system in sol-gel materials

As described earlier, more than one dopants can be incorporated in the silica glass by using the sol-gel method. Several co-doping systems can be studied and used to prepare microlasers with better performance:

- **Yb^{3+}/ Er^{3+}codoping system**

By adding Yb^{3+} and Er^{3+} together into the silica matrix, the pump efficiency of the laser can be increased because the Yb^{3+} has a larger absorption cross section than Er^{3+} and can transfer the energy non-irradiatively to the Er^{3+} to help excite the Er^{3+} to the upper laser level.

- **Al^{3+}/ Er^{3+}codoping system**

Since silica network is built on covalence bond, a certain number of non-bridging oxygen groups must be present to allow for incorporation of Er^{3+}. In pure silica glasses, a rigid structure exists and therefore the amount of non-bridging $Si\text{-}O^-$ is very small. So the solubility of Er^{3+} in the silica network is very low. When the concentration is above certain 'threshold concentration', Er^{3+} tends to aggregate together and form cluster in the silica matrix, which leads to some detrimental effects such as paired ions induced quenching and cooperative up-conversion, etc. When aluminum ions are incorporated into the silica network, they attract the Er^{3+} ions and at the same time increase the number of non-bridging oxygen groups in the silica network. The solubility of Er^{3+} in the silica network is therefore greatly increased.

- Enhanced nonlinear optics sol-gel materials

As mentioned in this thesis work, a low threshold Raman microtoroid laser on a silicon chip can be fabricated from pure silica sol-gel films. On the other hand, silica has a very small Raman gain coefficient. By doping phosphate into the silica network, the Raman gain coefficient can be increase and therefore can further enhance the nonlinear effects in the cavities.

- Low-melting point sol-gel materials

Some applications may involve incorporation of functional organic or biological molecules in the silica network. Densification and reflow at high temperature is avoided in those cases. By using SiO_2/ZrO_2 materials system, the reflow temperature of the sol-gel materials can be decreased as low as 190 °C [79]. This low reflow temperature materials enable incorporation of components which can not sustain high temperature process, such as semiconductor quantum dots, functional organic components or biological components. More application on these materials can be investigated in the future.

- Sol-gel and organic hybrid materials

The introduction of organic components into the silica network permits further tailoring of the chemical and physical properties of the silica glass, such as improved mechanics properties, lower densification temperature, decreased shrinkage during drying and densification etc. For example, by adding photo-sensitive organic components, which can polymerize under exposure to UV light, into the silica network, different degree of exposure to UV light can induce different change of the refractive index in polymerized

and non-polymerized region. A grating structure can be created in the sol-gel silica to fabricate new optical devices.

Bibliography

1. Braginsky V. B., Gorodetsky M. L., and Ilchenko V. S., *Quality-Factor And Nonlinear Properties Of Optical Whispering-Gallery Modes.* Physics Letters A, 1989. **137**(7-8): p. 393-397.
2. Mabuchi H. and Kimble H. J., *Atom Galleries For Whispering Atoms - Binding Atoms In Stable Orbits Around An Optical-Resonator.* Optics Letters, 1994. **19**(10): p. 749-751.
3. Sandoghdar V., Treussart F., Hare J., LefevreSeguin V., Raimond J. M., and Haroche S., *Very low threshold whispering-gallery-mode microsphere laser.* Physical Review A, 1996. **54**(3): p. R1777-R1780.
4. Vollmer F., Arnold S., Braun D., Teraoka I., and Libchaber A., *Multiplexed DNA quanti. cation by spectroscopic shift of two microsphere cavities.* Biophysical Journal, 2003. **85**(3): p. 1974-1979.
5. Agrawal G. P., *Fiber-optic communication systems.* Wiley series in microwave and optical engineering. 1992: A wiley-interscience publication.
6. Tzeng H. M., Wall K. F., Long M. B., and Chang R. K., *Laser-Emission From Individual Droplets At Wavelengths Corresponding To Morphology-Dependent Resonances.* Optics Letters, 1984. **9**(11): p. 499-501.
7. Lin H. B. and Campillo A. J., *Cw Nonlinear Optics In Droplet Microcavities Displaying Enhanced Gain.* Physical Review Letters, 1994. **73**(18): p. 2440-2443.
8. Lin H. B. and Campillo A. J., *Microcavity enhanced Raman gain.* Optics Communications, 1997. **133**(1-6): p. 287-292.
9. Zhang J. Z. and Chang R. K., *Generation And Suppression Of Stimulated Brillouin-Scattering In Single Liquid Droplets.* Journal Of The Optical Society Of America B-Optical Physics, 1989. **6**(2): p. 151-153.
10. Gorodetsky M. L., Savchenkov A. A., and Ilchenko V. S., *Ultimate Q of optical microsphere resonators.* Optics Letters, 1996. **21**(7): p. 453-455.
11. Spillane S. M., Kippenberg T. J., and Vahala K. J., *Ultralow-threshold Raman laser using a spherical dielectric microcavity.* Nature, 2002. **415**(6872): p. 621-623.

12. Cai M., Painter O., Vahala K. J., and Sercel P. C., *Fiber-coupled microsphere laser.* Optics Letters, 2000. **25**(19): p. 1430-1432.

13. *Sol-gel optics: processing and applications.* Kluwer international series in engineering and computer science. Electronic materials, science and technology, ed. L.C. Klein. 1994, Boston: Kluwer Academic.

14. Chen D. G., Potter B. G., and Simmons J. H., *Geo2-Sio2 Thin-Films For Planar Wave-Guide Applications.* Journal Of Non-Crystalline Solids, 1994. **178**: p. 135-147.

15. Gouveianeto A. S., *Modulation Instability And Soliton-Raman Generation In P2o5 Doped Silica Fiber.* Journal Of Lightwave Technology, 1992. **10**(11): p. 1536-1539.

16. Yang L. and Vahala K. J., *Gain functionalization of silica microresonators.* Optics Letters, 2003. **28**(8): p. 592-594.

17. Yeatman E. M., Ahmad M. M., McCarthy O., Vannucci A., Gastaldo P., Barbier D., Mongardien D., and Moronvalle C., *Optical gain in Er-doped SiO2-TiO2 waveguides fabricated by the sol-gel technique.* Optics Communications, 1999. **164**(1-3): p. 19-25.

18. Little B. E., Laine J. P., and Haus H. A., *Analytic theory of coupling from tapered fibers and half-blocks into microsphere resonators.* Journal Of Lightwave Technology, 1999. **17**(4): p. 704-715.

19. Collot L., Lefevreseguin V., Brune M., Raimond J. M., and Haroche S., *Very High-Q Whispering-Gallery Mode Resonances Observed On Fused-Silica Microspheres.* Europhysics Letters, 1993. **23**(5): p. 327-334.

20. Dubreuil N., Knight J. C., Leventhal D. K., Sandoghdar V., Hare J., and Lefevre V., *Eroded Monomode Optical-Fiber For Whispering-Gallery Made Excitation In Fused-Silica Microspheres.* Optics Letters, 1995. **20**(8): p. 813-815.

21. Knight J. C., Dnbreuil N., Sandoghdar V., Hare J., Lefevreseguin V., Raimond J. M., and Haroche S., *Mapping Whispering-Gallery Modes In Microspheres With A Near-Field Probe.* Optics Letters, 1995. **20**(14): p. 1515-1517.

22. Ilchenko V. S., Yao X. S., and Maleki L., *Pigtailing the high-Q microsphere cavity: a simple fiber coupler for optical whispering-gallery modes.* Optics Letters, 1999. **24**(11): p. 723-725.

23. Gorodetsky M. L. and Ilchenko V. S., *Optical microsphere resonators: optimal coupling to high-Q whispering-gallery modes.* Journal Of The Optical Society Of America B-Optical Physics, 1999. **16**(1): p. 147-154.

24. Hench L. L. and West J. K., *The Sol-Gel Process.* Chemical Reviews, 1990. **90**(1): p. 33-72.

25. McCarthy G. J., Roy R., and McKay J. M., *Preliminary Study Of Low-Temperature Glass Fabrication From Noncrystalline Silicas.* Journal Of The American Ceramic Society, 1971. **54**(12): p. 637-&.

26. Roy R., *Gel Route To Homogeneous Glass Preparation.* Journal Of The American Ceramic Society, 1969. **52**(6): p. 344-&.

27. Roy R., *Aids In Hydrothermal Experimentation.2. Methods Of Making Mixtures For Both Dry And Wet Phase Equilibrium Studies.* Journal Of The American Ceramic Society, 1956. **39**(4): p. 145-146.

28. Roy D. M. and Roy R., *An Experimental Study Of The Formation And Properties Of Synthetic Serpentines And Related Layer Silicate Minerals.* American Mineralogist, 1954. **39**(11-1): p. 957-975.

29. Roy R., *Ceramics By The Solution-Sol-Gel Route.* Science, 1987. **238**(4834): p. 1664-1669.

30. Wright J. D. and Sommerdijk N. A. J. M., *Sol-gel Materials: Chemistry and applications.* Advanced Chemistry Texts. 2001: Gordon and Breach Science Publishers.

31. Martucci A., Fick J., Schell J., Battaglin G., and Guglielmi M., *Microstructural and nonlinear optical properties of silica-titania sol-gel film doped with PbS quantum dots.* Journal Of Applied Physics, 1999. **86**(1): p. 79-87.

32. Benatsou M. and Bouazaoui M., *Fluorescence properties of sol-gel derived Er3+:SiO2-GeO2 planar waveguides.* Optics Communications, 1997. **137**(1-3): p. 143-150.

33. Sorek Y., Reisfeld R., Finkelstein I., and Ruschin S., *Sol-Gel Glass Wave-Guides Prepared At Low-Temperature.* Applied Physics Letters, 1993. **63**(24): p. 3256-3258.

34. Smith B. C., *Fundamentals of Fourier transform infrared spectroscopy.* 1996, Boca Raton, FL: CRC Press.

35. Davazoglou D. and Vamvakas V. E., *Arrangement of Si and O atoms in thermally grown SiO2 films.* Journal Of The Electrochemical Society, 2003. **150**(5): p. F90-F96.

36. Campostrini R., Carturan G., Ferrari M., Montagna M., and Pilla O., *Luminescence Of Eu3+ Ions During Thermal Densification Of Sio2 Gel.* Journal Of Materials Research, 1992. **7**(3): p. 745-753.

37. Zhao J., Sullivan J., and Bennett T. D., *Wet etching study of silica glass after CWCO2 laser treatment.* Applied Surface Science, 2004. **225**(1-4): p. 250-255.

38. Kim B. G., Kang S. Y., and Kim J. J., *FTIR study of fluorinated silicon oxide film.* Journal Of Physics D-Applied Physics, 1997. **30**(12): p. 1720-1724.

39. von Klitzing W., Jahier E., Long R., Lissillour F., Lefevre-Seguin V., Hare J., Raimond J. M., and Haroche S., *Very low threshold lasing in Er3+ doped ZBLAN microsphere.* Electronics Letters, 1999. **35**(20): p. 1745-1746.

40. Orignac X., Barbier D., Du X. M., and Almeida R. M., *Fabrication and characterization of sol-gel planar waveguides doped with rare-earth ions.* Applied Physics Letters, 1996. **69**(7): p. 895-897.

41. Bruynooghe S., Chabli A., Bertin F., Pierre F., and Leflem G., *Preparation and characterization of Nd3+ and Er3+-doped silica sol-gel coatings by Rutherford backscattering spectroscopy and spectroscopic ellipsometry.* Journal Of Materials Research, 1997. **12**(10): p. 2779-2783.

42. Chen S. Y., Ting C. C., and Li C. H., *Fluorescence enhancement and structural development of sol-gel derived Er3+-doped SiO2 by yttrium codoping.* Journal Of Materials Chemistry, 2002. **12**(4): p. 1118-1123.

43. Arena A., Patane S., Saitta G., Rizzo G., Galvagno S., and Neri G., *Preparation, characterization, and micropatterning of laser-dye-doped sol-gel films.* Journal Of Materials Research, 2002. **17**(8): p. 2095-2098.

44. Dong W. T. and Zhu C. S., *Optical properties of UV dye PTP-doped silica film prepared by sol-gel process.* Materials Letters, 2000. **45**(6): p. 336-339.

45. Slooff L. H., de Dood M. J. A., van Blaaderen A., and Polman A., *Effects of heat treatment and concentration on the luminescence properties of erbium-doped silica sol-gel films.* Journal Of Non-Crystalline Solids, 2001. **296**(3): p. 158-164.

46. Knight J. C., Cheung G., Jacques F., and Birks T. A., *Phase-matched excitation of whispering-gallery-mode resonances by a fiber taper.* Optics Letters, 1997. **22**(15): p. 1129-1131.

47. Chang R. K. and Campillo A. J., *Optical Processes in Microcavities.* 1996: World Sientific, Singapore.

48. Gorodetsky M. L. and Ilchenko V. S., *High-Q Optical Whispering-Gallery Microresonators - Precession Approach For Spherical Mode Analysis And Emission Patterns With Prism Couplers.* Optics Communications, 1994. **113**(1-3): p. 133-143.

49. Siegman A. E., *Lasers.* 1986: University Science Books, Mill Valley, CA.

50. Chang S. S., Rex N. B., Chang R. K., Chong G., and Guido L. J., *Stimulated emission and lasing in whispering-gallery modes of GaN microdisk cavities.* Applied Physics Letters, 1999. **75**(2): p. 166-168.

51. Armani D. K., Kippenberg T. J., Spillane S. M., and Vahala K. J., *Ultra-high-Q toroid microcavity on a chip.* Nature, 2003. **421**(6926): p. 925-928.

52. McLachlan A. D. and Meyer F. P., *Temperature-Dependence Of The Extinction Coefficient Of Fused-Silica For Co2-Laser Wavelengths.* Applied Optics, 1987. **26**(9): p. 1728-1731.

53. Sheikbahae M. and Kwok H. S., *Controlled Co2-Laser Melting Of Silicon.* Journal Of Applied Physics, 1988. **63**(2): p. 518-524.

54. Becker P. C., Olsson N. A., and Simpson J. R., *Erbium-doped fiber amplifiers:fundamentals and technology.* 1999, San Diego: Academic Press.

55. Islam M. N., *Raman amplifiers for telecommunications.* Ieee Journal Of Selected Topics In Quantum Electronics, 2002. **8**(3): p. 548-559.

56. Troccoli M., Belyanin A., Capasso F., Cubukcu E., Sivco D. L., and Cho A. Y., *Raman injection laser.* Nature, 2005. **433**(7028): p. 845-848.

57. Yang L., Armani D. K., and Vahala K. J., *Fiber-coupled erbium microlasers on a chip.* Applied Physics Letters, 2003. **83**(5): p. 825-826.

58. Polman A., Min B., Kalkman J., Kippenberg T. J., and Vahala K. J., *Ultralow-threshold erbium-implanted toroidal microlaser on silicon.* Applied Physics Letters, 2004. **84**(7): p. 1037-1039.

59. Kippenberg T. J., Spillane S. M., Armani D. K., and Vahala K. J., *Ultralow-threshold microcavity Raman laser on a microelectronic chip.* Optics Letters, 2004. **29**(11): p. 1224-1226.

60. Hattori K., Kitagawa T., Oguma M., Ohmori Y., and Horiguchi M., *Erbium-Doped Silica-Based Wave-Guide Amplifier Integrated With A 980 1530nm Wdm Coupler.* Electronics Letters, 1994. **30**(11): p. 856-857.

61. Li Y. P. and Henry C. H., *Silica-based optical integrated circuits.* Iee Proceedings-Optoelectronics, 1996. **143**(5): p. 263-280.

62. Huang W. and Syms R. R. A., *Sol-gel silica-on-silicon buried-channel EDWAs.* Journal Of Lightwave Technology, 2003. **21**(5): p. 1339-1349.

63. Chen K. M., Sparks A. W., Luan H. C., Lim D. R., Wada K., and Kimerling L. C., *SiO2/TiO2 omnidirectional reflector and microcavity resonator via the sol-gel method.* Applied Physics Letters, 1999. **75**(24): p. 3805-3807.

64. Jang J. K. and Yoon H., *Novel fabrication of size-tunable silica nanotubes using a reverse-microemulsion-mediated sol-gel method.* Advanced Materials, 2004. **16**(9-10): p. 799-+.

65. Stolen R. H. and Ippen E. P., *Raman Gain In Glass Optical Waveguides.* Applied Physics Letters, 1973. **22**(6): p. 276-278.

66. Dianov E. M., *Advances in Raman fibers.* Journal Of Lightwave Technology, 2002. **20**(8): p. 1457-1462.

67. Yang L., Carmon T., Min B., Spillane S. M., and Vahala K. J., *Erbium-doped and Raman microlasers on a silicon chip fabricated by the sol-gel process.* Applied Physics Letters, 2005. **86**(9): p. 091114.

68. Syms R. R. A., Schneider V., Huang W., and Holmes A. S., *Low-Loss Achieved In Sol-Gel Based Silica-On-Silicon Integrated-Optics Using Borophosphosilicate Glass.* Electronics Letters, 1995. **31**(21): p. 1833-1834.

69. Bellessa J., Rabaste S., Plenet J. C., Dumas J., Mugnier J., and Marty O., *Eu3+-doped microcavities fabricated by sol-gel process.* Applied Physics Letters, 2001. **79**(14): p. 2142-2144.

70. Haus H. A., *Waves and fields in optoelectronics.* Prentice-Hall series in solid state physical electronics. 1984.

71. Min B. K., Kippenberg T. J., Yang L., Vahala K. J., Kalkman J., and Polman A., *Erbium-implanted high-Q silica toroidal microcavity laser on a silicon chip.* Physical Review A, 2004. **70**(3).

72. Spillane S. M., Kippenberg T. J., Painter O. J., and Vahala K. J., *Ideality in a fiber-taper-coupled microresonator system for application to cavity quantum electrodynamics.* Physical Review Letters, 2003. **91**(4).

73. Maiman T. H., *Stimulated Optical Radiation In Ruby.* Nature, 1960. **187**(4736): p. 493-494.

74. Hideur A., Chartier T., Ozkul C., and Sanchez F., *Dynamics and stabilization of a high power side-pumped Yb-doped double-clad fiber laser.* Optics Communications, 2000. **186**(4-6): p. 311-317.

75. Colin S., Contesse E., LeBoudec P., Stephan G., and Sanchez F., *Evidence of a saturable-absorption effect in heavily erbium-doped fibers.* Optics Letters, 1996. **21**(24): p. 1987-1989.

76. Sanchez F. and Stephan G., *General analysis of instabilities in erbium-doped fiber lasers.* Physical Review E, 1996. **53**(3): p. 2110-2122.

77. Wysocki P. F., Wagener J. L., Digonnet M. J. F., and Shaw H. J. *Evidence and modeling of paired ions and other loss mechanisms in erbium-doped silica fibers.* in *SPIE: Fiber Laser source adn Amplifiers IV*. 1992.

78. Sanchez F., Leboudec P., Francois P. L., and Stephan G., *Effects Of Ion-Pairs On The Dynamics Of Erbium-Doped Fiber Lasers.* Physical Review A, 1993. **48**(3): p. 2220-2229.

79. He M., Yuan X. C., Ngo N. Q., Bu J., and Kudryashov V., *Simple reflow technique for fabrication of a microlens array in solgel glass.* Optics Letters, 2003. **28**(9): p. 731-733.